Factors Affecting the Design Thickness of Bridge Slabs

by

John Conley Graddy, B.S.C.E.

Thesis

Presented to the Faculty of the Graduate School

of The University of Texas at Austin

in Partial Fulfillment

of the Requirements

for the Degree of

Master of Science in Engineering

The University of Texas at Austin

May 1995

Factors Affecting the Design Thickness of Bridge Slabs

APPROVED BY

SUPERVISING COMMITTEE:

_____

Richard E. Klingner

_____

Ned H. Burns

To my parents

ACKNOWLEDGMENT

I want to thank Dr. Ned H. Burns and Dr. Richard E. Klingner for allowing me the opportunity to participate in the research project discussed in this thesis. Their patience, guidance, and personable attention through the duration of this project made it a truly enjoyable experience. I am truly grateful to all of my other friends at the Ferguson Structural Engineering Laboratory for their daily help and understanding, and to Mr. Charles F. Terry and his staff for their friendship and for the use of their resources in times of need. I am also grateful for the financial support provided by the Texas Department of Transportation, and to Austin Prestress Company for their donation of precast prestressed concrete panels to this project.

My parent's love and support made it possible for me to attend The University of Texas at Austin. I will never be able to repay them for all that they have given to me and instilled in my soul.

John Graddy

April 1995

ABSTRACT

Factors Affecting the Design Thickness of Bridge Slabs

by

John Conley Graddy, M.S.E.

The University of Texas at Austin, 1995

SUPERVISOR: Richard E. Klingner

An analytical and experimental investigation into the punching shear fatigue behavior of bridge decks, including the effects of arching action, is discussed. The experimental investigation included static and pulsating fatigue tests on cast-in-place and precast prestressed panel specimens. Failure modes, loads, and test specimen behaviors observed during the experimental tests are discussed and compared with analytical predictions. Finite element models of a full-scale bridge and for test specimens were developed. Those models are discussed, and the analytical results obtained from them are compared with the experimental test results. A method of including the effects of membrane compression in punching shear capacity calculations that gives reasonable agreement with experimental test results is proposed. S-N curves suitable for pulsating and rolling fatigue design and assessment purposes were developed and are included. Recommendations for further research into the punching shear

fatigue behavior and flexural capacity of bridge decks are also included in this thesis

TABLE OF CONTENTS

LIST OF TABLES

LIST OF FIGURES

CHAPTER ONE
INTRODUCTION

1.1 General

Arching action is known to increase the flexural capacity of cracked slabs and bridge decks (Batchelor 1978, Fang 1986, Elling 1986, Tsui 1986, Kim 1988, Fang 1990a, Fang 1990b, Klingner 1990). The recognition and utilization of arching action is allowing engineers to design more efficient and less expensive bridge decks than was possible in the recent past. Significant savings in material and labor costs associated with deck construction are being realized through the adoption of the isotropically reinforced, "Ontario-type" bridge decks into design provisions used in Texas and elsewhere in the United States.

The increase in flexural capacity due to arching action can be so significant that punching shear capacity will control the design of a bridge deck. However, research pertaining to punching shear in bridge decks, especially in fatigue, has been limited. As a result, the Texas Department of Transportation (TxDOT) sponsored the investigation presented in this thesis into the effects of fatigue deterioration on the punching shear resistance of bridge decks.

1.2 Purpose and Scope

The general purpose of TxDOT Project 3-15D-92-1305 was to develop guidelines for specifying the required thickness of bridge decks as a function of traffic characteristics such as loading level, wheel spacing and expected fatigue history. The investigation included the development of analytical models and experimental tests that adequately reflected the behavior of bridge decks. Research by others was also relied upon where necessary. Slab specimens were

tested in static and fatigue loading in order to develop "S-N curves" for punching shear fatigue. These curves relate the maximum punching shear stress range due to an applied load cycle, to the number of load cycles required to cause a punching shear failure. Both cast-in-place (CIP) and precast prestressed panel (PCP) bridge deck configurations were investigated.

1.3 Objectives

The primary objective of Project 1305 is to recommend guidelines for specifying the required thickness of bridge decks as a function of traffic characteristics. To accomplish this objective, the following tasks were planned:

1) Review past research pertaining to the wheel load, axle width, and axle spacing characteristics of standard and nonstandard loads.
2) Use structural analysis computer programs and engineering models to estimate the stress range experienced by a full-scale cracked bridge deck subjected to a conventional truck loading, and to predict the maximum principal tensile stress in the cracked deck.
3) Design and construct a test setup that would be suitable for the static and dynamic testing of full-scale bridge decks, including both rolling and pulsating (constant location) loads.
4) Develop S-N curves for both CIP reinforced concrete decks and PCP decks, and to use these curves to determine the relationship between rolling and fixed load applications, and of arching action.

1.4 Typical Texas Bridge Deck Construction

As stated in the Bridge Design Guide used by bridge designers in Texas, design specifications for bridge decks have evolved "from none in the beginning...to the completely empirical design method specified in the Ontario Highway Bridge Design Code" (Bridge Design Guide 1990). Various methods of constructing bridge decks on stringers have evolved as well. Driven by economic considerations, bridge construction has evolved through fully shored construction of monolithic slab and girder bridges to the current practice of casting the deck on prestressed concrete or structural steel stringers. Three methods are currently used to construct the latter type of deck. Temporary formwork and permanent metal deck forms are used, but the "preferred method of constructing decks on prestressed concrete beams" is with the use of precast prestressed concrete panels (Bridge Design Guide 1990).

1.5 Current AASHTO Design Provisions

Current design provisions for bridge decks adopted and published by the American Association of State Highway and Transportation Officials (AASHTO) and specified in the Standard Specifications for Highway Bridges (AASHTO Code), are patterned after and in general conformity with provisions of the American Concrete Institute Building Code Requirements for Reinforced Concrete (ACI Code). Texas design practice departs from the AASHTO Code where justified by local research or proven experience (Bridge Design Guide 1990).

Bridge decks have been designed for flexure as one-way slabs. Reinforcement is proportioned to satisfy moments calculated using an empirical equation that neglects the beneficial affects of arching action. As discussed above, research has shown that this results in conservative flexural designs due to the presence of arching action.

1.6 Isotropically Reinforced Bridge Decks

Isotropically reinforced bridge decks have begun to be used in Texas. This type of deck, and the design method associated with it, is based on the principle that a bridge deck's flexural capacity is increased by the presence of arching and proportions reinforcement based on empirical methods. Isotropically reinforced bridge decks are designed in Texas based on the following provisions (Bridge Design Guide 1990):

- Minimum slab thickness is 7.5 inches (191 mm).
- Maximum design span length is 15 times the slab thickness.
- Minimum isotropic reinforcement in each layer is 0.3 percent of the slab area using the average depth to the bottom layer of reinforcement.
- There must be a 3.28 foot (1.0 m) overhang. Concrete railing and overhang having an equivalent area is acceptable.

Additional provisions concerning skewed bridges, cantilevers and diaframs not included here must also be addressed. When precast prestressed panels are used, they replace the bottom mat of reinforcement.

1.7 Overview of Thesis

This thesis summarizes the background information required to understand the theories tested and the expected test specimen behavior. This, along with related research conducted by others, is discussed in Chapter 2. Chapters 3 and 4 discuss the analytical models used in accomplishing the research objectives. The experimental testing program is presented in Chapter 5. Typical test results for CIP and PCP test specimens are presented in Chapters 6 and 7. Chapter 8 discusses observed failure modes and loads and compares experimental test results with analytical predictions. S-N data and other results obtained from

experimental tests are discussed in Chapter 9. A discussion on the application of test results to the design of bridge decks is the subject of Chapter 10. Finally, Chapter 11 summarizes the research program, presents the conclusions reached by investigators, and makes recommendations for applying the results to the design of bridge decks and for further research.

CHAPTER TWO
BACKGROUND

2.1 Introduction

This chapter reviews the background information presented in previous reports for this project (Whitt 1993, Kim 1994). Included are discussions of arching action and punching shear in concrete slabs and of general fatigue behavior. Research conducted by others that influenced this project involving both pulsating and rolling loads on bridge decks are also discussed.

2.2 Arching Action

When an uncracked bridge deck is loaded by traffic, it resists the load primarily through one-way (transverse) flexure. Before flexural cracking occurs, in-plane forces remain insignificant. However, after the deck is significantly cracked, it resists traffic loads through arching action, similar to a flat dome. Arching action is defined by a zone of compression radiating out from the point of load and a surrounding zone of circumferential tension (hoop stresses) in equilibrium with the radiating compressive forces. This is illustrated schematically in Figure 2.1. The compressive membrane forces increase the flexural capacity of a bridge deck. These membrane forces exist even if supports are unrestrained, although the distribution of membrane forces is influenced by the degree of edge restraint.

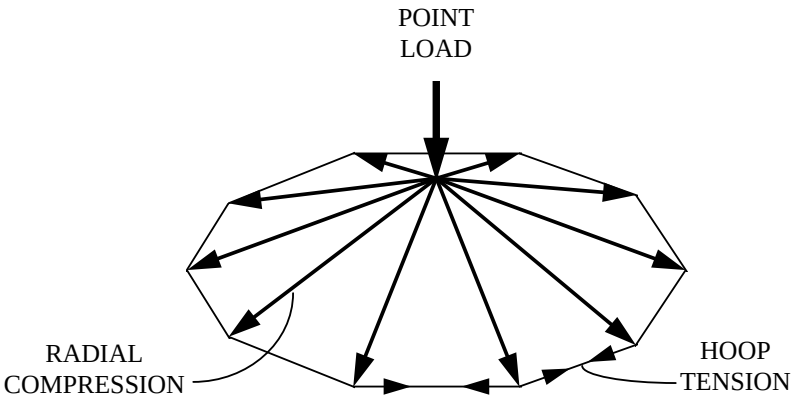

Figure 2.1: Schematic representation of arching action in a concrete slab due to a point load.

The increase in flexural capacity due to arching action is the basis for the isotropically reinforced, "Ontario-type," bridge deck. This empirical design method requires an isotropic reinforcement layout that uses much less reinforcing steel than would be required in a traditional deck design using procedures of the AASHTO Code. Much research has been conducted testing this procedure, and many bridges have been constructed using this design method. Their performance is being monitored and has been satisfactory.

2.2.1 Typical AASHTO Truck Loading

A standard AASHTO truck has a variable axle spacing with a minimum of 14 feet (4.27 m) between axle loads. This relatively large axle spacing allows arching action to develop, which significantly increases the flexural capacity of a typical bridge deck.

2.2.2 Multiple Closely Spaced Axle Loading

How arching action is affected when loads are applied simultaneously at multiple locations is not completely understood. As mentioned above, a point load creates the effect of a flat dome; however, when a line load or group of closely spaced loads is applied, the zone of tension extends on the length of the line, as illustrated in Figure 2.2. This "spreading" of the dome reduces the effectiveness of arching action. This is illustrated by noting that without a tension tie to maintain equilibrium in the transverse direction, the interior loads shown in Figure 2.2 are resisted by one-way flexure only, without arching action. This is a practical concern in bridges when dealing with long, multiple-axle trailers carrying unusually large loads.

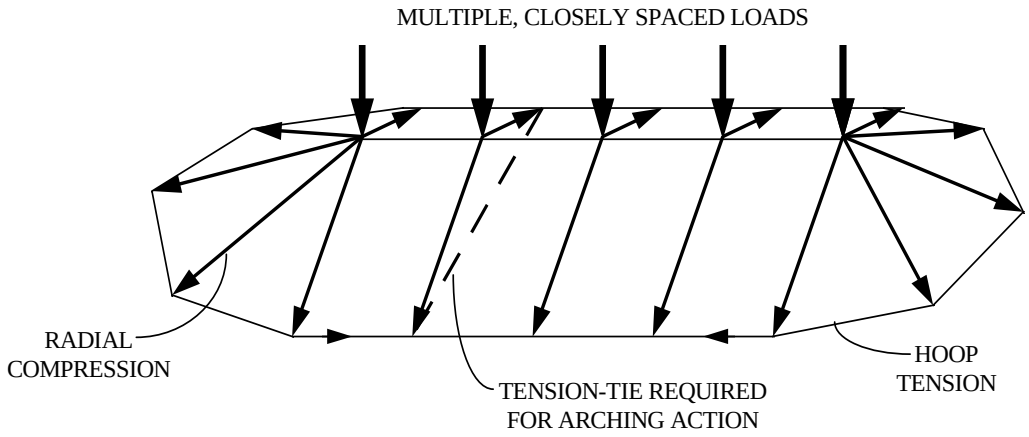

Figure 2.2: Schematic illustration showing the reduced effectiveness of arching action in a concrete slab due to multiple, closely spaced loads.

2.3 Fatigue Behavior

Under cyclic stresses, a material's load-carrying capacity can deteriorate -- the higher the number of cycles, the greater the deterioration. If a material is subjected to a large number of loading cycles, its nominal capacity can decrease, even if the load is fairly small relative to the nominal capacity. This phenomenon, referred to as fatigue deterioration, is of particular concern in the design of highway bridges and bridge decks. These structures are subjected to millions of loading cycles over their design lives, sometimes at very large loads relative to those assumed in design.

The relationship between applied stress range and the number of stress cycles must be known in order to predict the reduced capacity of a fatigued structure. This relationship is typically illustrated on "S-N curves." On an S-N curve for punching shear, the zero cycle point is merely the static capacity of the structure. This point can be predicted with relative ease and accuracy by analysis, and verified with experimental tests. However, the rest of the curve is less well known. Establishing this curve using experimental tests is an important aspect of this project. Fatigue cycles can be estimated as a function of traffic and age for real bridges. Using these estimates along with analytical models, the reduced capacity of a bridge can be estimated using the S-N curves established from experimental tests. An example of an S-N curve is shown in Figure 2.3.

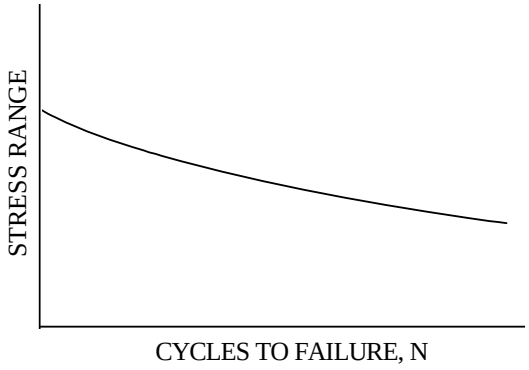

Figure 2.3: Example of an S-N curve.

Two types of fatigue behavior were to be studied in this project: pulsating fatigue, which concerns a constant-location load of varying magnitude, and

rolling fatigue, which concerns a constant-magnitude, varying location load. However, in spite of diligent efforts, rolling fatigue tests were not performed successfully. The difficulties involved in moving a large wheel load in a stable manner for many cycles were more than anticipated. Results from rolling fatigue tests conducted by other researchers were used to correlate the fatigue deterioration observed in pulsating fatigue tests to that caused by rolling fatigue.

2.4 Research by Others

Arching action in concrete bridge decks and fatigue behavior of concrete slabs have been important subjects in recent research. As discussed in previous reports, other studies have significantly influenced this project: a previous study conducted at The University of Texas at Austin of Ontario-type bridge decks (Fang 1986, Elling 1986, Tsui 1986, Kim 1988); a project at Case Western Reserve University that examined rolling fatigue behavior of concrete slabs (Perdikaris 1988, 1989); and a study conducted in Japan of rolling fatigue behavior of concrete slabs (Matsui 1986). These studies were reviewed in previous reports (Whitt 1993, Kim 1994), and relevant details are summarized in the following sections.

2.4.1 Pulsating Fatigue

The study conducted at The University of Texas at Austin investigated the performance of an Ontario-type bridge deck on steel girders. The full-scale bridge was constructed using a combination of cast-in-place deck and precast prestressed panels covered with a cast-in-place topping. Performance of the structure was satisfactory under both static and fatigue loading. These tests showed that arching action could be considered in flexural design; and due in part

to this arching action, punching shear will usually govern the capacity of concrete bridge decks.

2.4.2 Rolling Fatigue

Perdikaris and others studied the affects of pulsating and rolling loads on concrete bridge decks designed with both orthotropic reinforcement and isotropic reinforcement (Perdikaris 1988, 1989). Experiments were performed on small-scale model decks 1.25 inches (31.8 mm) thick and supported on steel girders. Experiments into the affects of rolling fatigue on concrete bridge decks were also conducted by Matsui *et al.* in Japan (Matsui 1986). Small-scale models and full-scale specimens were tested. Only orthotropic reinforcing steel layouts were used in those tests.

Both of those studies showed that rolling loads produced more fatigue deterioration than fixed-location, pulsating loads. Extensive grid-like, "alligator-skin" cracking patterns were observed in both studies. As stated in the report by Matsui *et al.*, that cracking pattern closely resembled those observed in actual bridge decks, confirming that their rolling-fatigue test setup closely simulated the behavior of actual slabs.

CHAPTER THREE
ANALYTICAL MODELING FOR DESIGN

3.1 Purpose and Scope

As detailed in previous reports (Whitt 1993, Kim 1994), analytical procedures were used to develop laboratory test specimens that would reflect the actual behavior of bridge decks. Analytical procedures were also required to extend the applicability of experimental test results to full-scale bridge decks. Finite element models and design equations were used to accomplish these two objectives. Finite element analytical modeling is discussed in Chapter 4 of this thesis.

Other analytical models were required to develop a correlation between experimental test data, finite element models and equations used in bridge deck design. This Chapter discusses the analytical models used to calculate the design flexural and punching shear capacities used in the development of laboratory test specimens. The flexural and punching shear capacities calculated for both cast-in-place (CIP) and precast prestressed panel (PCP) test specimens are included. Predicted capacities are compared with experimental test results in Chapter 8.

3.2 Punching Shear Capacities

Two equations were used to estimate punching shear capacities for test specimens. The first was the punching shear capacity equation given in both the AASHTO and ACI codes. The second was the general model punching shear capacity equation discussed in previous reports (Tsui 1986, Whitt 1993, Kim 1994). The equations were used as presented in the following sections for both CIP and PCP test specimens.

3.2.1 AASHTO and ACI Equation for Punching Shear Capacity

The AASHTO equation for the punching shear capacity of slabs (Eq. 8-58 of the AASHTO Code) is identical to the ACI punching shear capacity equation (Eq. 11-36 of the ACI Code) for the punching shear capacity associated with a rectangular footprint in nonprestressed slabs and for slabs prestressed in one direction only, and can be expressed as:

$$V_C = 2\left(b_1 + b_2 + 2\bar{d}\right)\bar{d}\, f_t \tag{3.1}$$

$$f_t = \left(2 + \frac{4}{\beta_c}\right)\sqrt{f'_c} \;\le\; 4\sqrt{f'_c} \tag{3.2}$$

where:

V_C = punching shear capacity, lbs.

b_1 = short side of concentrated load or reaction area, in.

b_2 = long sides of concentrated load or reaction area, in.

$\bar{d}$ = average effective depth of section, in.

f_t = ultimate tensile capacity of concrete, psi

$\beta_c = \dfrac{b_2}{b_1}$

f'_c = specified compressive strength of concrete, psi

3.2.2 General Model Equation for Punching Shear Capacity

The general punching shear model was discussed in previous reports (Tsui 1986, Whitt 1993, Kim 1994) and is illustrated in Figure 3.1. The general punching shear equation is derived from equilibrium of forces acting on the assumed failure planes shown in the figure. This general equation can be expressed as:

$$V_C = 2\left(b_1 + b_2 + \frac{2\bar{d}}{\tan\theta}\right)\frac{\bar{d}}{\tan\theta} f_t \qquad (3.3)$$

which reduces to the AASHTO and ACI equation when the angle θ is set to 45^o. The angle θ is the acute angle between the horizontal and the assumed failure plane and is shown in Figure 3.1. As was reported in previous reports for this project (Whitt 1993, Kim 1994), an angle θ of 38^o, and the ultimate tensile capacity of concrete given by Eq. (3.2), were used in punching shear calculations using the general model equation.

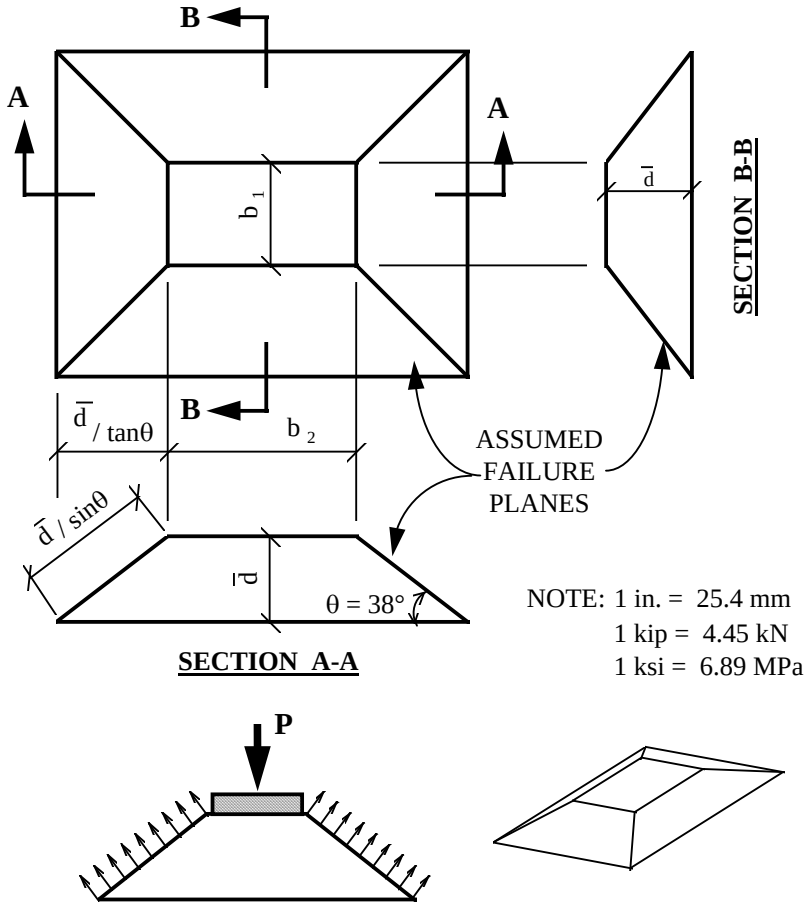

Figure 3.1: General punching shear model showing assumed failure planes and forces acting in equilibrium.

3.2.3 Predicted Punching Shear Capacity for Cast-in-Place Test Specimens

Table 3.1 summarizes calculated punching shear capacities, V_C, using both of the above equations. Values for constants used in these calculations are also included in the table. These constants are based on actual test specimen parameters for static tests, which are discussed in Chapter 5. Figure 3.7 at the end of this chapter presents calculated punching shear capacities in graphic form

along with loads which were calculated to cause flexural failure (discussed in Section 3.3 of this chapter).

Table 3.1: Summary of calculated punching shear capacities, V_C, and constants used in punching shear equations for cast-in-place test specimens.

	AASHTO and ACI Equation		General Model Equation	
V_C	127 kips		171 kips	
Constants Used in Punching Shear Equations				
f'_c (psi)	b_1 (in.)	b_2 (in.)	$\bar{d}$ (in.)	f_t (psi)
5,950	16.0	24.0	4.25	309

Note: 1 in. = 25.4 mm, 1 kip = 4.45 kN, 1 psi = 6.89 kPa

3.2.4 Predicted Punching Shear Capacity for Precast Prestressed Panel Test Specimens

Table 3.2 summarizes calculated punching shear capacities, V_C, using both of the above equations. Values for constants used in these calculations are also included in the table. These constants are based on actual test specimen parameters, which are discussed in Chapter 5. The value in Table 3.2 for the compressive strength of concrete used in the calculations is that of the cast-in-place concrete topping as determined from cylinder tests performed at the time of static testing. The value in the table is the average of strengths determined from both static tests. The depth to the bottom of the prestressing strands was used as the effective depth, and no increase was considered in the ultimate tensile capacity of concrete due to the effects of prestressing. The calculated punching shear capacities are presented in graphic form at the end of this chapter in Figure

3.8 for PCP specimens, along with calculated flexural capacities (discussed in Section 3.3 of this chapter).

The PCP test specimens did not behave as expected. Chapter 8 discusses this unexpected behavior in detail. The calculated capacities presented in Table 3.2 do not reflect the adjustments discussed in Chapter 8, which were made in order to correlate experimental data with analytical models. It should also be noted here that (as discussed in Chapter 5) the loaded area for PCP test specimens was reduced from that used for CIP test specimens.

Table 3.2: Summary of calculated punching shear capacities, V_C, and constants used in punching shear equations for precast prestressed panel test specimens.

	AASHTO and ACI Equation		General Model Equation	
V_C	115 kips		159 kips	
Constants Used in Punching Shear Equations				
f'_c (psi)	b_1 (in.)	b_2 (in.)	$\bar{d}$ (in.)	f_t (psi)
4,750	10.0	17.5	5.44	276 psi

Note: 1 in. = 25.4 mm, 1 kip = 4.45 kN, 1 psi = 6.89 kPa

3.3 Flexural Capacities

This research project required that maximum loads applied to test specimens would not result in flexural failure. Expected maximum loads were dictated by the calculated punching shear capacities discussed in the previous section. Moment-curvature analyses were used to calculate flexural capacities of CIP and PCP test specimens. Actual material properties and specimen parameters

were used in the calculations, along with an assumed maximum useful concrete compressive strain of 0.003. Nominal flexural capacities in both the longitudinal and transverse directions were calculated. Figure 3.2 shows a test specimen plan with coordinate axes and the notation used in the following discussion of calculated flexural capacities.

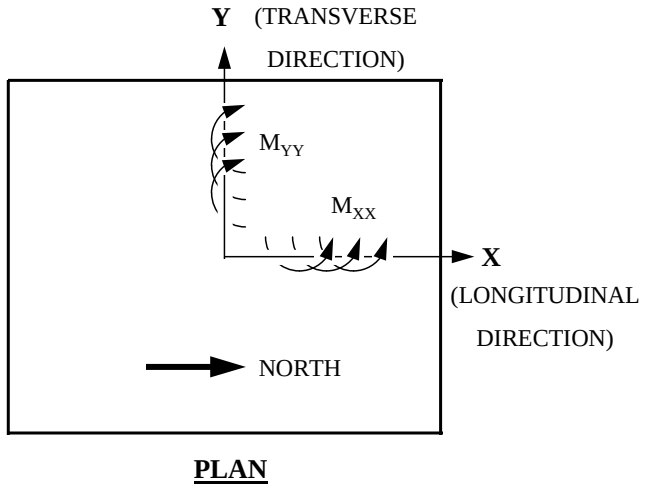

Figure 3.2: Test specimen coordinate axes and notation used for flexural capacities. Moments shown are those acting on the northwest quadrant.

3.3.1 Cast-in-Place Test Specimens

As discussed in Chapter 5, CIP test specimens were provided with twice as much bottom reinforcing steel in the transverse direction as in the longitudinal direction. Accordingly, M_{XX} moment capacity calculated by moment-curvature analysis was about twice the M_{YY} capacity. Calculated nominal capacities for M_{XX} and M_{YY} moments were 36.2 kip-ft/ft (161 kN-m/m) and 18.1 kip-ft/ft (80.5 kN-m/m) respectively. Calculated strains and forces acting through the depth of the section at nominal flexural capacity are shown in Figure 3.3 for CIP test

specimens. In the analysis, a reinforcing steel yield stress of 67.5 ksi (465 MPa) was used; 6,000 psi (41.3 MPa) was used for the compressive strength of concrete.

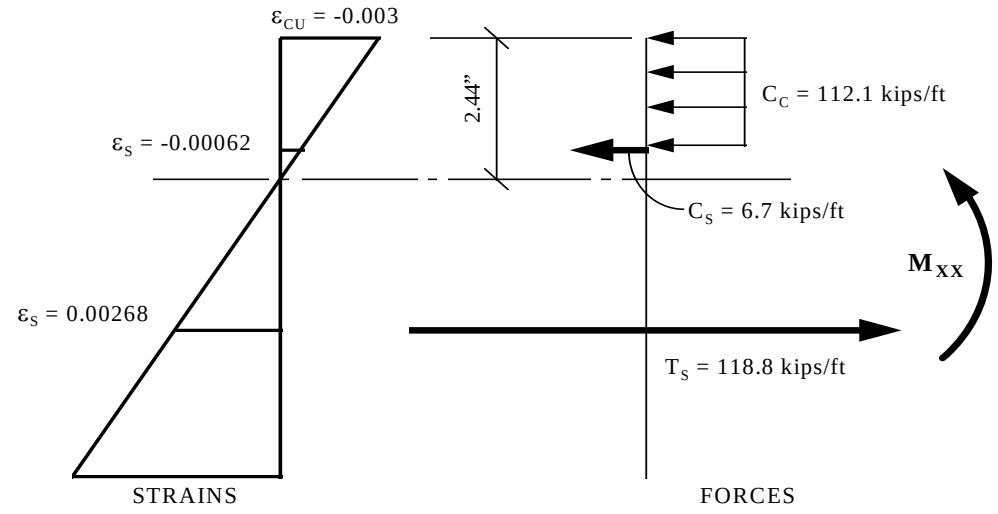

M_{XX} (YY DIRECTION)

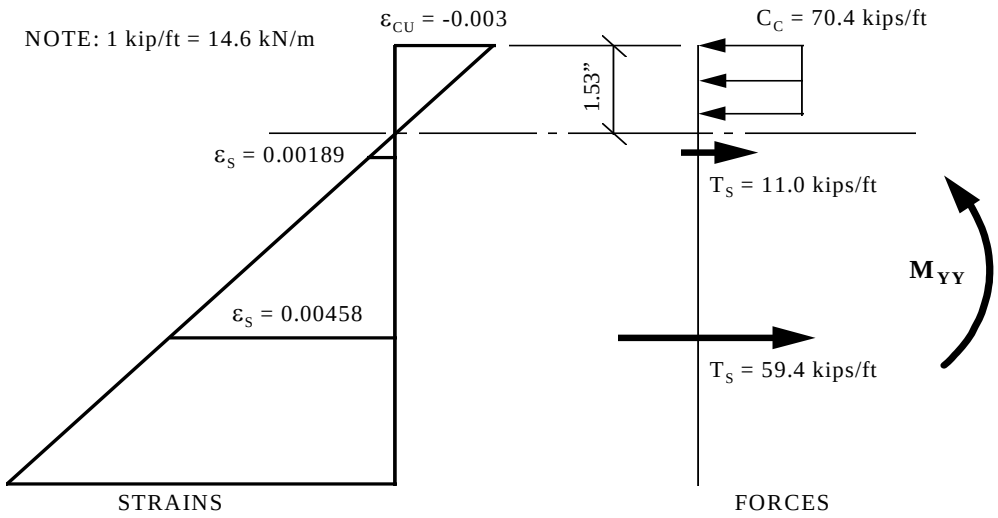

M_{YY} (XX DIRECTION)

Figure 3.3: Flexural strains and forces at nominal moment capacity calculated by moment-curvature analysis for cast-in-place test specimens.

3.3.2 Precast Prestressed Panel Test Specimens

Precast prestressed panels, constructed in accordance with Texas Department of Transportation (TxDOT) standard details, were donated to this research project by Austin Prestressed Company. The panels were cast in January of 1991 and stored until May of 1994, when they were delivered to the Phil M. Ferguson Structural Engineering Laboratory. To determine the prestress losses that had occurred during storage, calculations were made in accordance with the recommendations of the Precast Concrete Institute (PCI). These calculations are included in Appendix A. Losses of about 11% were calculated and used in the moment-curvature calculation of flexural capacity.

A value of 5,000 psi (34.5 MPa) was used for the compressive strength of concrete, and 67.5 ksi (465 MPa) was used for the yield strength of reinforcing steel bars cast in the topping. A value of 92.0 ksi (634 MPa) was used for the yield strength of welded wire fabric cast in the precast panels. This value was determined from tests on wires cut from one of the test specimens as discussed in Chapter 8. Force in prestressing strands was calculated using the stress strain relationship recommended by the PCI for strains greater than 0.008 in 270-ksi (1,860-MPa) strand:

$$f_{ps} = 268 - \frac{0.075}{E_{ps} - 0.0065} \leq 0.98 f_{pu} \qquad (3.6)$$

(Figure 11.2.5 of the PCI Design Handbook)

where

f_{ps} = stress in prestressing strand, ksi

E_{ps} = 28,000 ksi (193,000 MPa)

f_{pu} = 270 ksi (1,860 MPa)

Calculated nominal capacities for M_{XX} and M_{YY} moments were 20.7 kip-ft/ft (92.1 kN-m/m) and 12.2 kip-ft/ft (54.3 kN-m/m) respectively. Calculated strains and forces acting through the depth of the section at nominal flexural capacity are shown in Figure 3.4 for PCP test specimens.

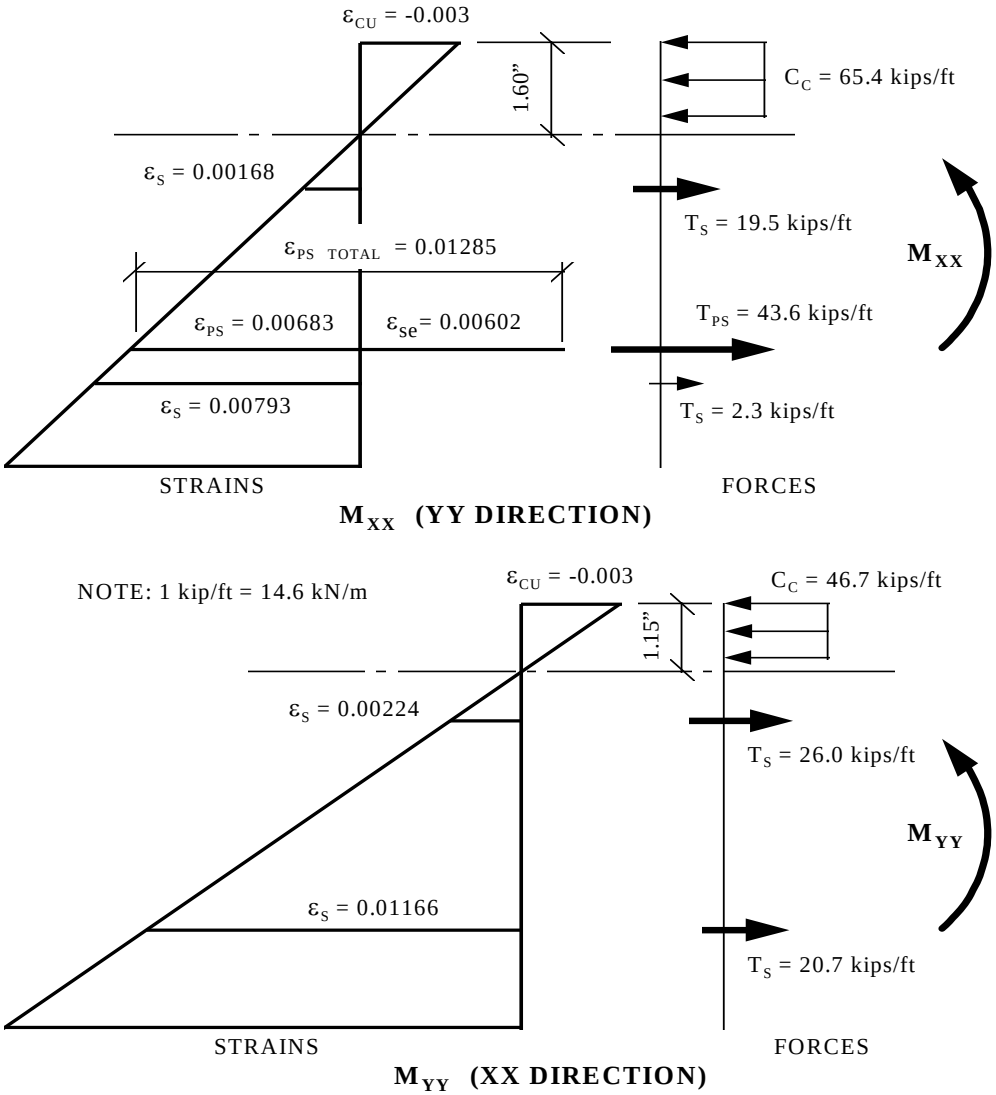

Figure 3.4: Flexural strains and forces at nominal moment capacity calculated by moment-curvature analysis for precast prestressed panel test specimens.

3.3.3 Yield Line Analyses

Flexural capacities calculated by moment-curvature analyses were used to calculate overall flexural capacities by yield line analysis. A complete discussion of yield line analysis is included in (MacGregor 1992), and is not be repeated here. Simple supports were assumed. Calculated nominal flexural capacities were 232 kips (1,030 kN) and 139 kips (619 kN) for CIP and PCP test specimens respectively. This information, along with calculated punching shear capacities, is presented in graphic form in Figure 3.7 for CIP and in Figure 3.8 for PCP test specimens at the end of this chapter. These capacities do not include the beneficial affects of arching action, which are discussed in the following section.

3.3.4 Affects of Arching Action on Flexural Capacity

As discussed in previous reports for this project (Whitt 1993, Kim 1994), the presence of membrane compression in the plane of a bridge deck due to arching action can significantly increase the deck's flexural capacity. Previous research (Fang 1986, Elling 1986, Tsui 1986, Kim 1988) also indicated that arching action was possible only after significant cracking had occurred in a bridge deck, and that membrane compression increased proportional to the applied wheel load. One reference (Tsui 1986) reported that in a full-scale test bridge, membrane compression reached 14 kips (62 kN) (in a 6-foot width) for each 20 kips (89 kN) of applied wheel load. This equates to an average membrane compressive force of about 2.33 kips/ft (34.0 kN/m) for 20 kips (89 kN) of applied wheel load. This magnitude of membrane compression would significantly increase the flexural capacity of a typical bridge deck.

Results from the finite element model for CIP test specimens, discussed in Chapter 4, indicated that arching action exists even in simply supported slabs. Compressive membrane forces observed in the test specimen analytical model of

this project were only slightly less than those calculated using the full-bridge analytical model, as well as those reported for tests on the full-scale bridge (Tsui 1986). Maximum compressive membrane forces in the finite element test specimen model were about 3.0 kips/ft (44 kN/m) and 2.1 kips/ft (31 kN/m) in the transverse and longitudinal directions respectively for each 20 kips (89 kN) of applied wheel load. The maximum value of transverse membrane compression observed in the finite element model of the full-bridge was about 3.7 kips/ft (54 kN/m) at 20 kips of applied wheel load. Membrane forces observed in the finite element models are discussed in detail in Chapter 4 of this thesis.

The wheel load calculated to cause flexural failure in CIP test specimens was found to be 232 kips (1,030 kN) without including the beneficial affects of arching action (Section 3.3.3 of this thesis). This would cause maximum membrane compressive forces of about 35 kips/ft (511 kN/m) in the transverse direction and about 24 kips/ft (350 kN/m) in the longitudinal direction, based on results from the finite element models and previous research (Fang 1986, Elling 1986, Tsui 1986, Kim 1988). These forces were included in the calculation of flexural capacity through the use of moment-axial force interaction diagrams. Figure 3.5 shows the interaction diagrams for CIP test specimens. A concrete compressive strength of 6,000 psi (41.3 MPa) and a yield strength for reinforcing steel of 67.5 ksi (465 MPa) were used to create the diagrams. The diagrams are for positive bending (tension bottom) only.

The unusual shape of the M_{XX} interaction curve shown in Figure 3.5 is the result of the highly asymmetric pattern of reinforcement used in the CIP test specimens. As discussed in Chapter 5, a very large amount of bottom transverse reinforcement was used in these specimens. This reinforcement was required to raise the predicted flexural capacity above the predicted punching shear capacity without consideration of the beneficial affects of arching action.

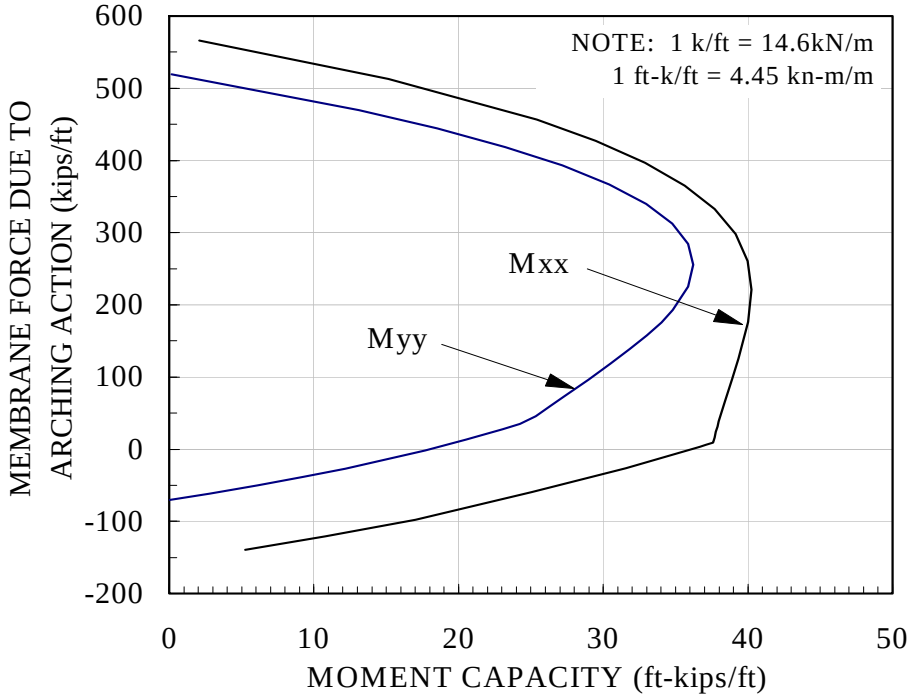

Figure 3.5: Interaction diagrams for cast-in-place test specimens.

Figure 3.5 indicates that for CIP test specimens, transverse compression could increase the M_{XX} moment capacity by about 10%, whereas longitudinal membrane compression could increase the M_{YY} moment capacity by a factor of about 2. However, the compressive membrane forces predicted by the finite element model were surrounded by membrane tensile forces that limited potential increases in flexural capacity. Membrane forces were estimated using results from the finite element model as discussed in Chapter 4. Figure 3.6 shows that portion of the interaction diagram (of Figure 3.5) covering the range of membrane forces predicted by the finite element model for CIP test specimens. Flexural capacities, including the affects of membrane compression and tension, were estimated using the partial interaction diagram of Figure 3.6.

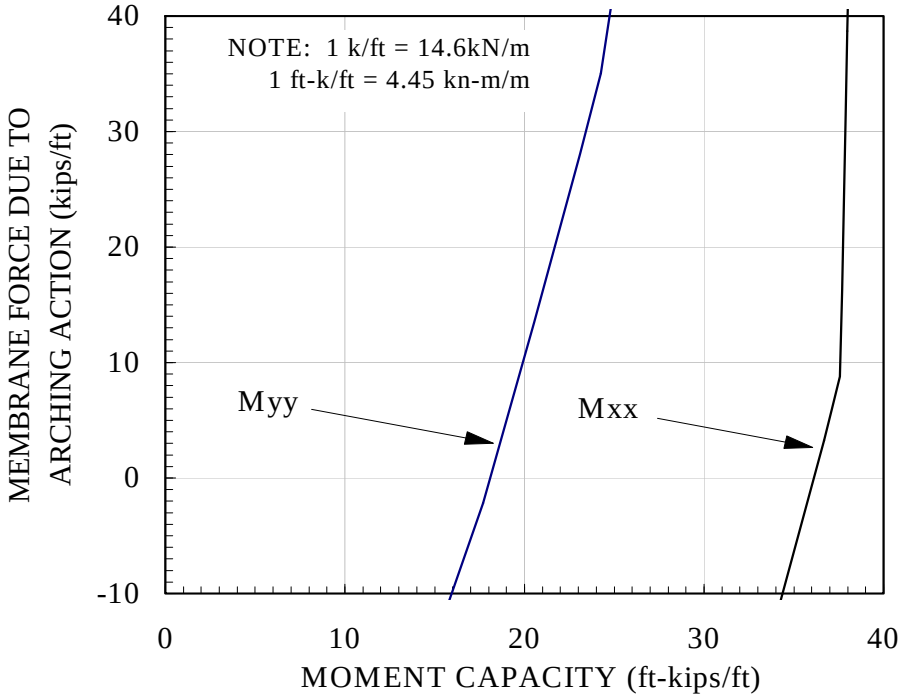

Figure 3.6: Partial interaction diagrams for cast-in-place test specimens.

The load calculated to cause flexural failure in PCP test specimens was found to be 139 kips (619 kN) without including the beneficial affects of arching action (Section 3.3.3 of this thesis). This would cause maximum membrane compressive forces of about 24 kips/ft (350 kN/m) in the transverse direction and about 14 kips/ft (204 kN/m) in the longitudinal direction based on results from the finite element models and previous research (Fang 1986, Elling 1986, Tsui 1986, Kim 1988). This assumes that membrane forces observed in the finite element model for CIP test specimens were applicable to PCP test specimens. These forces were included in the calculation of flexural capacity through the use of moment-axial force interaction diagrams as described for CIP specimens. Figure 3.7 shows the interaction diagrams for PCP test specimens. A concrete

compressive strength of 5,000 psi (34.5 MPa) was used to create the diagrams. In the diagrams, yield strengths of 67.5 ksi (465 MPa) and 92.0 ksi (634 MPa) were used for mild reinforcing steel used in the cast-in-place topping and for welded wire mesh used in the panels respectively. The stress-strain relation for prestressing strand given in Eq. (3.6) was also used to create the diagrams. The diagrams are for positive bending (tension bottom) only.

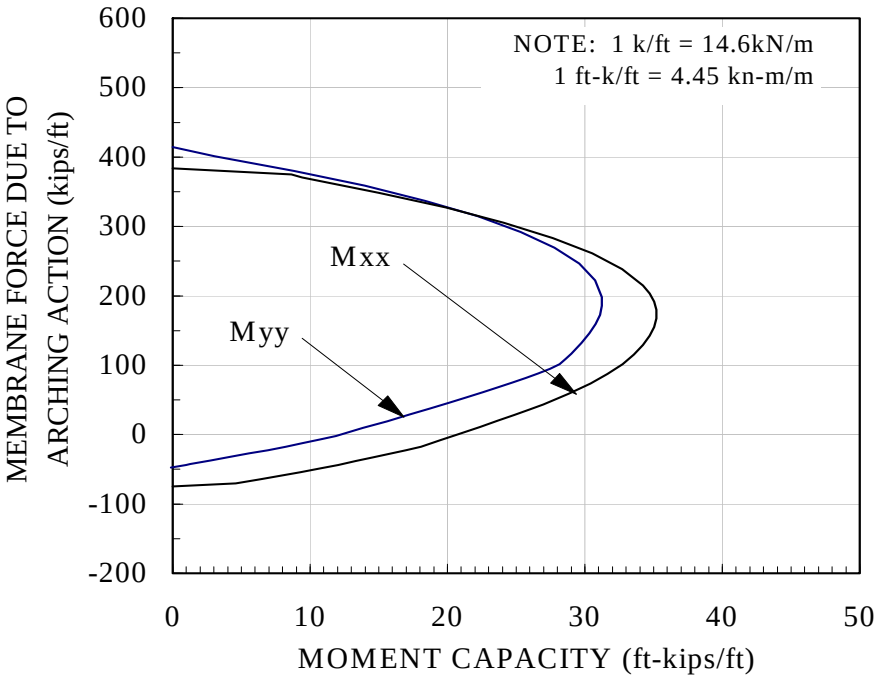

Figure 3.7: Interaction diagrams for precast prestressed panel test specimens.

Figure 3.7 indicates that for PCP test specimens, transverse membrane compression could increase the M_{XX} moment capacity by a factor of about 1.75, and longitudinal membrane compression could increase the M_{YY} moment capacity by a factor of more than 2.5. However, regions with compressive membrane forces, predicted by the finite element model, were surrounded by regions with

tensile membrane forces; this limited potential increases in the overall flexural capacity of the slabs. Figure 3.8 shows that portion of the interaction diagram (of Figure 3.7) covering the range of membrane forces predicted by the finite element model. Flexural capacities for PCP test specimens, including the affects of membrane compression and tension, were estimated using the partial interaction diagram of Figure 3.8.

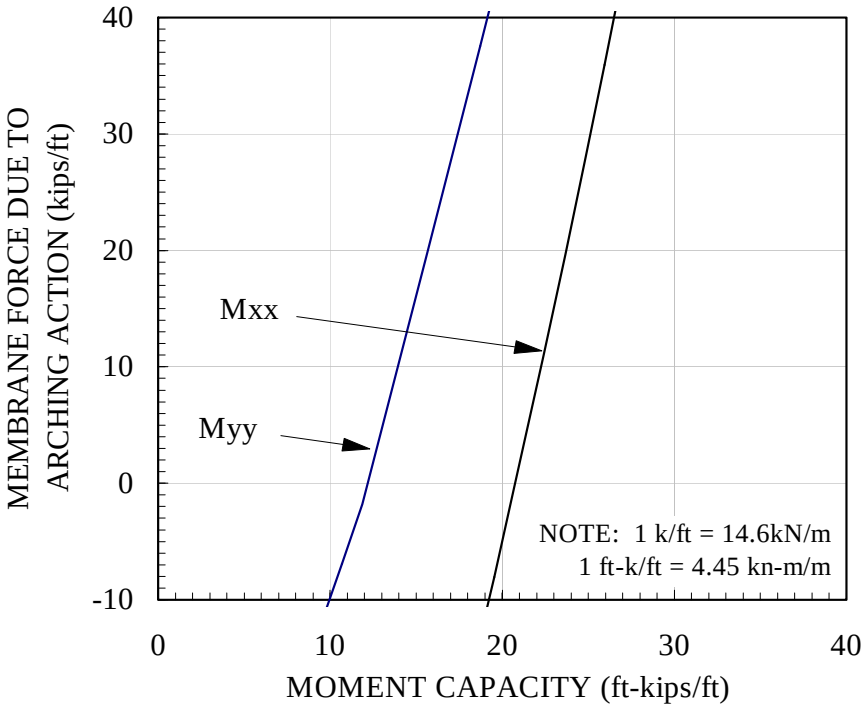

Figure 3.8: Partial interaction diagrams for precast prestressed panel test specimens.

The loads that would cause flexural failure in CIP and PCP test specimens were estimated using yield line analyses. The flexural capacities were modified as described above to include the affects of arching action. Arching action had only a slight effect on the load calculated to cause flexural failure, raising it from 232 kips (1,030 kN) to 239 kips (1,064 kN) in the CIP test specimens. The load

calculated to cause flexural failure in PCP test specimens was increased from 139 kips (619 kN) to 143 kips (636 kN) due to the effects of arching action.

Two primary reasons account for these virtually insignificant increases in calculated flexural failure load. First, increased flexural capacities in regions of membrane compression were offset by decreased flexural capacities in regions of membrane tension. Second, greater membrane compressive forces were observed in the finite element model's transverse direction (M_{XX}). Inspection of Figures 3.5 and 3.6 indicates that only a slight increase in the M_{XX} moment capacity is realized above a compressive force of about 9 kips/ft (131 kN/m) for CIP test specimens.

Predicted flexural capacities are summarized in Figures 3.9 for CIP test specimens and in Figure 3.10 for PCP test specimens. Also shown in the figures are the punching shear capacities calculated using the three equations discussed in section 3.2 of this thesis. Note that the calculated flexural capacity shown in Figure 3.10 for PCP test specimens is less than the predicted punching shear capacity calculated using the general model equation.

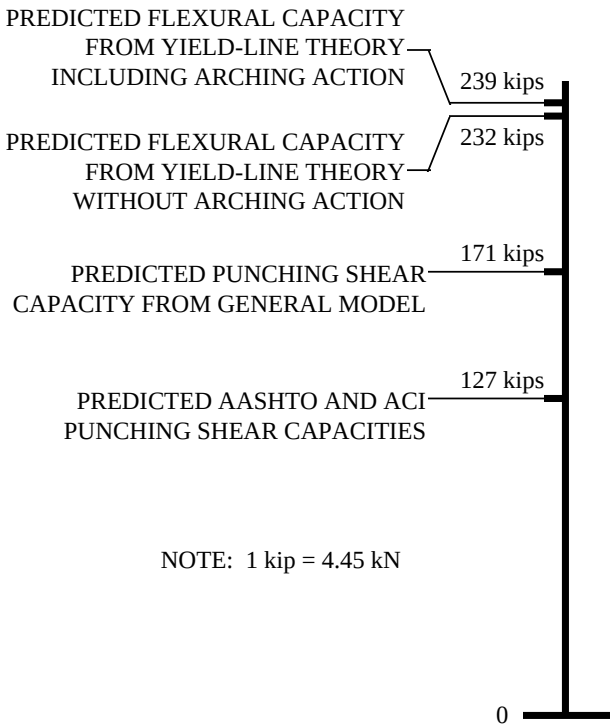

Figure 3.9: Predicted capacities for cast-in-place test specimens.

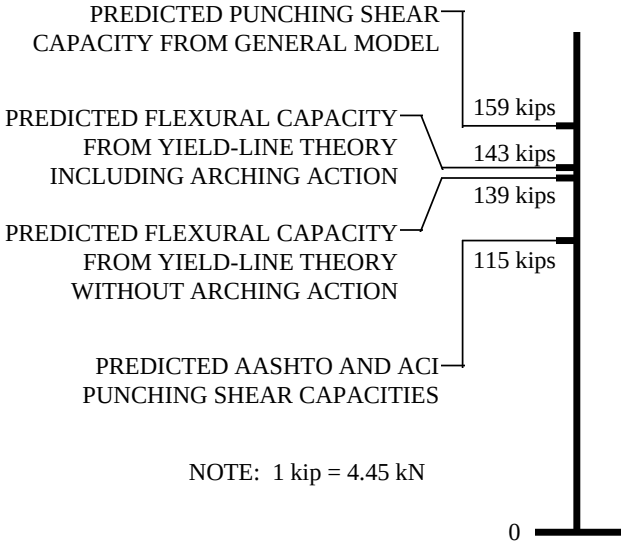

Figure 3.10: Predicted capacities for precast prestressed panel test specimens.

CHAPTER FOUR
FINITE ELEMENT ANALYTICAL MODELING

4.1 Purpose and Scope

As detailed in previous reports for this project (Whitt 1993, Kim 1994), analytical procedures were used to develop laboratory test specimens that would reflect the actual behavior of bridge decks. Analytical procedures were also required to extend the applicability of experimental test results. Both a complete bridge deck and the test specimens of this project were analyzed. The analysis considered non-linear elastic behavior due to cracking. While non-linear programs are capable of handling this directly, the Texas Department of Transportation (TxDOT) does not use such programs. To provide results that could be replicated by TxDOT, a widely available linear elastic program, SAP90™ (Wilson 1988), was used in a sequential linear procedure described below. A microcomputer version of the program was used because microcomputers are cost-effective and are commonly used by TxDOT for such computations.

Both the full bridge and the test specimens for this project were analyzed using a sequence of linear elastic analyses until the models had reached a fully cracked state. Cracking in reinforced concrete was modeled using the smeared cracking approach. In this chapter, the sequential linear elastic analysis approach used is reviewed; input parameters used in the analyses are presented; and finally, the fully cracked models are discussed and the analysis results are presented.

The primary purpose of modeling the full bridge was to relate membrane forces in test specimens to those in a real bridge, and to verify the results reported by (Fang 1986). Therefore, results from the finite element analysis regarding

membrane forces are the only results from the full-bridge model discussed in this chapter.

4.2 Sequential Linear Elastic Analysis Using Smeared Cracking

As discussed in previous reports for this project (Whitt 1993, Kim 1994), a sequence of linear elastic analyses was used to follow the non-linear elastic behavior associated with cracking in reinforced concrete. This sequence began with finite element models that had properties associated with uncracked reinforced concrete. The models were then analyzed with the full load applied. Results from these linear elastic analyses were reviewed to determine which (if any) elements exceeded their cracking stresses. These elements were then assigned new properties reflecting the stiffness of cracked reinforced concrete. The models were again analyzed, and this process was repeated until no previously uncracked elements exceeded their cracking stresses. Each iteration of the analyses was performed with the same magnitude of applied load. Cracking was idealized using the smeared crack approach. Throughout the entire element, cracking was assumed to exist perpendicular to the direction in which cracking stresses were exceeded.

4.3 Input Parameters for the Finite Element Models

The input parameters for the finite element models are discussed in this section. These include material properties, loading, support conditions, and element properties for uncracked as well as cracked elements.

4.3.1 General Information on Input Parameters

Due to symmetry, only one quadrant of the 7-feet (2.13-m) long, 6-feet (1.83-m) wide, and $7^1/_2$-inch (191-mm) thick test specimen was modeled. A finite element mesh comprised of 8-node isoparametric solid elements was used. Each unrestrained node had 3 translational degrees of freedom and no rotational degrees of freedom. The test specimen model consisted of 21 by 18 elements in plan and 7 layers in section, for a total of 2,646 elements. Each of the 7 layers corresponded either to a layer within the test specimen in which reinforcement ran in one direction only, or to a layer that was unreinforced. For example, the first (bottom) layer of elements in the model corresponded to the $2^1/_2$ inches (64 mm) of cover concrete below the test specimen's bottom mat of reinforcement. The second layer of elements in the test specimen model corresponded to the layer where bottom transverse reinforcement was placed in the test specimens. Two layers of elements in the test specimen model were used to model each two-way mat of reinforcing steel. Thus, element thicknesses in this model were dependent on the size and location of reinforcing steel in the test specimens.

Coordinate axes for the test specimen model originated at the center of the test specimen (loaded corner in the quadrant modeled). The X axis coincided with the longitudinal direction of a typical slab and girder bridge; the Y axis coincided with the transverse direction; and the Z axis went vertically upward through the thickness of the model. Figure 4.1 shows a plan and a transverse section of the analytical model. Coordinate axes are indicated in the figure. The figure also shows the initial location of spring supports and location of applied node loads, both of which are discussed later in this section.

Symmetry allowed only half of the complete bridge to be modeled. The prototypical bridge modeled had a 50 foot (15.2 m) span and a $7^1/_2$-inch (191 mm) thick isotropically reinforced deck supported on (3) W36x150 steel girders spaced at 7 feet (2.13 m) on center. The deck cantilevered 3.25 feet (1.0 m) beyond the

outside girders and was modeled as acting compositely with them. The same 8-node isoparametric solid elements used in the test specimen model were used to model the full-bridge model's deck. The full-bridge deck was modeled using 50 by 8 elements in plan and 2 layers in section for a total of 800 elements. All deck elements between girders were 12 inches square. The steel girders were modeled using three-dimensional beam elements, and composite behavior was modeled as discussed in (Fang 1986).

Coordinate axes for the full-bridge model originated on the top surface of the deck at midspan along the bridge's centerline. The X axis coincided with the longitudinal direction of a typical slab and girder bridge; the Y axis coincided with the transverse direction; and the Z axis went vertically down through the deck. Figure 4.2 shows the finite element mesh for the full-bridge model. Coordinate axes are included in the figure.

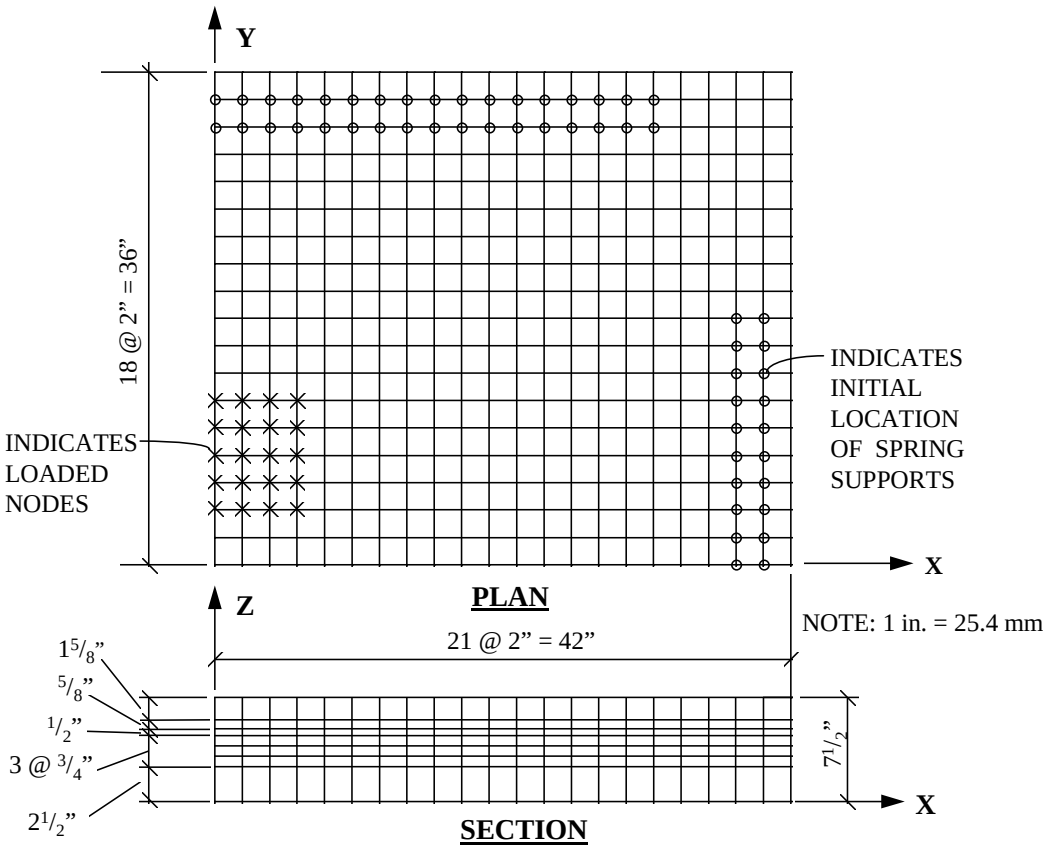

Figure 4.1: Finite element model for test specimen.

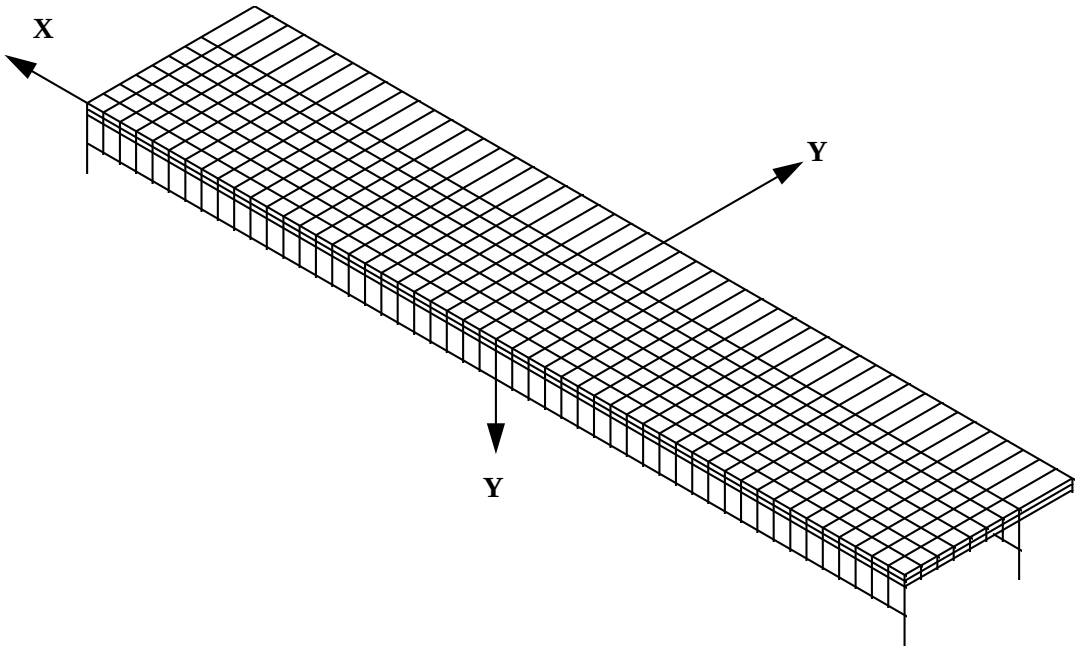

Figure 4.2: Finite element mesh for the full-bridge model.

4.3.2 Material Properties Used in the Finite Element Models

Elastic moduli and Poisson's ratios were required to develop element properties for the finite element models. A value of 29,000 ksi (200,000 MPa) was used for the elastic modulus of steel. The elastic modulus of concrete used in the test specimen model was established from the design compressive strength, f'_c, of 6,000 psi (41.3 MPa) used for test specimens, and the ACI equation $E_C = 57{,}000\sqrt{f'_c}$. This resulted in an elastic modulus for concrete of 4,415 ksi (30,420 MPa). The elastic modulus for concrete used in the full-bridge model was 3,605 ksi (24,840 MPa), based on the design compressive strength of 4,000 psi (27.6 MPa) specified by TxDOT for Class S concrete (Standard Specifications for Construction of Highways, Streets, and Bridges 1993). A Poisson's ratio of 0.15 was used for reinforced concrete in both models. These material properties

were used to derive element stiffness properties for the models, discussed later in this Chapter.

4.3.3 Loading Parameters Used in the Finite Element Models

To simulate the distribution of load used in the test specimens, discrete point loads were applied at appropriate nodes on the top surface of the model. The locations of these nodal loads are indicated in Figure 4.1. The magnitude of each point load was based on the loaded area tributary to that particular node. Thus, nodes on the interior region of the loaded area had loads twice as large as those at the edge of the loaded region, and four times larger than those at the corners of the loaded region. The total load applied to the quadrant of the test specimen modeled was 37.5 kips (167 kN), corresponding to a total specimen load of 150 kips (668 kN).

The spacing of loads applied to the full-bridge model was established from the dimensions for a standard AASHTO truck. These loads were applied as nodal loads in the same manner as that described above for the test specimen loads, and the locations of applied node loads are shown in Figure 4.2. In order to compare analytical results from the test specimen model directly with those from the full-bridge model, the maximum wheel loads from a standard AASHTO HS20-44 truck were scaled up to the same 150 kip (668 kN) load applied to the test specimen model. The total load applied to the full-bridge model was nearly 9.4 times the standard AASHTO HS20-44 truck loading. This is illustrated in Figure 4.3.

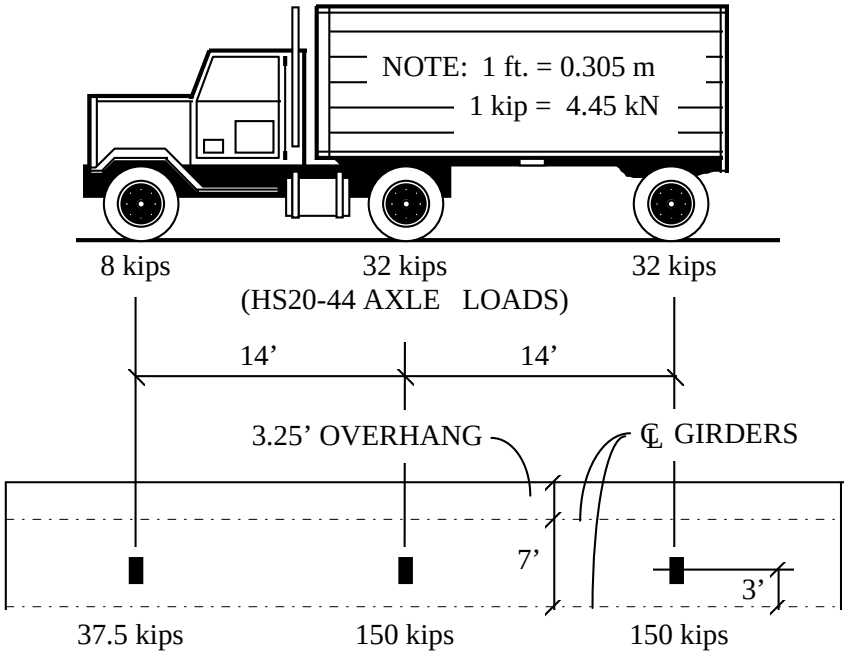

Figure 4.3: AASHTO design loads for a standard HS20-44 truck, and loads applied to the full-bridge finite element model.

4.3.4 Support Conditions Used in the Finite Element Models

Because the test specimens were simply supported at their edges on $^1/_2$-inch (13-mm) thick by 5-inch (127-mm) wide, 70-durometer neoprene bearing strips (see Chapter 5), spring supports were used in the analytical model. Based on AASHTO recommendations for neoprene, a modulus for compression of about 10 ksi (68.9 MPa) was calculated. This resulted in a spring constant in the Z direction of 100 kips/in (17.5 kN/mm). A shear modulus of 0.15 ksi (1.03 MPa), recommended by AASHTO for 70-durometer neoprene, resulted in spring constants for the X and Y directions of 1.5 kips/inch (0.26 kN/mm). Although springs were also used to support the girders in the full-bridge model, their

influence on the behavior of the deck was minimal and will not be discussed further.

Spring supports were provided in the test specimen model in two rows along supported edges, as shown in Figure 4.1. Spring supports near the outer corner of the modeled quadrant were released to prevent tension. This was done as part of the iterative sequential linear elastic modeling process.

Nodes in the test specimen model were restrained against lateral translation along the two lines of symmetry (the X and Y axes). All nodes in the X-Z plane were restrained against translation in the Y direction. Similarly, all nodes in the Y-Z plane were restrained against translation in the X direction. Nodes in the plane of symmetry in the bridge model were restrained against out-of-plane translation (Y direction) as well as rotation about vertical and longitudinal axes. These nodes were allowed to translate in the plane of symmetry and to rotate about axes normal to this plane.

4.3.5 Uncracked Element Properties

Based on the material properties presented above, properties for uncracked elements were derived for each of the 7 layers in the test specimen model, and for both layers in the full-bridge model. The stress-strain relation used for modeling uncracked elements is shown in Eq. 4.1 for a layer in the test specimen model with reinforcement parallel to the X axis:

$$\begin{Bmatrix} \varepsilon_X \\ \varepsilon_Y \\ \varepsilon_Z \\ \gamma_{XY} \\ \gamma_{YZ} \\ \gamma_{ZX} \end{Bmatrix} = \begin{bmatrix} \frac{1}{E_{X_{eff}}} & \frac{-\nu}{E_Y} & \frac{-\nu}{E_Z} & 0 & 0 & 0 \\ \frac{-\nu}{E_{X_{eff}}} & \frac{1}{E_Y} & \frac{-\nu}{E_Z} & 0 & 0 & 0 \\ \frac{-\nu}{E_{X_{eff}}} & \frac{-\nu}{E_Z} & \frac{1}{E_Z} & 0 & 0 & 0 \\ 0 & 0 & 0 & \frac{1}{G_C} & 0 & 0 \\ 0 & 0 & 0 & 0 & \frac{1}{G_C} & 0 \\ 0 & 0 & 0 & 0 & 0 & \frac{1}{G_C} \end{bmatrix} \begin{Bmatrix} \sigma_X \\ \sigma_Y \\ \sigma_Z \\ \tau_{XY} \\ \tau_{YZ} \\ \tau_{ZX} \end{Bmatrix} \qquad (4.1)$$

where

$\varepsilon_X, \varepsilon_Y, \varepsilon_Z$ = normal strains in the X, Y, and Z directions respectively

$\gamma_{XY}, \gamma_{YZ}, \gamma_{ZX}$ = shearing strains in the X-Y, Y-Z, and Z-X planes respectively

$E_{X_{eff}}$ = effective elastic modulus in the X direction (see below)

E_Y, E_Z = elastic moduli in the Y and Z directions respectively

ν = Poisson's ratio for concrete

G_C = shear modulus for concrete = $\frac{E_C}{2(1+\nu)}$

$\sigma_X, \sigma_Y, \sigma_Z$ = normal stresses in the X, Y, and Z directions respectively

$\tau_{XY}, \tau_{YZ}, \tau_{ZX}$ = shear stresses causing shear strains in the X-Y, Y-Z, and Z-X planes respectively

The effective elastic modulus in the X direction, $E_{X_{eff}}$, was calculated as

$$E_{X_{eff}} = E_C [1 + \rho_{eff} (n-1)] \quad (4.2)$$

where

E_C = elastic modulus for concrete

ρ_{eff} = effective tensile steel ratio for a layer = $\frac{A_S}{s\ t}$

A_S = area of 1 reinforcing bar in a layer (or area of a bundle of bars)

s = spacing of reinforcing bars in a layer (or spacing of bundles)

t = thickness of layer (diameter of bar)

n = modular ratio = $\frac{E_S}{E_C}$

A Poisson's ratio of 0.15 was used for all uncracked elements. The shear modulus, G_C, was calculated to be 1,920 ksi (13,200 MPa) for all uncracked elements in the test specimen model, and 1,630 ksi (11,250 MPa) for uncracked elements in the full-bridge model. The modular ratio for the test specimen model was calculated to be 6.57, based on 6,000-psi (41.3-MPa) concrete and an elastic modulus for steel of 29,000 ksi (200,000 MPa). The modular ratio for the full-bridge model was calculated to be 8.04, based on 4,000-psi (27.6-MPa) concrete. Values of ρ_{eff} and E_{eff} are summarized in Table 4.1 for all layers in the test specimen model. Because the full bridge was modeled with an isotropically reinforced deck using only 2 layers of elements, both layers of elements had the same properties. These uncracked element properties are shown in Table 4.2.

Table 4.1: Summary of effective reinforcement ratios and effective moduli for uncracked elements in the test specimen model.

	X-Direction		Y-Direction	
LAYER	ρ_{eff}	$E_{X_{eff}}$ (ksi)	ρ_{eff}	$E_{Y_{eff}}$ (ksi)
1	0	4,415	0	4,415
2	0	4,415	0.1956	9,220
3	0.0978	6,820	0	4,415
4	0	4,415	0	4,415
5	0.0333	5,235	0	4,415
6	0	4,415	0.0496	5,635
7	0	4,415	0	4,415

Note: 1 ksi = 6.89 MPa

Table 4.2: Summary of effective reinforcement ratios and effective moduli for uncracked elements in the full-bridge model.

	X-Direction		Y-Direction	
LAYER	ρ_{eff}	$E_{X_{eff}}$ (ksi)	ρ_{eff}	$E_{Y_{eff}}$ (ksi)
Both	0.00593	3,755	0.00593	3,755

Note: 1 ksi = 6.89 MPa

4.3.6 Cracked Element Properties

With each iteration of the analysis, element stresses were evaluated to determine if cracking stresses were exceeded. This section discusses the criteria used to evaluate element cracking stresses, and presents the calculated properties for cracked elements used in the analysis.

Based on Kupfer's biaxial stress criterion (Kupfer 1969), a cracking stress of $0.1 f'_c$ was used for plain concrete. For 6,000 psi (41.3 MPa) concrete, this results in a cracking stress (σ_{cr}) of 0.60 ksi (4.13 MPa) for elements corresponding to unreinforced layers, and for cracking parallel to reinforcing steel in elements corresponding to reinforced layers in the test specimens. The relation

$$\varepsilon_{cr} = \frac{\sigma_{cr}}{E_C} \tag{4.3}$$

results in a cracking strain (ε_{cr}) of 0.000136. Cracking stresses perpendicular to reinforcing steel were calculated using the relation

$$\sigma_{cr} = \varepsilon_{cr} E_{eff} \tag{4.4}$$

Elements that exceeded their respective cracking stresses were assigned new properties corresponding to the cracked state. The stress-strain relation used for modeling cracked elements is shown in Eq. 4.5 for a layer in the test specimen model with reinforcement parallel to the X axis and cracked perpendicular to the X axis:

$$\begin{Bmatrix} \varepsilon_X \\ \varepsilon_Y \\ \varepsilon_Z \\ \gamma_{XY} \\ \gamma_{YZ} \\ \gamma_{ZX} \end{Bmatrix} = \begin{bmatrix} \frac{1}{\rho_{eff} E_S} & 0 & 0 & 0 & 0 & 0 \\ 0 & \frac{1}{E_Y} & \frac{-\nu}{E_Z} & 0 & 0 & 0 \\ 0 & \frac{-\nu}{E_Z} & \frac{1}{E_Z} & 0 & 0 & 0 \\ 0 & 0 & 0 & \frac{1}{\beta G_C} & 0 & 0 \\ 0 & 0 & 0 & 0 & \frac{1}{G_C} & 0 \\ 0 & 0 & 0 & 0 & 0 & \frac{1}{\beta G_C} \end{bmatrix} \begin{Bmatrix} \sigma_X \\ \sigma_Y \\ \sigma_Z \\ \tau_{XY} \\ \tau_{YZ} \\ \tau_{ZX} \end{Bmatrix} \quad (4.5)$$

where β is a factor of 0.5 and the other quantities are as defined above. The term $\rho_{eff} E_S$ is seen to be the effective modulus for the cracked element. As developed in previous reports for this project (Whitt 1993, Kim 1994), the term $\frac{1}{\beta G_C}$ represents the remaining shear stiffness in the cracked plane, due to aggregate interlock and dowel action.

Element cracking stresses and effective moduli for cracked elements are summarized in Table 4.3 for all layers in the test specimen model, and in Table 4.4 for both layers in the full-bridge model.

Table 4.3: Summary of cracking stresses and effective moduli for cracked elements in the test specimen model.

	X-Direction		Y-Direction	
LAYER	σ_{cr} (ksi)	$E_{X_{eff}}$ (ksi)	σ_{cr} (ksi)	$E_{Y_{eff}}$ (ksi)
1	0.600	0	0.600	0
2	0.600	0	1.250	5,670
3	0.927	2,840	0.600	0
4	0.600	0	0.600	0
5	0.712	967	0.600	0
6	0.600	0	0.766	1,440
7	0.600	0	0.600	0

Note: 1 ksi = 6.89 MPa

Table 4.4: Summary of cracking stresses and effective moduli for cracked elements in the full-bridge model.

	X-Direction		Y-Direction	
LAYER	σ_{cr} (ksi)	$E_{X_{eff}}$ (ksi)	σ_{cr} (ksi)	$E_{Y_{eff}}$ (ksi)
Both	0.417	172	0.417	172

Note: 1 ksi = 6.89 MPa

4.4 Smeared Crack Propagation in the Test Specimen Model

The sequential linear elastic method of analysis used was an iterative process. Initial cracking was observed in only the bottom layer of the analytical model. This cracking was observed perpendicular to both the X and Y axes and only near the applied load. Elements that exceeded their respective cracking stresses were assigned new properties consistent with cracked concrete as discussed above, and the model was analyzed again. This second iteration produced cracking extending through the third layer (up from the bottom); unlike the first iteration, the cracked elements extended to the outer edges of the model. Elements exceeding their cracking stresses extended along the outer edges toward the model's outer corner. This pattern of cracked elements (propagating upward through layers and outward along the supported edges toward the outer corner) continued slowly through 7 iterations.

The 7th iteration produced only a few new elements that exceeded their cracking stresses. After this iteration, cracking perpendicular to the X axis had propagated higher into the model, through 6 layers, than did cracking perpendicular to the Y axis, which had propagated through only 4 layers.

The 8th iteration was the first in which spring supports indicating tension reactions (near the outer corner) were removed. Only 3 spring supports were released on this iteration. This induced additional cracking, which progressed in the same manner as previously described. It also produced tension in springs which were previously in compression. The process of cracking additional elements and releasing spring supports, which indicated tension reactions, continued through a total of 19 iterations. The 19th analysis iteration indicated no additional elements exceeding their cracking stresses and all remaining spring supports in compression. Figure 4.4 shows the location of spring supports remaining in compression after the final iteration of analysis.

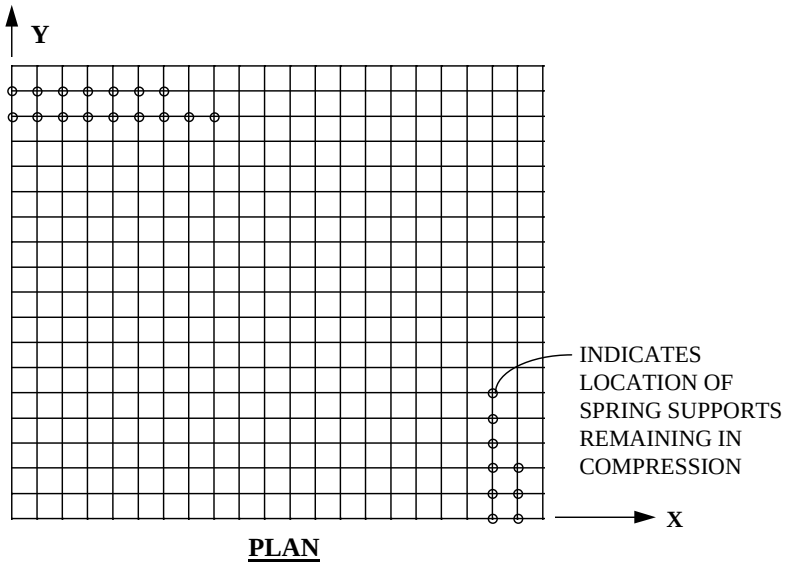

Figure 4.4: Spring supports in compression after the final analysis iteration.

4.5 Fully Cracked Models

Cracking was extensive in the fully cracked test specimen model. Cracking perpendicular to the X axis extended up through all but the top layer, and some tension in the bottom of the top layer was observed. In all cracked layers, cracking perpendicular to the X axis extended towards the corner along the supported edge.

Cracking perpendicular to the Y axis did not extend as far up into the model as did cracking perpendicular to the X axis. Cracking perpendicular to the Y axis extended up through the 5th layer, but not through the 6th layer. This cracking did not exhibit the pronounced orientation towards the corner observed in cracking perpendicular to the X axis. It was slightly more extensive along the supported edge than in the loaded region, with one exception. Cracking perpendicular to the Y axis that occurred in Layer 5 (the highest level cracked in

this direction) did not occur directly under the loaded region, but rather began just outside the load footprint and extended along the X axis to the supported edge.

Figure 4.5 illustrates the typical smeared cracking pattern that developed in the fully cracked analytical model for test specimens. It shows the extent of cracking in Layer 3, which has properties associated with the level in the test specimen that was reinforced with #6 bars at 6 inches (152 mm) on center parallel to the X axis. Only the pattern of cracking (not crack widths) is illustrated in the figure.

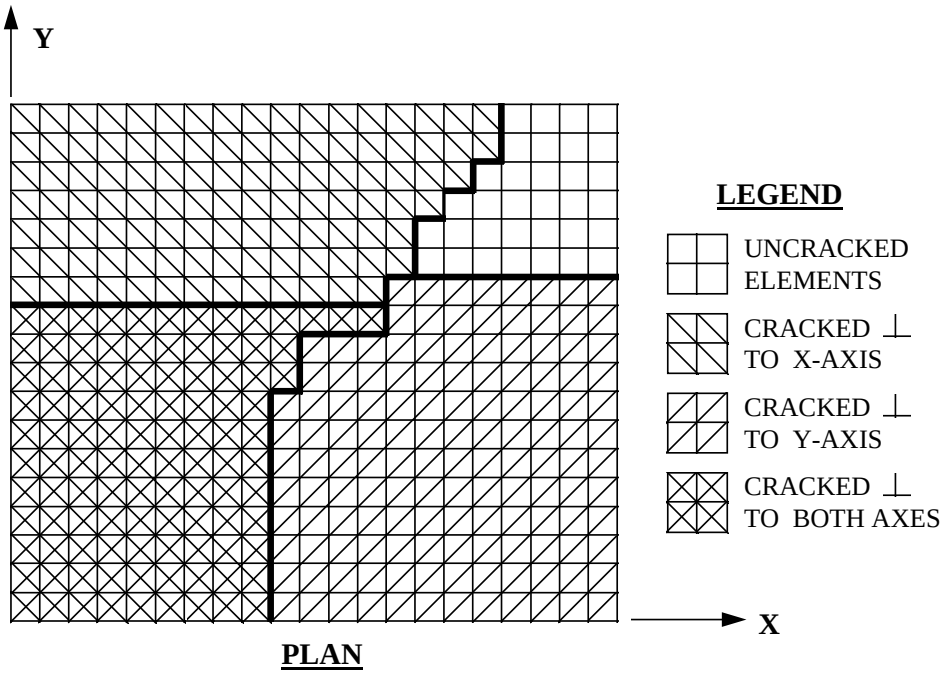

Figure 4.5: Typical pattern of smeared cracking observed in the analytical model for test specimens (layer 3 of the analytical model of test specimens is shown).

Cracking in the full-bridge model was observed in both directions only under the loaded areas. Longitudinal cracking extended along the entire length of the bridge between girders in the bottom layer, and only over the interior girder in the top layer.

4.6 Analytical Results from the Fully Cracked Test Specimen Model

This section presents the results from the smeared crack finite element analysis of a cast-in-place (CIP) test specimen. The analytical results are compared with experimental results in Chapter 8 of this thesis. Deflections, reactions, flexural stresses and shearing stresses are presented here. Also included are normal stresses acting on the assumed failure plane, which were calculated using results from the finite element analysis. Arching action observed in the analytical model for test specimens is presented as well. Membrane forces observed in the full-bridge analytical model are presented in Section 4.7.

4.6.1 Deflections

The maximum downward deflection observed in the analytical model was 0.247 inches (6.27 mm), which occurred at the origin of the coordinate axes (center of loaded region). The maximum uplift occurred at the outer corner of the model, and was 0.181 inches (4.60 mm). A load-deflection curve was generated from the sequence of linear elastic analyses, and is shown in Figure 4.6. The final point on the curve is that of the final analysis iteration. The load and corresponding deflection for each intermediate point plotted were generated by first calculating the ratio of deflection from the intermediate analysis to the deflection from the final analysis. Both the 150 kip (668 kN) applied load and the total deflection from the intermediate analysis were factored by this ratio to obtain the intermediate load and deflection points plotted in the figure. The result is a

curve that closely approximates the complete load-deflection response of the analytical model. The 4 intermediate points plotted are those from the 1st, 2nd, 3rd and 8th analyses.

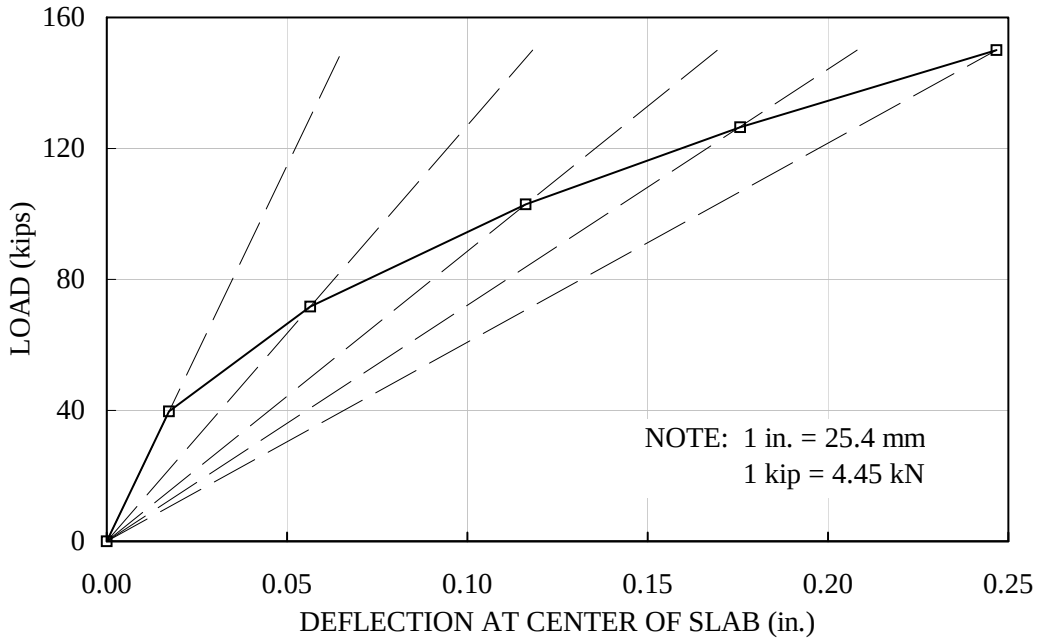

Figure 4.6: Load-deflection curve calculated from results of the sequential linear analysis of test specimens.

4.6.2 Reactions

Figure 4.4 shows those spring supports that remained in compression after the final analysis iteration. Spring reactions varied from about zero to a maximum of about 3.6 kips (16 kN) at the interior springs located near the Y axis (transverse axis). Figures 4.7 and 4.8 illustrate the magnitude of vertical spring reactions along lines parallel to the X and Y axes respectively. The maximum

lateral spring reaction was 0.17 kips (0.76 kN), at the inboard spring on the Y axis. All other lateral spring reactions were less than about 0.07 kips (0.3 kN).

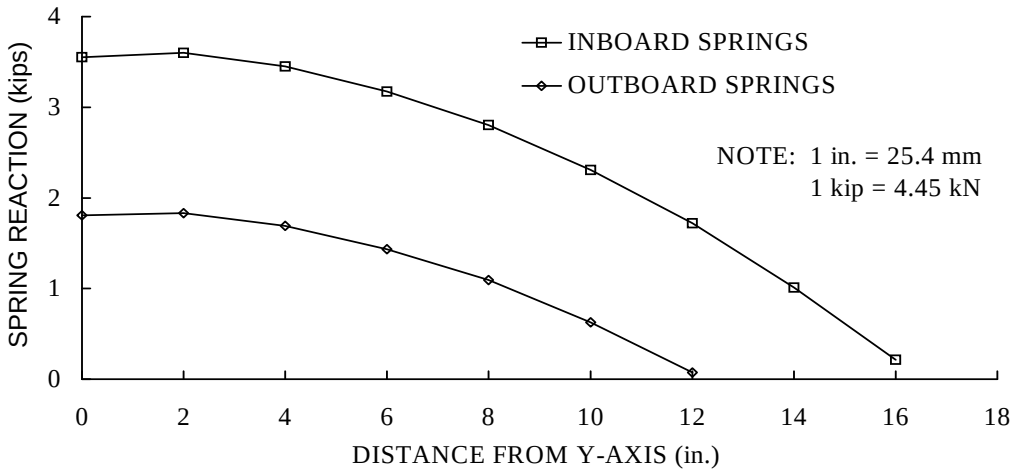

Figure 4.7: Vertical spring reactions for springs parallel to the X axis.

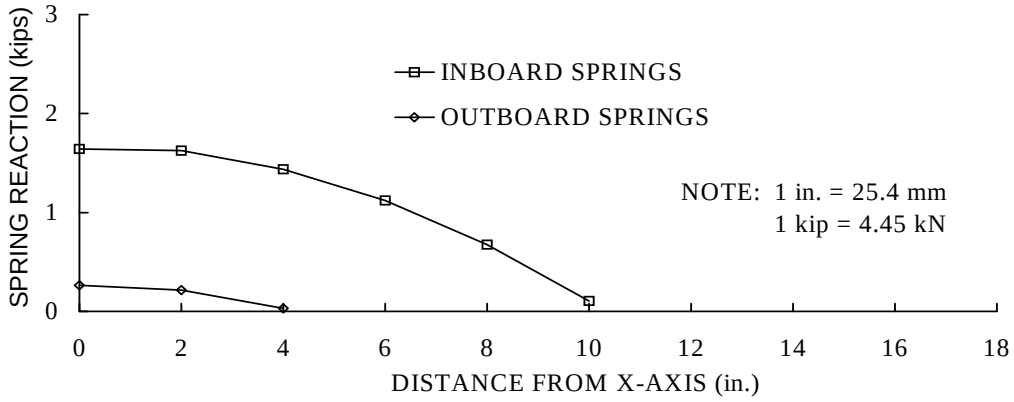

Figure 4.8: Vertical spring reactions for springs parallel to the Y axis.

4.6.3 Flexural Stresses in the Test Specimen Model

Two-way action was clearly evident in the analytical model. Maximum flexural compressive stresses were observed not at the loaded corner of the specimen, but rather near the center of the actual loaded area of the quadrant modeled. The maximum compressive stresses were 6.67 ksi (46.0 MPa) and 6.00 ksi (41.3 MPa) in the transverse and longitudinal directions respectively. Flexural compression in the longitudinal direction was observed only in the top layer (layer 7). In the transverse direction, flexural compression was present not only in the top layer, but through most of the 6th layer as well.

Tensile stresses from the finite element analysis were converted to equivalent reinforcing steel stresses by using the relations

$$n_{eff} = \frac{E_S}{E_{eff}} \tag{4.6}$$

and

$$f_S = n_{eff}\,\sigma \tag{4.7}$$

where

n_{eff} = the effective modular ratio for a given layer

E_S = elastic modulus for steel

E_{eff} = effective elastic modulus as defined in equation (4.2)

f_S = reinforcing steel stress for a given layer

σ = element stress (at center of element) from finite element analysis

Values of effective moduli are summarized in Table 4.1 for uncracked elements and in Table 4.3 for cracked elements. It should be noted that the effective modular ratio for uncracked elements is not equal to the effective modular ratio for cracked elements. Values of effective modular ratios (n_{eff}),

maximum finite element stresses in the direction of reinforcing (σ_{max}), and calculated reinforcing steel stresses ($f_{S\ max}$) are summarized in Table 4.5 for all reinforced layers in the test specimen model. Note that Layer 6 has reinforcing steel parallel to the Y axis and is uncracked across this reinforcement; thus, the value for n_{eff} tabulated for that layer is for uncracked elements.

Table 4.5: Summary of effective modular ratios, maximum element stresses and reinforcing steel stresses for reinforced layers of the finite element test specimen model.

LAYER	DIRECTION	n_{eff}	σ_{max} (ksi)	$f_{S\ max}$ (ksi)
2	YY	5.11	6.80	34.8
3	XX	10.2	4.38	44.7
5	XX	30.0	0.674	20.2
6	YY	5.15*	0.0644	0.33

* Value for uncracked elements

Note: 1 ksi = 6.89 MPa

4.6.4 Shearing Stresses in the Test Specimen Model

Maximum absolute values of shear stress occurred in the transverse direction at the outside edge of the loaded area. This maximum value was 0.70 ksi (4.8 MPa). Figure 4.9 shows a plot of transverse shearing stresses, τ_{YZ}, along the Y axis from the origin of coordinate axes to the outside edge of the model. Values are for stresses at the center of elements in Layer 6.

Shearing stresses in the longitudinal direction, τ_{XZ}, were large at the "toe" of the loaded area. Values in this region were about 0.47 ksi (3.2 MPa).

However, maximum absolute values of longitudinal direction shear stress, τ_{XZ}, occurred outside the lines of springs supporting the transverse edge at about mid-depth of the model. These values were about -0.48 ksi (-3.2 MPa), which is slightly greater in magnitude than those near the loaded area. Figure 4.10 shows a plot of longitudinal shearing stresses, τ_{XZ}, along a line parallel to the X axis and going through the center of the loaded region for the quadrant modeled. Values are for stresses at the center of elements in Layer 6.

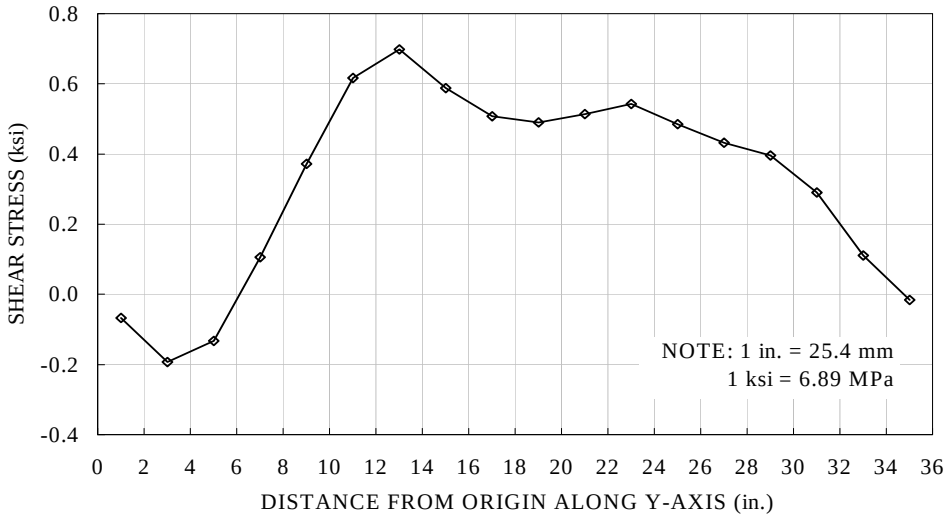

Figure 4.9: Transverse shearing stresses, τ_{YZ}, along the Y axis of the test specimen model.

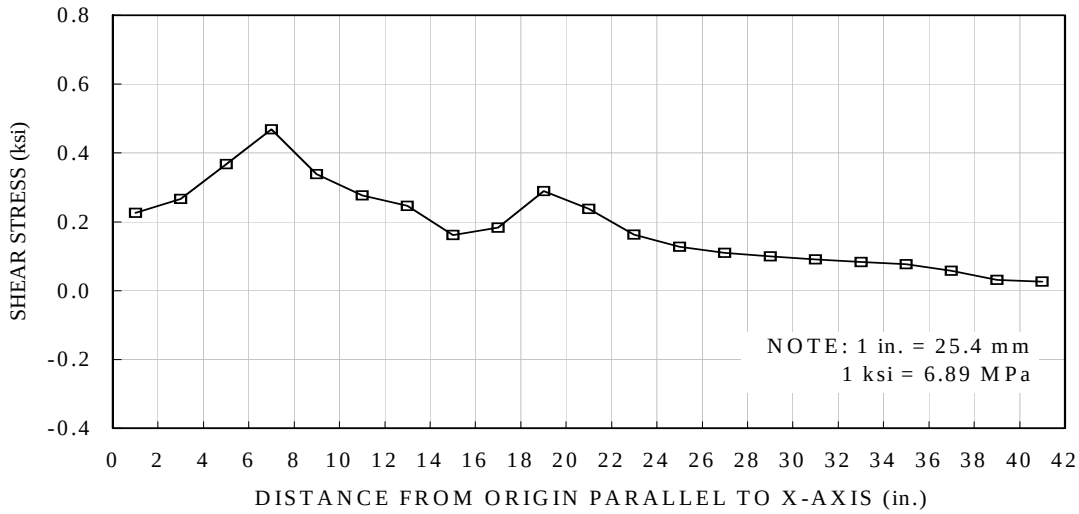

Figure 4.10: Longitudinal shearing stresses, τ_{XZ}, parallel to the X axis of the test specimen model.

4.6.5 Stresses Acting on the Assumed Failure Plane

The assumed failure plane was discussed in detail in Section 3.2 of this thesis. Stresses normal to this failure plane were calculated at its intersection with both the X and Y coordinate axes of the finite element test specimen model. These normal stresses were calculated using stresses at the center of elements (joint stresses were used at the top and bottom surfaces of the model) and the following stress transformation equation:

$$\sigma_N = \frac{\sigma_X + \sigma_Z}{2} + \frac{\sigma_X - \sigma_Z}{2}\cos 2\theta + \tau_{XZ}\sin 2\theta \qquad (4.8)$$

where

σ_N = stress normal to failure plane

θ = angle between σ_X (horizontal) and the normal to the failure plane

and the other quantities are as defined in Equation (4.1). The subscripts in the above are for the intersection of the assumed failure plane with the X-Z plane. The subscript "x" is replaced with subscript "y" for calculation of stresses at the intersection with the Y-Z plane. Calculated normal stresses on either side of the failure plane were linearly interpolated to determine the normal stresses at the location of the failure plane

Figures 4.11 and 4.12 show the stresses acting normal to the assumed failure plane at its intersection with the X-Z and Y-Z planes respectively. The disproportionate tensile "spikes" in the figures correspond to reinforced layers in the model. If these points are not plotted the stress distribution becomes nearly linear from the point of maximum tensile stress to the model's bottom surface. The figures indicate that the stresses normal to the failure plane in the transverse direction were greater than those in the longitudinal direction. Also indicated by the figures is that compression exists normal to the assumed failure plane in the flexural compression zone of the section.

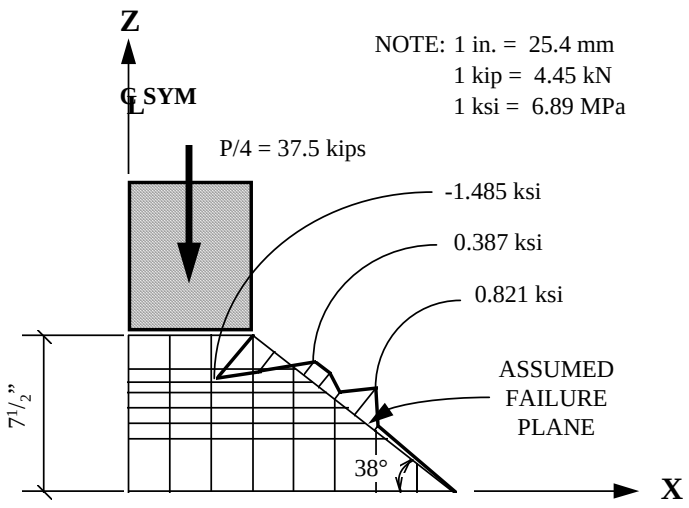

SECTION

Figure 4.11: Stresses normal to the assumed failure plane at its intersection with the X-Z plane (longitudinal axis) of the analytical model. Tension is positive.

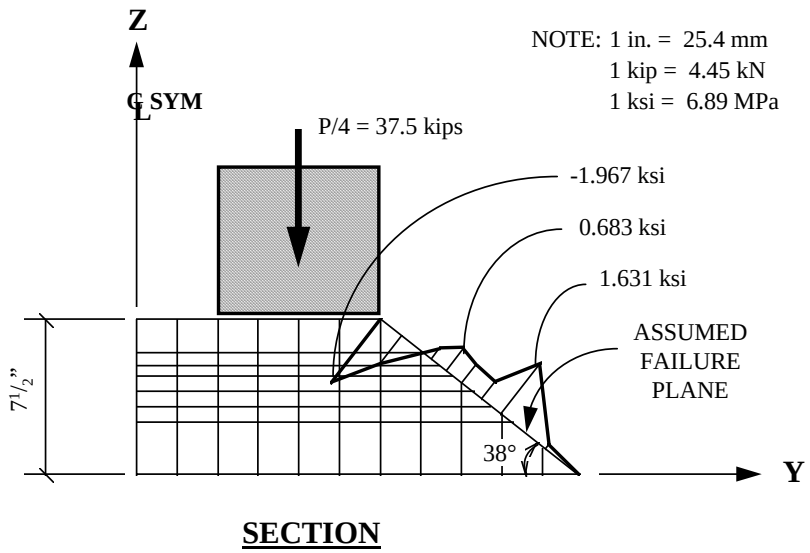

Figure 4.12: Stresses normal to the assumed failure plane at its intersection with the Y-Z plane (transverse axis) of the analytical model. Tension is positive.

4.6.6 Arching Action in the Test Specimen Model

Arching action was detected in the finite element model by summing in-plane forces through the model's thickness. At a specific (X,Y) coordinate location, element stresses at the center of elements (in the X and Y coordinate directions) were multiplied by the element thickness to obtain the total element force per unit width (again, in the X and Y coordinate directions). These forces were then summed over the thickness of the model (7 layers thick) to obtain the net force per unit width acting parallel to coordinate axes at that specific (X,Y) coordinate location. The net force calculated by this technique is the membrane force per unit width resulting from arching action. Orthogonal components of membrane stress were calculated by simply dividing these net forces by the total

thickness of the model. An example of these calculations for the elements at the origin of coordinates is included in Appendix B.

Calculated membrane stresses clearly show that arching action was present in the finite element model. Figure 4.13 illustrates the orthogonal components of membrane stress calculated as described above for elements along the perimeter of the test specimen model. As shown in the figure, membrane compressive stresses existed along and in the direction of coordinate axes while membrane tensile stresses existed around and parallel to the exterior edges. This is in absolute agreement with the commonly used description of arching action in bridge decks: a compression dome surrounded by membrane tension. Also indicated by the figure is that membrane compressive stresses in the transverse direction were larger than those in the longitudinal direction. As discussed in Section 4.6.2, it should be noted that horizontal reactions were practically negligible and could not have been responsible for the membrane compressive stresses shown in Figure 4.13.

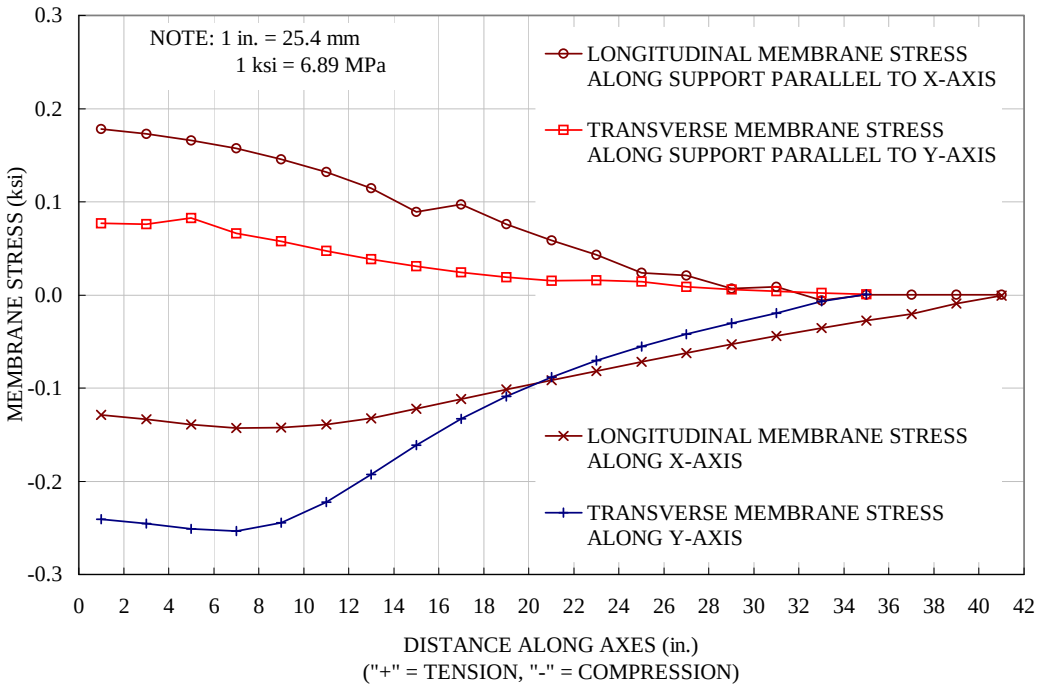

Figure 4.13: Orthogonal components of membrane stresses observed in the finite element test specimen model.

Slight irregularities in the curves indicating tensile membrane stress are likely the result of abrupt changes in tensile and shear stiffnesses that occur at the boundaries between cracked and uncracked elements in the model. These irregularities also correspond to locations where spring supports were removed, and the model lifts off its supports.

The membrane tensile stresses shown in Figure 4.13 explain the increased crack width near the outside edges of the test specimens, which was discussed in Section 4.5 and illustrated in Figure 4.5. Also noted in Section 4.5 was that smeared cracking perpendicular to the X axis was more extensive than that perpendicular to the Y axis along the outside edges of the model (see Figure 4.5). This is partially explained by the fact that (as shown in Figure 4.13) membrane

tensile stresses along the edge parallel to the X axis were larger than those along the edge parallel to the Y axis.

Orthogonal components of membrane forces were calculated as described above at locations throughout the finite element test specimen model. Figure 4.14 is a plan view of the finite element test specimen model showing the distribution of longitudinal membrane forces using force contours. Figure 4.15 shows transverse membrane force contours and Figure 4.16 shows average membrane force contours in the test specimen model. The compression dome under the loaded area is clearly illustrated in these figures. Contours within zones of membrane tension are shown dashed in the figures.

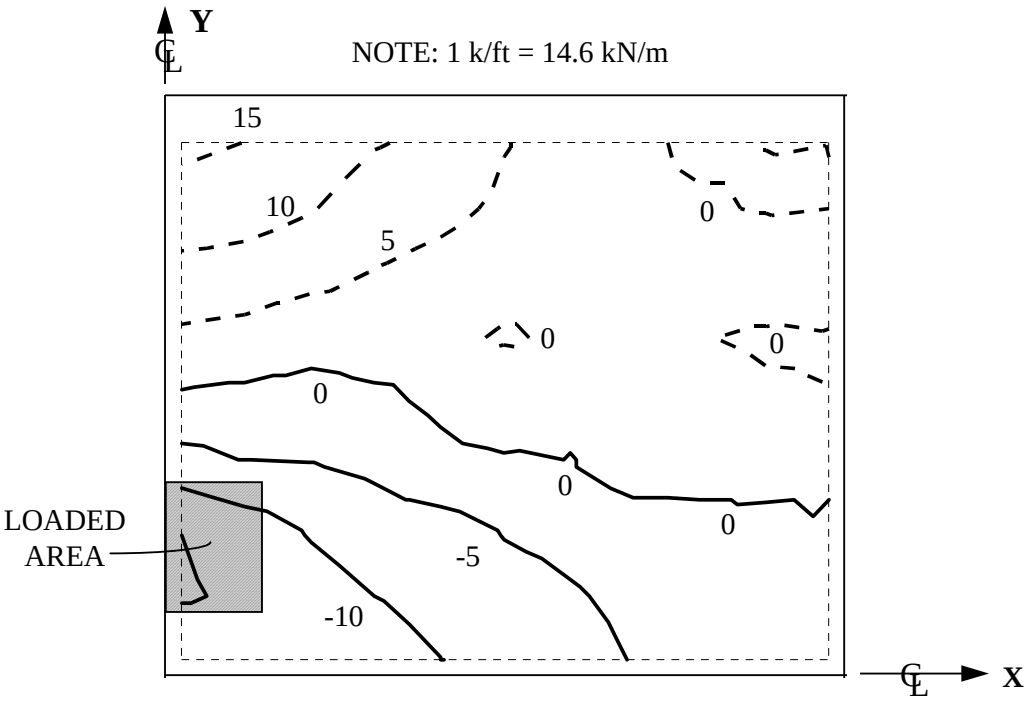

Figure 4.14: Longitudinal membrane force contours from the finite element test specimen model. Units are kips/ft. Tension (dashed lines) is positive; compression (solid lines) is negative.

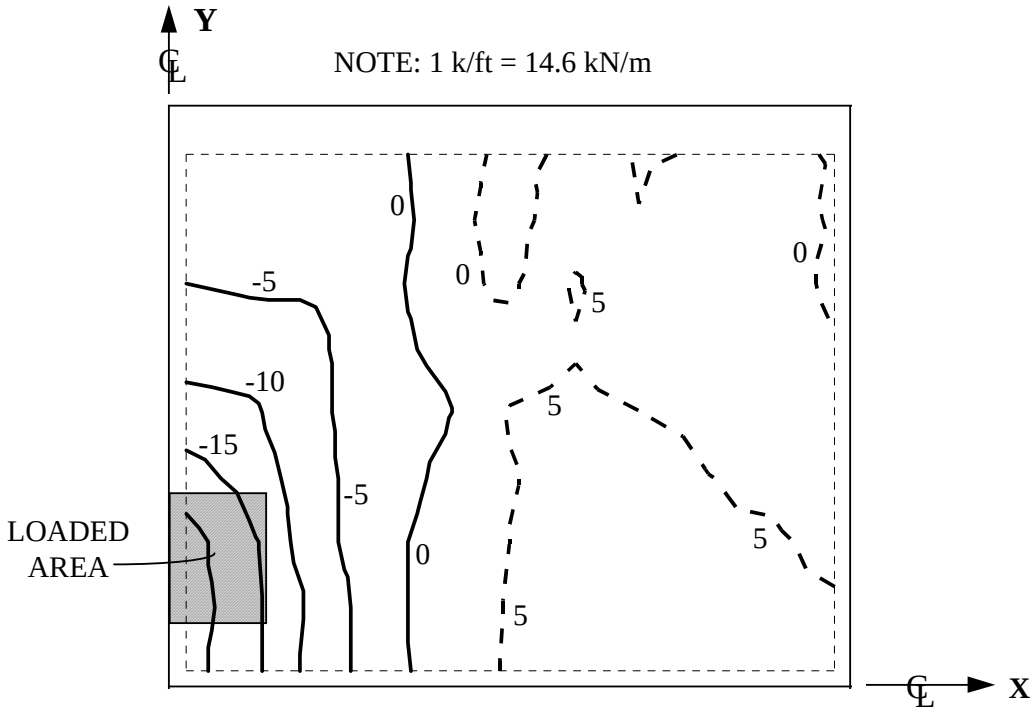

Figure 4.15: Transverse membrane force contours from the finite element test specimen model. Units are kips/ft. Tension (dashed lines) is positive; compression (solid lines) is negative.

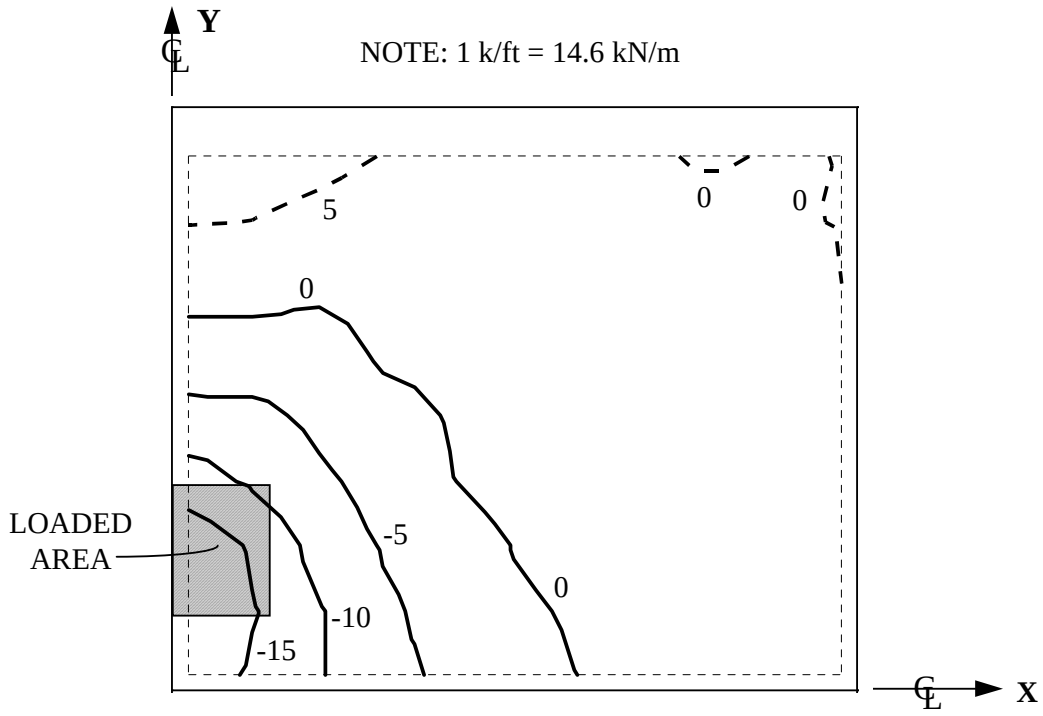

Figure 4.16: Average membrane force contours from the finite element test specimen model. Units are kips/ft. Tension (dashed lines) is positive; compression (solid lines) is negative.

4.7 Arching Action in the Full-Bridge Model

Membrane forces were calculated in the full-bridge model in the same manner as that described above for the test specimen model. Longitudinal membrane forces were not calculated because the analysis results include the longitudinal compression resulting from composite flexural behavior between the deck and girders. Figure 4.17 shows the transverse membrane forces calculated over the interior girder along the centerline of the bridge (line of symmetry). The wheel loads applied to the deck between girders are also shown in the figure.

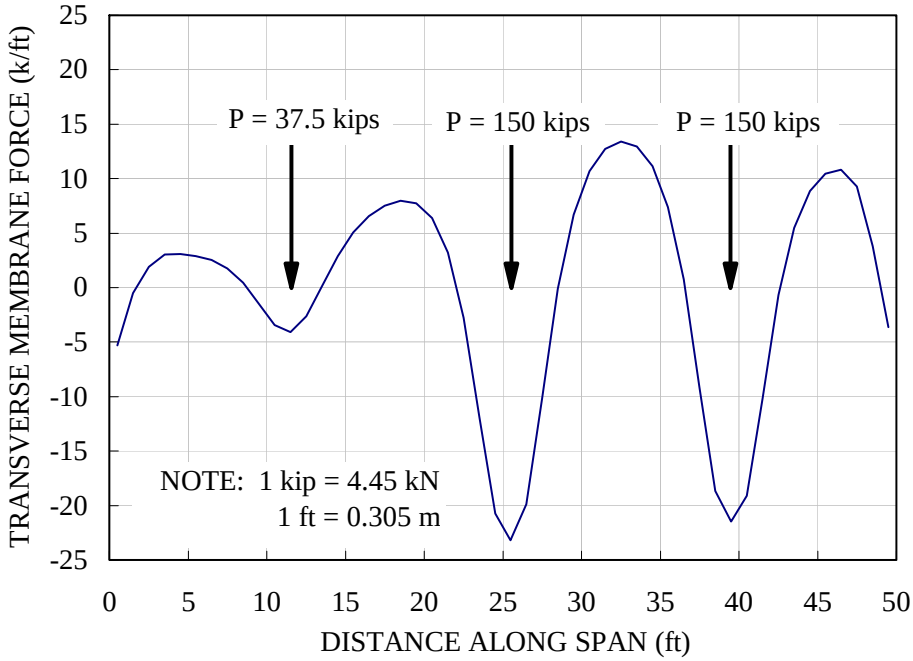

Figure 4.17: Transverse membrane forces from the finite element model of the full bridge (along the centerline). Tension is positive.

By summing the transverse compressive forces shown in Figure 4.17, and dividing this sum by the length over which the compressive forces act and again by the applied load, an average transverse compressive force per unit width as a function of applied load results. This calculation resulted in an average transverse compressive force of about 1.87 kips/ft (27.3 kN/m) for each 20 kips (89 kN) of applied load. This agrees reasonably well with results observed by (Fang 1986). Although some discrepancies are apparent in the results reported in that reference, it is apparent that the average transverse compressive force calculated by their finite element analysis was about 2.33 kips/ft (34.0 kN/m) at 20 kips (89 kN) of applied load. Experimental results from tests on a full-scale bridge reported in that reference indicated the slightly lower value of about 2.08 kips/ft (30.4 kN/m) at 20 kips (89 kN) of applied load.

Transverse membrane force contours from the full-bridge finite element model are shown in Figure 4.18 for the 7-feet (2.13-m) wide region between girders under the 150-kip (668-kN) trailing load. Transverse membrane force contours from the finite element test specimen model are shown in Figure 4.15 for the quadrant modeled. By simply mirroring those contours about lines of symmetry (coordinate axes), a contour plot for the entire test specimen was created, and is shown in Figure 4.19.

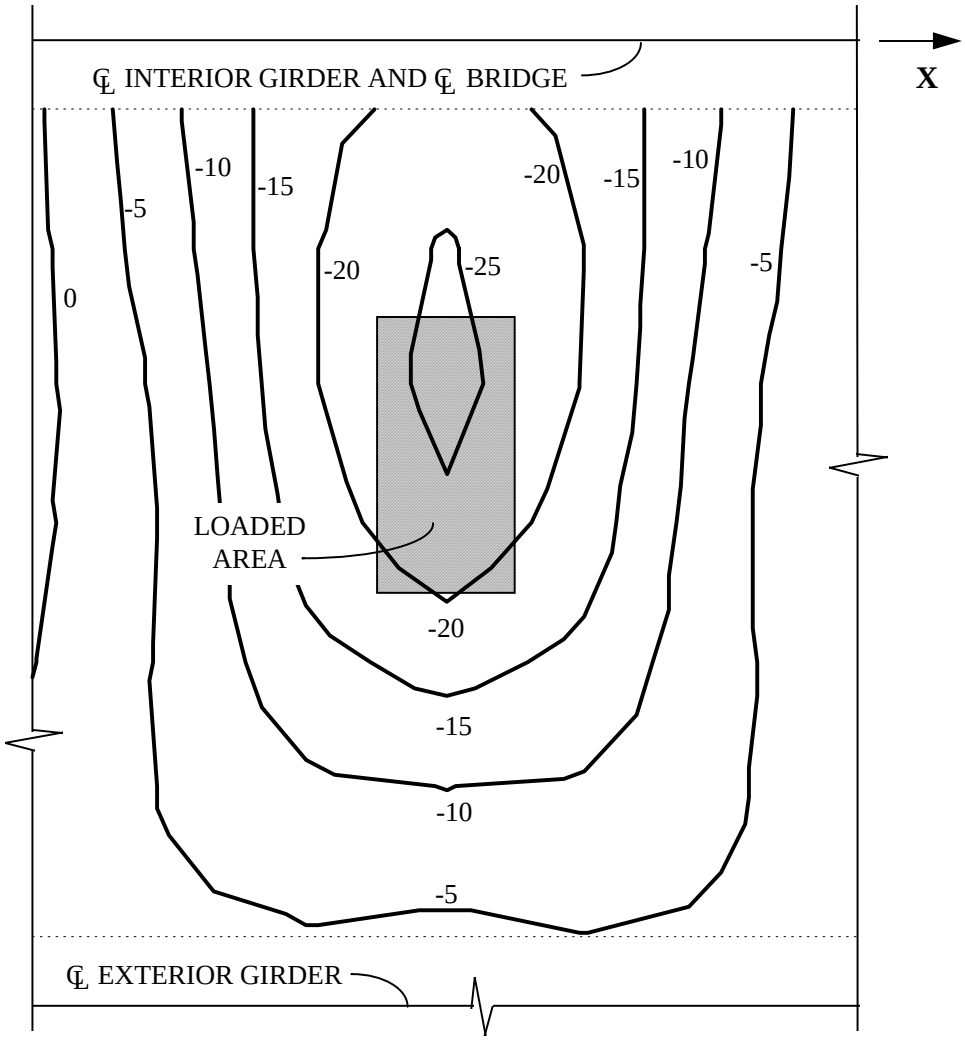

Figure 4.18: Transverse membrane force contours from the finite element model of the full bridge. Units are kips/ft and tension is positive

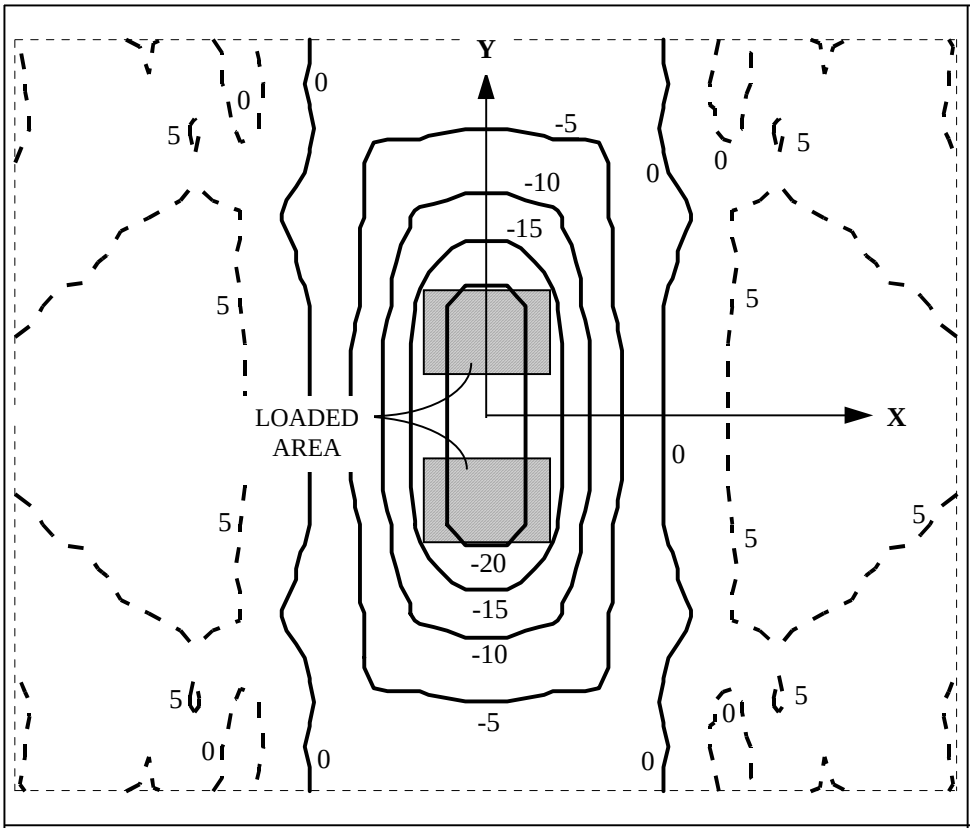

Figure 4.19: Transverse membrane force contours from the finite element test specimen model. Units are kips/ft. Tension (dashed lines) is positive; compression (solid lines) is negative..

Comparison of Figures 4.18 and 4.19 indicates that transverse membrane forces in the full bridge model were only slightly greater in magnitude than those in the test specimen model. Also, these membrane forces were confined to a relatively narrow length (parallel to the longitudinal axis) in the test specimen model, whereas in the full bridge model the transverse membrane forces are distributed over a longer region in this direction.

CHAPTER FIVE
EXPERIMENTAL TEST PROGRAM

5.1 Introduction

The development of the test setup and test specimens has been covered in detail in previous reports for this project (Whitt 1993, Kim 1994), and is not be repeated here. After static tests and low cycle pulsating fatigue tests had been completed, the test frame was modified to provide additional stiffness and strength and to isolate the specimen support frame and test specimens from the reaction frame. The modified test setup was used to complete pulsating fatigue tests on cast-in-place (CIP) test specimens. All precast prestressed panel (PCP) test specimens were tested using the modified test frame.

Problems associated with the movement of large loads in the rolling fatigue test setup persisted. The amount of time and financial resources expended on the rolling fatigue test setup eventually began to jeopardize the entire testing program. As a result, planned rolling fatigue tests were not performed, and the rolling fatigue test setup was dismantled. Results of rolling fatigue tests previously performed in Japan and discussed in Section 9.4 of this thesis were used to correlate results from pulsating fatigue tests with those from rolling fatigue tests.

This chapter discusses the modified test frame that was used for all tests conducted since the last report (1305-2). Material characteristics, instrumentation and loading parameters for both CIP and PCP test specimens are discussed. Methods of system control and data acquisition are discussed as well.

5.2 Modified Test Frame

Wide-flange columns acquired from laboratory stock were used to replace the steel channel columns that had been used in the original test setup. Each new column was anchored to the structural floor slab with four, 1-inch (25.4-mm) diameter high-strength anchor bolts. The anchor bolts were tensioned to about 40 ksi (276 MPa) in order to minimize the effects of fatigue loading. Replacing the original steel channel columns with wide-flange columns anchored to the structural floor slab served to isolate the reaction frame from the support frame and test specimens. The new wide-flange column arrangement also stiffened the test setup by eliminating the flexible connections between the support frame and steel channel columns. Additional stiffness was provided by shortening the reaction beam by about 6 inches (152 mm) and providing stiff connections to the new wide-flange columns. Figure 5.1 shows an overall view of the test setup after these modifications.

Test specimens had slight irregularities on their bottom surfaces wherever joints were present in the wooden forms used for construction. Friction between the support frame and these irregularities produced loud rubbing noises when the first specimen was tested in pulsating fatigue in the modified frame. To ensure uniform bearing of test specimens on the support frame (and to eliminate the noise), $^1/_2$-inch-thick by 5-inch-wide (13-mm-thick by 127-mm-wide), 70-durometer neoprene bearing strips were added to the top of the support frame. After glue failed to hold the neoprene strips in place, thin metal strips were tack welded to the top of the support frame outside the neoprene bearing strips to prevent the neoprene from "walking" out of position. Except for minor adjustments (such as re-tightening bolts), no other test setup modifications were required through the duration of testing. Figure 5.2 shows a dimensioned plan of

the modified test setup. The longitudinal section A-A indicated on the plan is shown in Figure 5.3.

PHOTO

Figure 5.1: Overall view of the modified pulsating fatigue test setup.

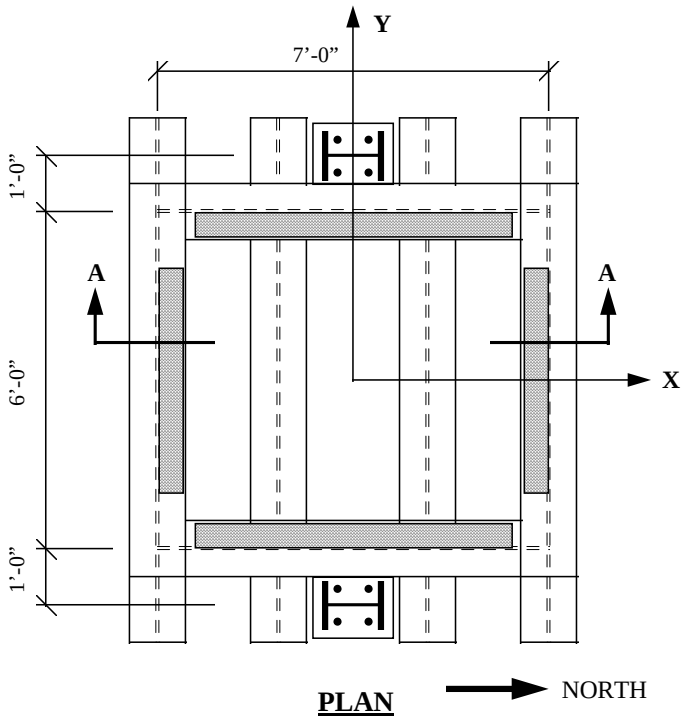

Figure 5.2: Dimensioned plan of the modified pulsating fatigue test setup.

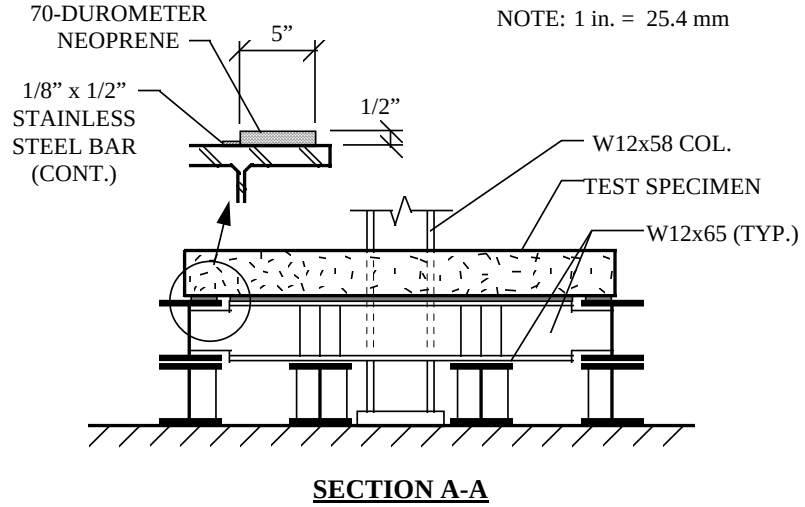

Figure 5.3: Longitudinal section through the modified pulsating fatigue test setup.

5.3 Nomenclature Used to Identify Test Specimens

Throughout this thesis, test specimens are referred to by identification numbers, whose meaning is explained below. CIP test specimens were assigned identification numbers such as "S2P110." The "S" signifies a CIP test specimen; the "2" identifies the second specimen tested at a specific load range; and the "P110" identifies the maximum load applied to the specimen as 110 kips (490 kN). Minimum cyclic loads were about 10% of the maximum load. Thus, S3P145 identifies the third CIP pulsating fatigue test specimen, tested under a cyclic sinusoidal load ranging from a minimum of 15 kips (67 kN) to a maximum of 145 kips (645 kN). PCP specimens were identified by the same nomenclature, except that a "P" was added to signify a PCP test specimen. For example, PS1P55 is the identification given to one of the PCP specimens.

5.3.1 Cast-in-Place Test Specimens

Development of CIP test specimens as well as design details were covered in previous reports for this project (Whitt 1993, Kim 1994). Relevant details are reviewed in this section.

All CIP test specimens were 6 feet (1.83 m) wide, 7 feet (2.13 m) long and $7^1/_2$ inches (191 mm) thick. In order to prevent flexural failure, very large areas of flexural reinforcement were used, along with a relatively large clear cover (to prevent splitting failures) for bottom bars. All CIP test specimens were provided with the same reinforcement and construction details. Figure 5.4 shows a typical plan of CIP test specimens. Coordinate axes as discussed in Chapter 4 are included in the figure. The longitudinal section A-A indicated on the plan is shown in Figure 5.5.

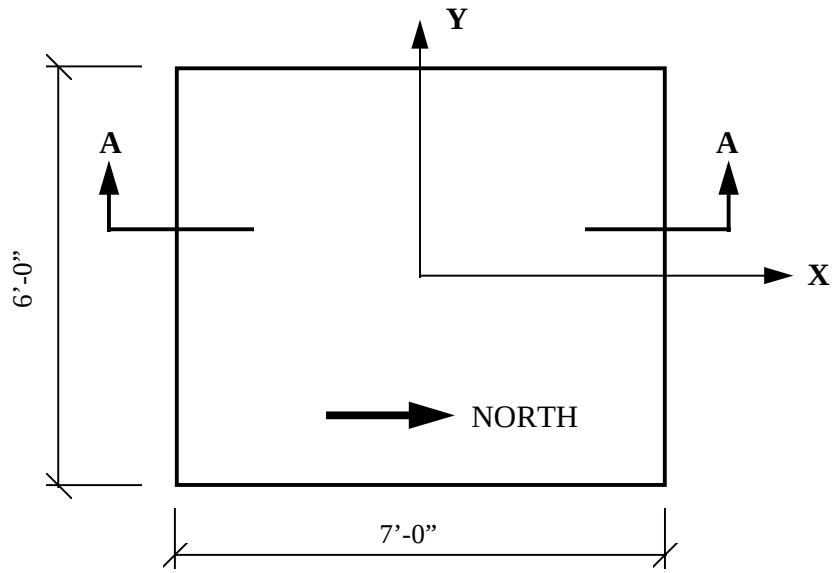

PLAN

Figure 5.4: Plan of cast-in-place test specimens.

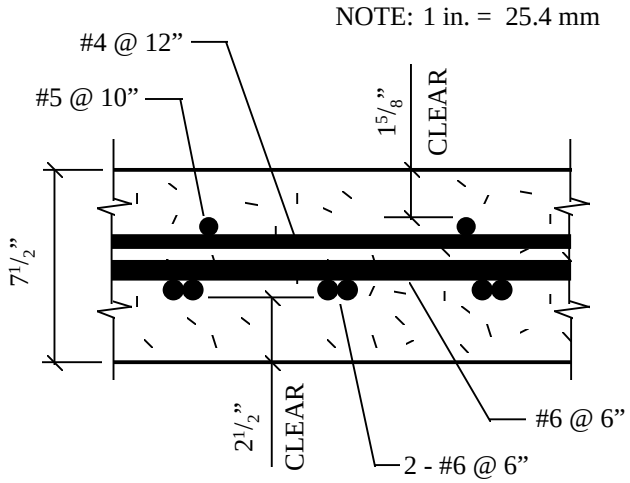

TYPICAL LONGITUDINAL SECTION A-A

Figure 5.5: Typical longitudinal section through cast-in-place test specimens.

5.3.2 Precast Prestressed Panels and Test Specimens

Four precast prestressed panels were donated to this research effort by Austin Prestressed Company. They were standard 8 feet (2.44 m) long, 6 feet 5 inch (1.96 m) wide and 4 inch (102 mm) thick panels and were selected from a storage yard of “rejected” and “extra” panels. The panels apparently complied with structural requirements, but had been rejected because they did not comply with tolerances for their plan dimensions. That defect was irrelevant to their performance in this project. Because panels had to fit between reaction frame columns of the existing test setup, size was the main criterion used for panel selection. The panels were designed in accordance with Texas Department of Transportation (TxDOT) standard details and cast in January of 1991. The panels had a raked finish on the top surface with grooves parallel to prestressing strands. Pertinent details for these panels are shown in Figure 5.6. Details shown are for the as-built condition of the donated panels, and conform to details shown on TxDOT Standard Detail Sheet PCP 1 of 2. The welded wire fabric reinforcement used in the panels and shown in Figure 5.6 was determined from samples cut from the first static test specimen after failure.

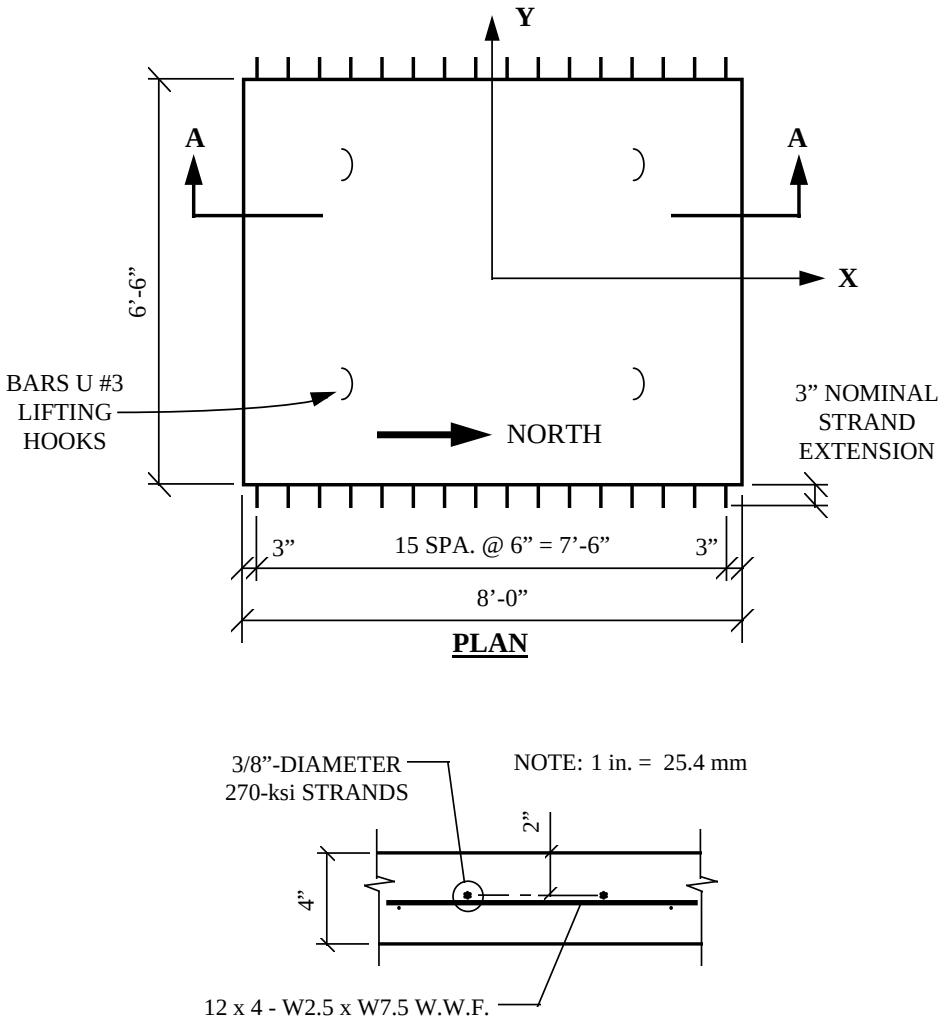

Figure 5.6: Precast prestressed panel details.

Precast prestressed panels were topped with $3^1/_4$ inches (83 mm) of cast-in-place concrete, reinforced with #4 bars at 6-inch (152-mm) centers each way. A 3-inch (76 mm) wide "turn-down" edge was provided along the edges with

protruding strands; the complete PCP test specimens were 8 feet (2.44 m) long and 7 feet (2.13 m) wide (in the transverse direction). This was the maximum width possible consistent with a $^1/_2$-inch (13-mm) gap between test specimens and the reaction frame columns. This width was maximized in order to provide as much development length for prestressing strands as possible. To accommodate this, the 3-inch (76-mm) nominal strand extensions were bent up nearly 90 degrees into the cast-in-place "turn-down" edge. Bending the ends of strands up may have slightly decreased the required strand transfer length as well.

Several hours before cast-in-place topping was placed, the panels were wetted. They were kept in a surface-dry state, but mottled in appearance, until the topping was placed, in order to obtain a good bond between the panels and the cast-in-place topping.

Flexural capacity of the PCP test specimens was primarily controlled by the reinforcement used in the donated panels. Calculations discussed in Chapter 3 indicated that reasonable measures would not raise the calculated flexural capacity above the calculated punching shear capacity. In order to provide as much depth for the reinforcement cast in the topping, the transverse bars were set $^1/_2$ inches (13 mm) clear above the panels. Figure 5.7 shows a plan and a typical section through PCP test specimens. Coordinate axes as discussed in Chapter 4 are included in the figure.

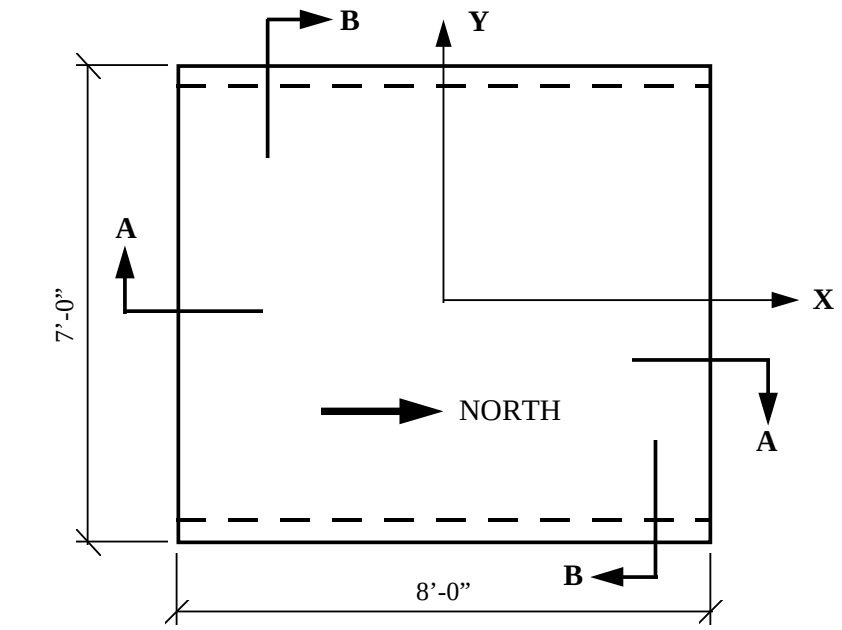

PLAN

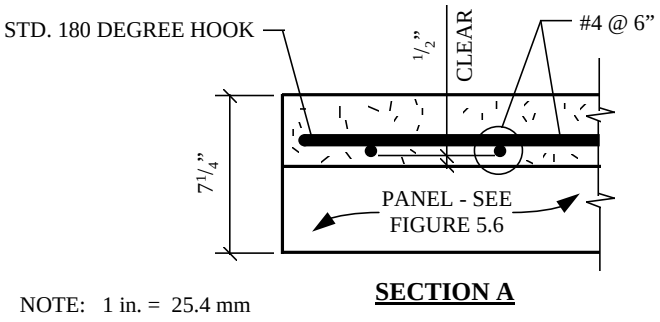

SECTION A

NOTE: 1 in. = 25.4 mm

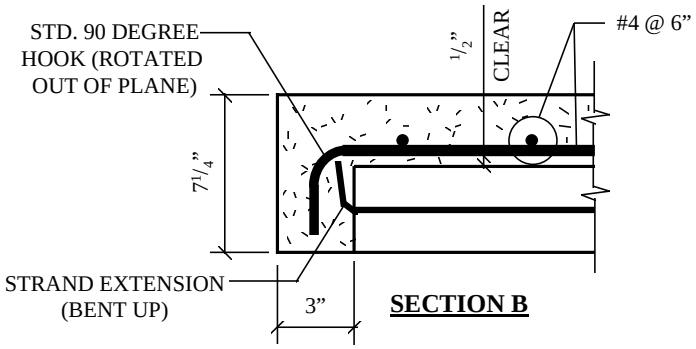

SECTION B

Figure 5.7: Precast prestressed panel test specimen details.

5.3.3 Material Characteristics

Concrete used for the CIP specimens and for topping in the PCP specimens was TxDOT Type S (Standard Specifications for Construction of Highways, Streets, and Bridges 1993). Because only $^1/_2$ inch (13 mm) clear was provided between the top of the precast panels and the reinforcing steel placed in the topping, a maximum aggregate size of $^3/_8$ inches (10 mm) was specified for the topping concrete. That same maximum aggregate size was used in the CIP test specimens, due to the congested reinforcing steel layout. Mild reinforcing steel bars were ASTM A615, Grade 60. Standard 90º or 180º hooks were used on all bars in order to prevent bond and development failures. Additional material characteristics, including cylinder strength test results, are included in Appendix D.

5.3.4 Instrumentation

Strain gages were attached to reinforcing steel bars at discrete locations in both CIP and PCP test specimens. No strain gages were attached to reinforcement placed in the precast prestressed panels, because those panels had been completely finished before they were donated. Concrete strain gages were attached to the top surface of the precast prestressed panels before topping was placed. Before testing, concrete strain gages were attached to the top and bottom surfaces of CIP and PCP test specimens. The locations of gages are shown in Figure 5.8 for CIP test specimens, and in Figure 5.9 for PCP test specimens. All strain gages were electrical resistance-type gages.

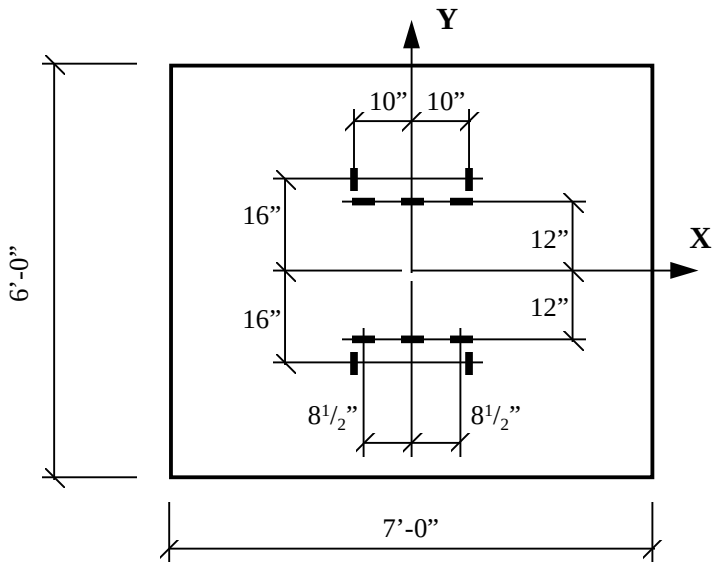

GAGES ON TOP BARS

NOTE: 1 in. = 25.4 mm

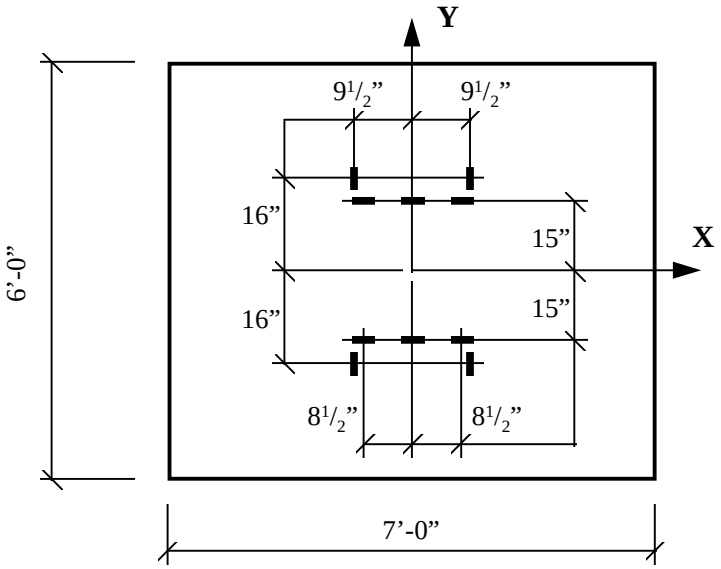

GAGES ON BOTTOM BARS

Figure 5.8: Locations of strain gages used in cast-in-place test specimens.

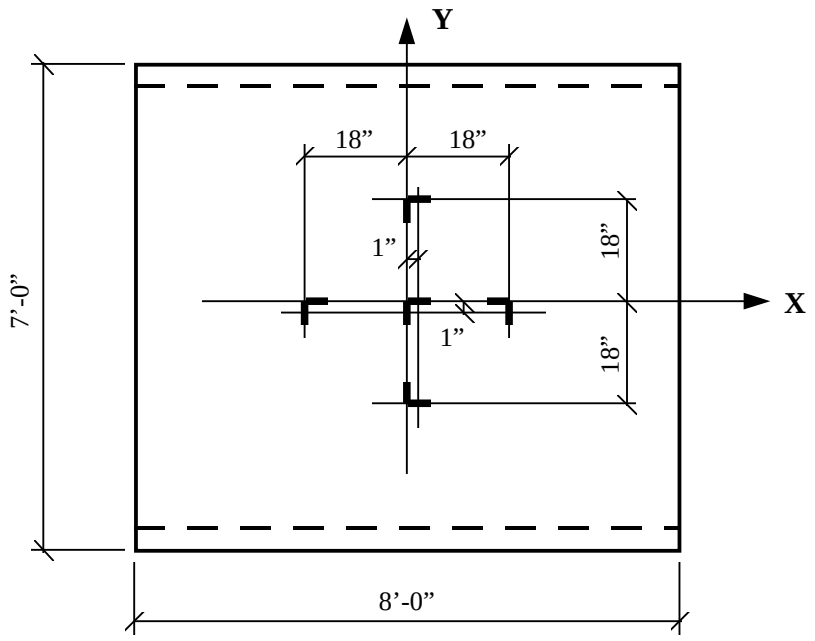

Figure 5.9: Locations of strain gages used in precast prestressed panel test specimens.

Deflections were measured from the underside of test specimens using 2-inch (51-mm) linear potentiometers supported above the structural floor slab by very stiff stands. They were located at the east and west edges of test specimens (just inside the support frame's edges) and at the center of test specimens. In an effort to quantify the unexpected flexural behavior observed in the PCP test specimens, additional linear potentiometers were located below Specimen PS1P77. The linear potentiometer layouts used are illustrated in Figure 5.10.

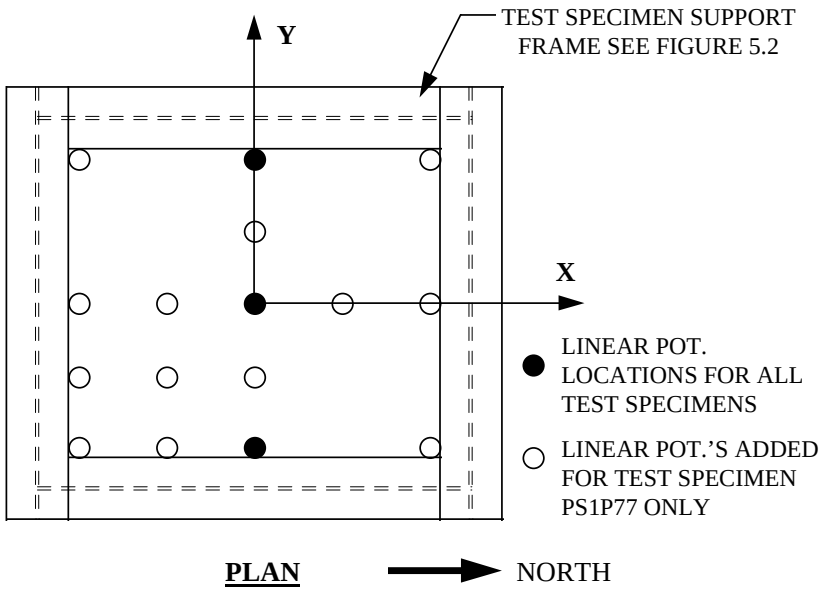

Figure 5.10: Layout of linear potentiometers used to measure deflections in test specimens.

5.3.5 Loading Parameters

Loads were applied to test specimens using a 300-ton (2,670-kN) hydraulic ram, which, as discussed in previous reports for this project (Whitt 1993, Kim 1994), was specially fitted with 1-inch (25-mm) ports to increase the maximum rate of hydraulic fluid flow through the ram. Hydraulic fluid was supplied to the ram by an electric pump capable of delivering 70 gpm (0.00442 m^3/sec) at 3,000 psi (20.7 MPa).

Applied loads were monitored using a 180-kip (801-kN), fatigue-rated load cell. During fatigue cycling of Specimen S3P110, the load cell experienced fatigue-induced debonding of some of its strain gages. A 200-kip (890-kN), non-fatigue rated load cell was used to complete the testing on Specimen S3P110.

The original fatigue-rated load cell was quickly repaired and used for all other tests.

Roller skids were used for static tests on the CIP test specimens. The roller skids applied load to the test specimens over a 16-inch (406-mm) by 24-inch (610-mm) area. As discussed in previous reports for this project (Whitt 1993, Kim 1994), the roller skids were replaced with a 3-inch (76-mm) thick steel plate. A pair of steel plates, in contact with this plate, rested on $^1/_2$-inch (13-mm) thick, 70-durometer neoprene pads, which transferred load directly to test specimens. The pair of plates had a 14-inch (356-mm) by 24-inch (610-mm) loading footprint. Figure 5.11 shows the loading footprint used for CIP pulsating fatigue test specimens.

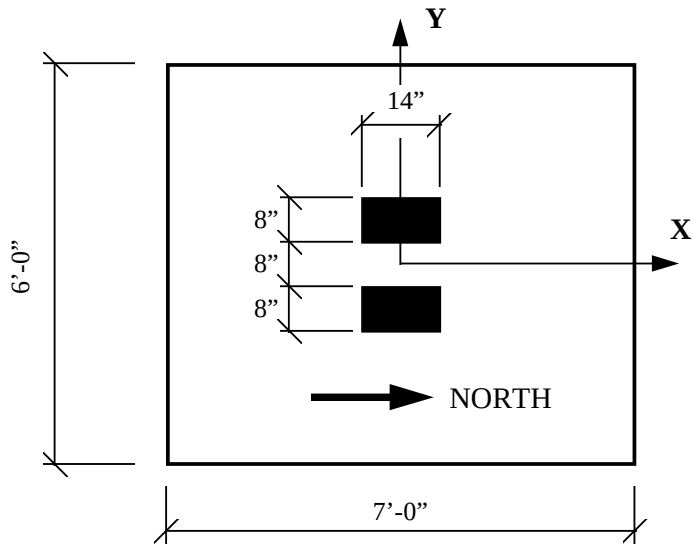

Figure 5.11: Loading footprint used for cast-in-place pulsating fatigue test specimens.

As previously mentioned, calculations indicated that punching shear capacity exceeded flexural capacity for PCP test specimens. As a result, static tests on PCP test specimens were not anticipated[1]. The goal was to test at least one specimen at the greatest possible load range that would not cause flexural failure. The loading footprint for PCP test specimens was reduced from that used in CIP pulsating fatigue test specimens, in order to increase the punching shear stresses without increasing the applied load and thereby risking flexural failure. The loaded area was reduced from the 14-inch by 24-inch (610-mm by 356-mm) area used in CIP pulsating fatigue tests to 10 inches by $17^1/_2$ inches (445 mm by 254 mm). The aspect ratio of the loaded area was approximately maintained. This reduced loading footprint was used for all tests on PCP test specimens, and is shown in Figure 5.12.

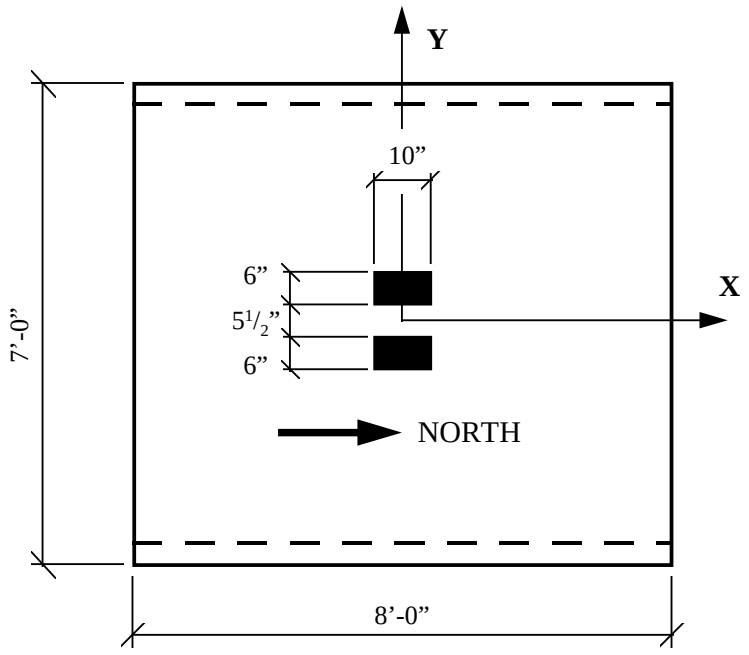

PLAN

NOTE: 1 in. = 25.4 mm

[1] Static tests on precast prestressed panel test specimens, though unanticipated, did occur. This is

Figure 5.12: Reduced loading footprint used for precast prestressed panel test specimens.

5.4 System Control

A closed-loop system, shown schematically in Figure 5.13, was used to control applied loads during tests. An MTS controller monitored the load on specimens through the load cell, compared it with the command signal, and supplied the appropriate corrective signals to the valve driver controlling the flow of fluid through the hydraulic ram. The MTS controller also monitored a mechanical limit switch placed below the test specimens. If the load deviated from the command signal by some pre-set limit, or if deflections exceeded the limit established by the switch, the controller was programmed to stop the test by removing pressure from the hydraulic ram. These limits, as well as the command signal, required occasional adjustment during each test in order to maintain the smooth and continuous application of load cycles. Sinusoidal loading was used, at frequencies between 1 Hz and 4.5 Hz. These frequencies depended on the rate of fluid flow required for each cycle of load, and on the test specimens' frequency response.

---

discussed in Chapter 7.

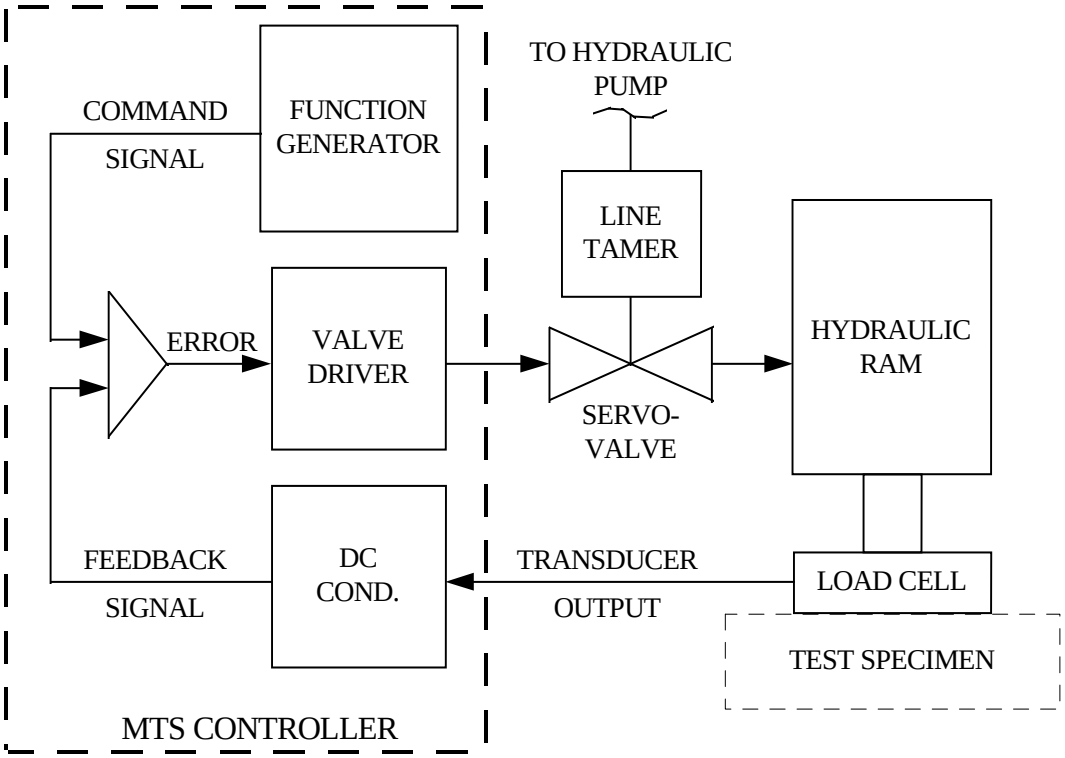

Figure 5.13: Schematic representation of the closed-loop control system used for static and pulsating fatigue tests.

5.5 Data Acquisition and Reduction

During fatigue testing, measurements of strain, load and deflections were recorded on the initial cycle of load, and at regular intervals thereafter. These measurements were recorded at each 5-kip (22.3-kN) load increment through a complete load cycle (starting at and returning to zero load). These data acquisition cycles were performed after cycle numbers 1, 100, 1,000, 10,000, 100,000, and at every 500,000 cycles thereafter until specimens failed. The

progress of fatigue deterioration and crack propagation was documented during each of these data acquisition cycles.

Voltages reflecting measurements of strain, deflections, and load were translated by a Hewlett-Packard Analog-to-Digital Converter (scanner) and recorded using a microcomputer. DC voltage sources were used to provide excitation voltages for strain gages and linear potentiometers. The MTS controller supplied excitation voltage to the load cell, and the load cell's return signal to the scanner. Digital information was converted to engineering units by a microcomputer program, and manipulated using spreadsheet programs.

CHAPTER SIX
TYPICAL TEST RESULTS FOR CAST-IN-PLACE TEST SPECIMENS

6.1 Introduction

This chapter presents typical test results obtained from both static and pulsating fatigue tests performed on cast-in-place (CIP) test specimens. Typical cracking patterns, deflections, and stresses are included as well as a discussion of the fatigue deterioration observed during pulsating tests. Only typical results for CIP test specimens are presented in this chapter. Typical test results for precast prestressed panel (PCP) test specimens are presented in Chapter 7. A discussion of the observed failure modes for CIP and PCP test specimens is included in Chapter 8. The S-N data for both CIP and PCP test specimens are included in Chapter 9.

6.2 Typical Static Test Results for Cast-in-Place Test Specimens

Previous reports for this project presented static test results for CIP test specimens in detail (Whitt 1993, Kim 1994). The following is a brief summary of those results.

Two static tests were performed on CIP test specimens; both resulted in punching shear failures. Failure loads of 173 kips (770 kN) and 205 kips (912 kN) were reported. Flexural cracking was first observed at a load of about 18 kips (80 kN), and propagated in both directions as the applied load was increased, with wider cracks being observed in the transverse direction. Reinforcing steel stresses measured in static tests were well below yield. All measured reinforcing steel stresses were tensile except in the top transverse bars, which showed only

slight compression. A maximum tensile stress of 33 ksi (227 MPa) at a load level of 150 kips (668 kN) was reported for the second static test. This stress occurred in bottom longitudinal bars. Both specimens failed at a maximum deflection of about 0.5 inches (13 mm).

6.3 Typical Pulsating Fatigue Test Results for Cast-in-Place Test Specimens

As discussed in Chapter 5, fatigue cycling was interrupted at regular intervals to record the progress of fatigue deterioration. At each interval, load on the specimen was removed and crack progression was noted. Then, one complete load cycle was applied to the specimen (starting from zero applied load) in 5-kip (22.3-kN) increments. Applied load, deflections, reinforcing steel strains, and concrete strains were recorded at each load increment.

6.3.1 Cracking in Cast-in-place Pulsating Fatigue Test Specimens

While some new flexural cracks formed as cycles of load accumulated, most flexural cracks formed during the first load cycle. After this cycle, cracks generally propagated upward into the specimen and outward toward supports. Figure 6.1 illustrates the typical pattern of cracking observed on the bottom surface of CIP test specimens after punching shear fatigue failure.

Cracks on the edges of test specimens were the most readily observed during pulsating fatigue tests. Flexural cracks running in the longitudinal (north-south) direction were generally vertical when observed at the edges. Cracks running in the transverse direction generally started vertical, but tilted away from the centerline of the specimens as they progressed toward the top surface. Transverse cracks propagated deeper into the specimens than did longitudinal cracks when viewed at the edges. At about third-points on the long edge,

transverse cracks penetrated the top surface and propagated inward several inches before specimen failure.

After specimen failure, intermittent horizontal cracks were observed along the north and/or south edges and near the corners on the east and west edges of test specimens. Some radial cracks were observed emanating from the loaded area on the top surface after failure. Figures 6.2 and 6.3 illustrate the typical pattern of cracking observed around the perimeter of CIP test specimens after punching shear fatigue failure.

PHOTO

Figure 6.1: Typical pattern of cracking observed on the bottom surface of cast-in-place test specimens after punching shear fatigue failure.

PHOTO

Figure 6.2: Typical cracking pattern observed on north and south edges of cast-in-place test specimens after punching shear fatigue failure.

PHOTO

Figure 6.3: Typical cracking pattern observed on east and west edges of cast-in-place test specimens after punching shear fatigue failure.

6.3.2 Fatigue Deterioration Observed in Cast-in-Place Test Specimens

Deterioration of CIP test specimens was clearly visible as cycling progressed. While the specimens were being cycled, fine sand was observed falling from cracks. Occasionally, a small piece of concrete or aggregate would drop as well. After 1,000 cycles of load there were typically points along cracks that had clearly lost small pieces of aggregate material. The floor and test frame below test specimens became striped with lines of sand which traced out the pattern of cracking. Debris continued to accumulate on the floor and test frame through the duration of cycling. Specimens cycled to 500,000 cycles or more typically had gaping cracks on the bottom surface due in part to the tremendous loss of material that was observed. Figure 6.4 shows some of the debris that accumulated below CIP test Specimen S1P110.

PHOTO

Figure 6.4: Debris that accumulated below CIP test Specimen S1P110 during fatigue testing.

6.3.3 Deflections for Cast-in-Place Pulsating Fatigue Test Specimens

Deflections recorded at each test specimen's east and west edges (just inboard of the support frame) were averaged and subtracted from the deflection recorded at the center, to remove the affects of rigid-body motion and obtain a net center deflection for the test specimen. Load versus net center deflections recorded at each interval were plotted. The resulting family of load-displacement response curves helps illustrate the behavior of test specimens under pulsating fatigue loading. Figure 6.5 shows the family of load-displacement response curves for Specimen S3P110, which failed at 507,287 cycles. The figure typifies load-deflection behavior of CIP test specimens.

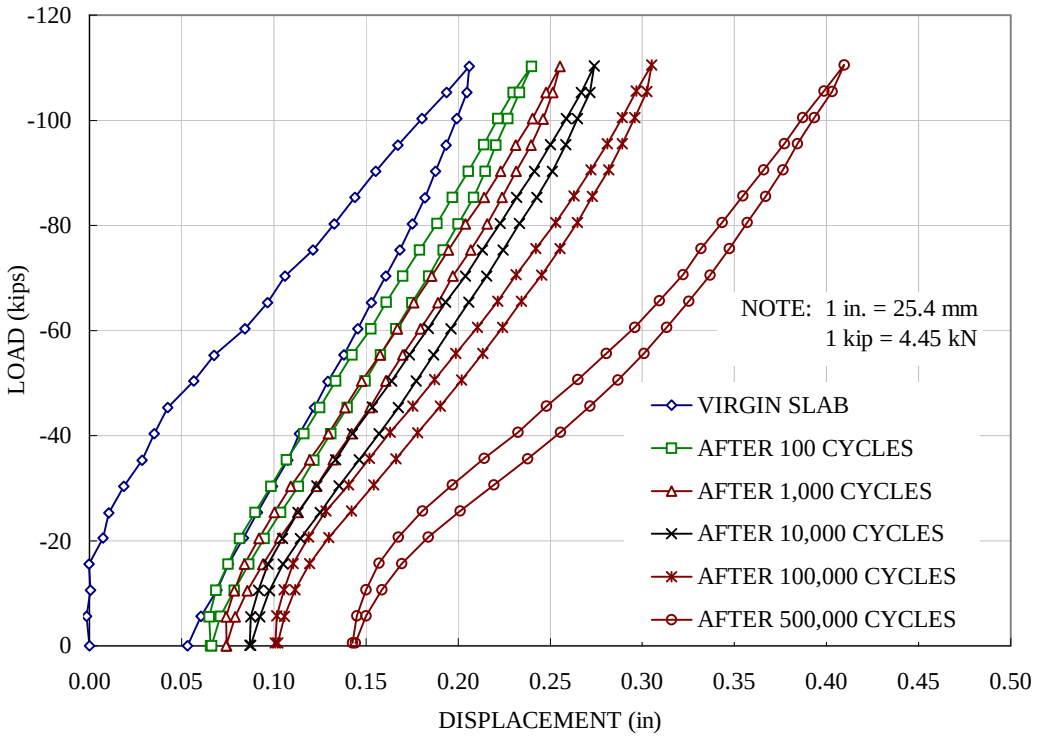

Figure 6.5: Typical load-displacement response for cast-in-place pulsating fatigue test specimens (shown is Specimen S3P110, which failed at 507,287 cycles).

6.3.4 Stresses in Cast-in-place Pulsating Fatigue Test Specimens

Reinforcing steel and concrete strains were recorded at regular intervals during fatigue testing as described above. A few strain gages in every test specimen were damaged before the onset of testing; others were damaged as fatigue cycles accumulated. Measured strains were converted to stresses and plotted. Figure 6.6 is a plot of load versus reinforcing steel stress for Specimen S3P110's initial loading cycle. A specimen plan indicating gage identification numbers is included. Top and bottom bar gages are distinguished by "T" or "B" in Figure 6.6. Placement of gages is shown in Figure 5.8. Stresses which in theory would be equal to one another (due to the symmetric strain gage layout used) were averaged for this illustrative plot. The stresses shown on the figure are a typical representation of the reinforcing steel stresses observed in CIP test specimens. Note that for this particular test specimen, gages B7 and T9 were damaged during concrete placement and were not included in the data.

Figure 6.7 is a plot of load versus concrete stresses for Specimen S3P110's initial loading cycle. Concrete strain gages were placed on the top and bottom surfaces of test specimens at the locations corresponding to gages 5 and 9 shown in Figure 6.6. The transverse measurements were somewhat erratic for this specimen, but are included in the figure. The stresses measured on the bottom surface are shown only up to the load where flexural cracks crossed and broke the surface mounted strain gages. The primary purpose of strain gages on the bottom surface was to measure concrete strains at cracking; this required a crack to form across the strain gages. As load cycles accumulated, reinforcing steel and concrete stresses increased in the same manner as that shown in Figure 6.5 for displacements.

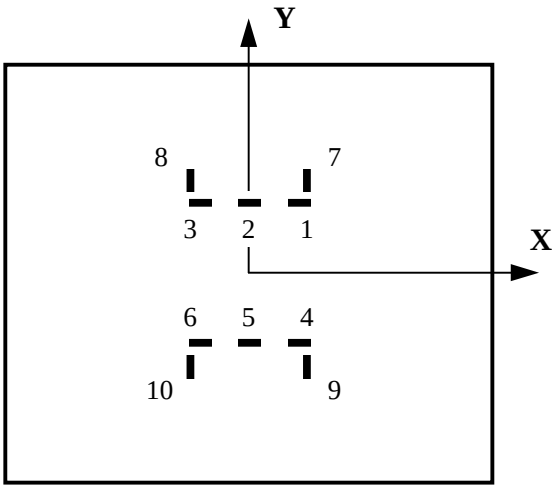
Y
X
8
7
3
2
1
6
5
4
10
9

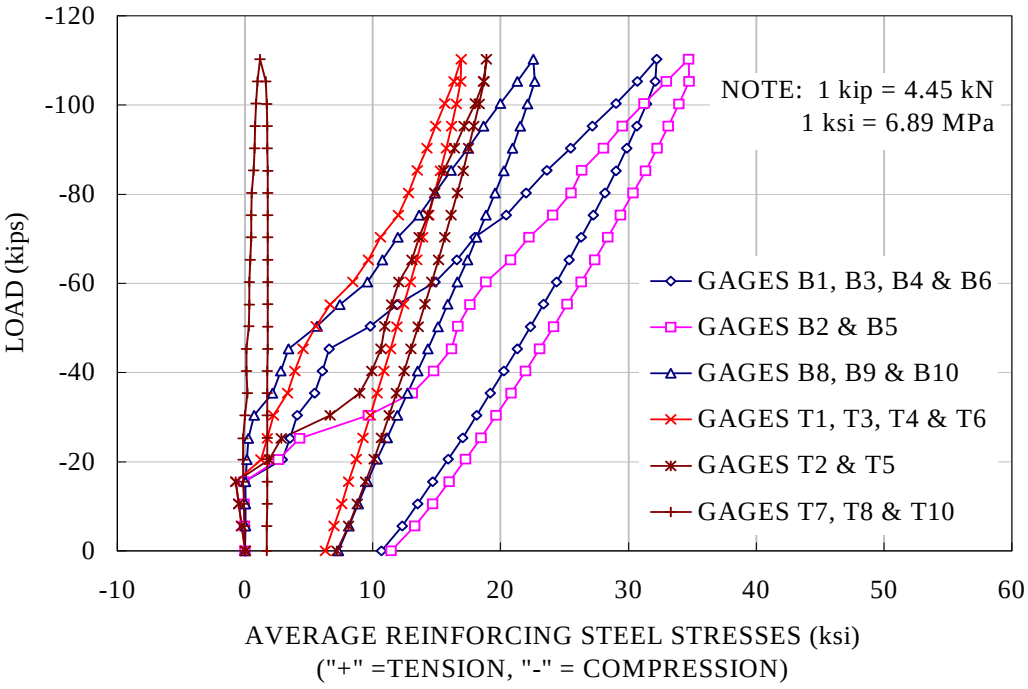
-120
-100
-80
-60
-40
-20
0
LOAD (kips)
-10
0
10
20
30
40
50
60
NOTE: 1 kip = 4.45 kN
1 ksi = 6.89 MPa
GAGES B1, B3, B4 & B6
GAGES B2 & B5
GAGES B8, B9 & B10
GAGES T1, T3, T4 & T6
GAGES T2 & T5
GAGES T7, T8 & T10
AVERAGE REINFORCING STEEL STRESSES (ksi)
("+" =TENSION, "-" = COMPRESSION)

Figure 6.6: Typical reinforcing steel stresses in cast-in-place pulsating fatigue test specimens (shown is the initial loading cycle for Specimen S3P110).

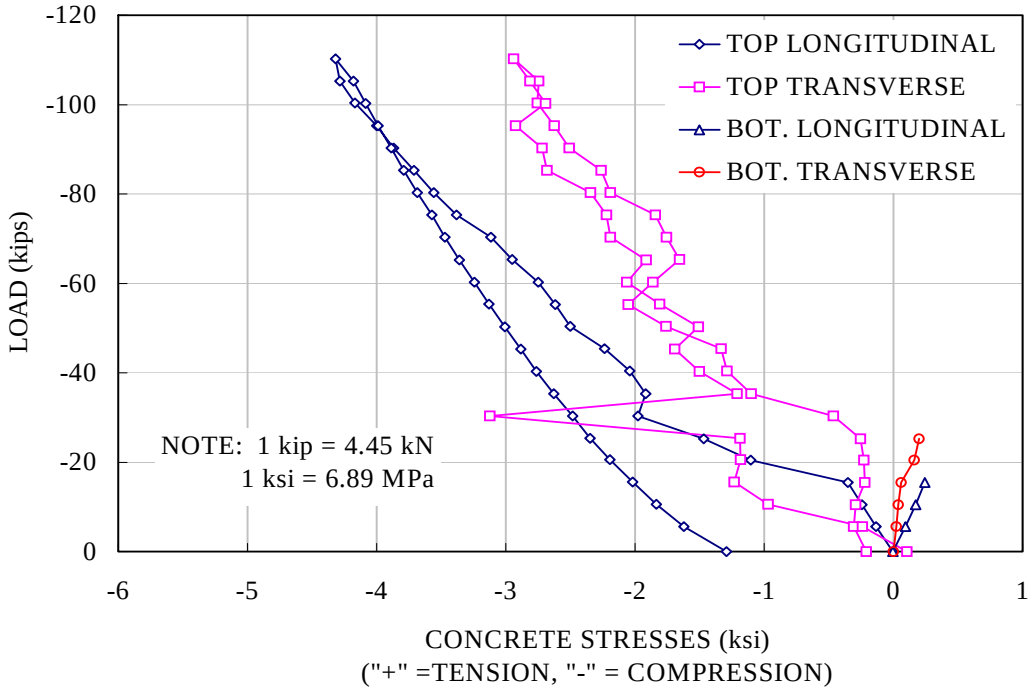

Figure 6.7: Typical concrete stresses in cast-in-place pulsating fatigue test specimens (shown is the initial loading cycle for Specimen S3P110).

CHAPTER SEVEN
TYPICAL TEST RESULTS FOR PRECAST PRESTRESSED PANEL TEST SPECIMENS

7.1 Introduction

This chapter presents typical test results obtained from both static and pulsating fatigue tests performed on precast prestressed panel (PCP) test specimens. Cracking patterns, deflections, and stresses are included as well as a discussion of the deterioration observed during pulsating fatigue tests. Typical test results for cast-in-place (CIP) test specimens were presented in Chapter 6. A discussion of the observed failure modes for CIP and PCP test specimens is included in Chapter 8. Test results, including S-N data, are discussed for both CIP and PCP test specimens in Chapter 9.

7.2 Static Test Results for Precast Prestressed Panel Test Specimens

Calculations discussed in Chapter 3 indicated that the punching shear capacity of the PCP test specimens exceeded their calculated flexural capacity. As a result, static tests on PCP test specimens were not planned. The first planned pulsating fatigue test on PCP test specimens was to involve cycling between a minimum load of 10 kips (44.5 kN) and a maximum load of 110 kips (490 kN). During the initial loading cycle, a punching shear failure occurred suddenly at a load of 105 kips (467 kN). A “post-mortem” inspection was performed on this test specimen in order to explain the unexpected failure. The results of this inspection and a discussion of the failure modes observed in both CIP and PCP test specimens are included in Chapter 8. A second static test was performed on a

PCP test specimen; it resulted in a punching shear failure at a load of 115 kips (512 kN).

7.2.1 Cracking Observed in Precast Prestressed Panel Static Tests

Cracking was first observed on the bottom surface of the first static test specimen in the transverse direction (parallel to strands) at a load of about 35 kips (156 kN). Similar cracking was observed in the second static test, but at a load of about 45 kips (200 kN). Flexural cracks quickly radiated out from the loaded region to the edges as the applied load was increased. Transverse cracks were much wider than longitudinal cracks. Within the middle third of PCP test specimens, cracking in both directions was observed, while outside this region only radial cracks were observed before specimen failure.

Failure planes were observed on the bottom surface of PCP static test specimens after punching shear failure, but only near the transverse supports. Punching shear failure planes were not observed near the longitudinal supports. Some cracks on the top surface were observed radiating out from the loaded region after specimen failure. The second static test specimen had a crack on the top surface that ran around the loaded area, but at some distance from it. Figures 7.1 and 7.2 show the pattern of cracking observed on the bottom and top surfaces of PCP static test specimens.

Cracks on the transverse edges propagated much deeper than those observed on the longitudinal edges. When viewed from the edges, some transverse cracks penetrated the top surface and propagated inward. Longitudinal cracks (crossing prestressed strands) never reached the top surface. Figure 7.3 shows the typical pattern of cracking observed on the north and south edges and Figure 7.4 shows the cracking observed on the east and west edges.

PHOTO

Figure 7.1: Typical pattern of cracking observed on the bottom surface of precast prestressed panel test specimens after static punching shear failure.

PHOTO

Figure 7.2: Cracking observed on the top surface of precast prestressed panel test specimens after static punching shear failure.

PHOTO

Figure 7.3: Cracking observed on the north and south edges of precast prestressed panel test specimens after static punching shear failure.

PHOTO

Figure 7.4: Cracking observed on the east and west edges of precast prestressed panel test specimens after static punching shear failure.

7.2.2 Deflections Observed in Precast Prestressed Panel Static Tests

Deflections recorded at the test specimen's east and west edges (just inboard of the support frame) were averaged and subtracted from the deflection recorded at the center, in order to remove the affects of rigid-body motion and obtain a net center deflection. Because loads were maintained constant at each measured increment ("load control"), the deflection just prior to failure was not recorded. The load versus net center displacement curves for both PCP static tests are shown in Figure 7.5. As discussed above, Static Test #1 had a load at failure of 105 kips (467 kN) and Static Test #2 had a failure load of 115 kips (512 kN).

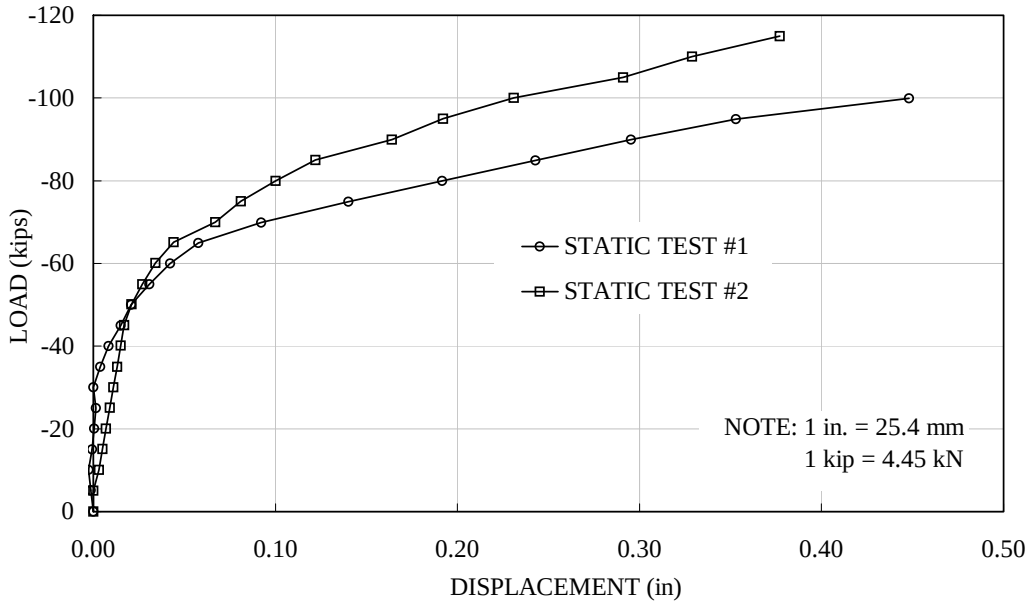

Figure 7.5: Load versus net center displacement curves for PCP static tests.

7.2.3 Stresses Observed in Precast Prestressed Panel Static Tests

The first static test specimen was not instrumented with strain gages. Seven of the 10 strain gage lead wires attached to reinforcing steel in the second static test specimen were accidentally sheared off while installing the specimen into the test setup. Bars in the reinforced concrete topping were very near the neutral axis. Accordingly, the maximum reinforcing steel stress recorded before failure was only about 7 ksi (48 MPa) and was tension in a transverse bar.

Concrete strain gages were attached to the top and bottom surfaces of the test specimen and to the top of the precast prestressed panel before placing the cast-in-place topping. All 6 of these concrete strain gages functioned. Maximum concrete compressive strains recorded were 0.0026 in the longitudinal direction and 0.0014 in the transverse direction.

7.3 Pulsating Fatigue Test Results for Precast Prestressed Panel Test Specimens

Only two pulsating fatigue test were performed on PCP test specimens. The first was PS1P55, which had a load range of from 5 kips to 55 kips (22 kN to 245 kN). The second was PS1P77, which had a load range of from 7 kips to 77 kips (31 kN to 343 kN). As discussed in Chapter 5, fatigue cycling was halted at regular intervals to record the progress of fatigue deterioration. At each interval, load on the specimen was removed and crack progression was noted. Then, a complete load cycle was applied to the specimen (starting from zero applied load) in 5-kip (22.3 kN) increments. Applied load, deflections, reinforcing steel strains, and concrete strains were recorded at each load increment.

7.3.1 Cracking in Precast Prestressed Panel Pulsating Fatigue Test Specimens

Many of the flexural cracks were present after the first load cycle, especially in the transverse direction, and in both directions near the loaded area. However, several new cracks were formed as load cycles accumulated. The cracking patterns observed after punching shear fatigue failure for Specimen PS1P77 were very similar to those shown above for static test specimens. Specimen PS1P55 developed one large transverse crack on the initial load cycle that dominated the overall cracking pattern and behavior for this test specimen. This behavior, as well as the failure mode that was observed is discussed in detail in Chapters 8 and 9. The cracking pattern that developed in Specimen PS1P55 was also very similar to that shown above for static tests.

7.3.2 Fatigue Deterioration Observed in PCP Pulsating Fatigue Test Specimens

Fatigue deterioration in PCP test specimens was evidenced in several ways. As with CIP test specimens, debris was observed raining down from cracks as load cycles accumulated. Specimen PS1P55 had very large pieces of concrete drop from the large transverse crack mentioned above. After specimen failure, it was determined that welded wire fabric crossing this crack had fractured. Figure 7.6 shows some of the debris that accumulated on the test frame below the large crack discussed. A portion of this crack is visible in the photograph.

Partial separation of cast-in-place topping and wearing of the interface was observed in Specimen PS1P77. This was evidenced by the accumulation of fine sand along the top of the specimen support frame at the north end.

PHOTO

Figure 7.6: Some of the debris that accumulated below Specimen PS1P55 during fatigue testing.

7.3.3 Deflections for Precast Prestressed Panel Pulsating Fatigue Test Specimens

Net center deflections were calculated in the same manner as that described above for static tests. Load versus net center deflections recorded at each data acquisition cycle were plotted. Figures 7.7 and 7.8 are the load versus displacement response curves for PCP Specimens PS1P77 and PS1P55 respectively.

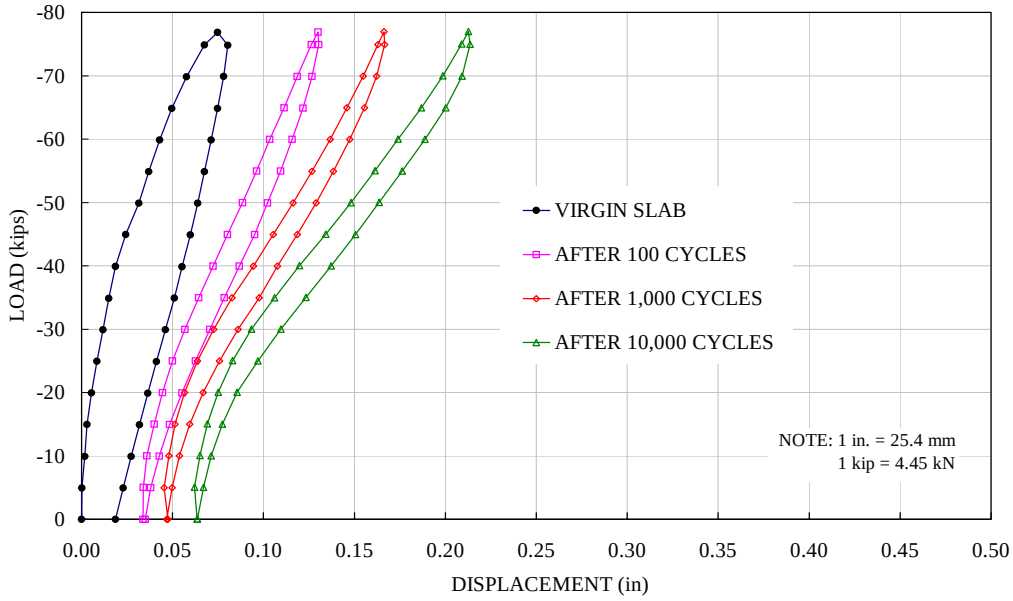

Figure 7.7: Load-displacement response for precast prestressed panel pulsating fatigue Specimen PS1P77, which failed at 56,169 cycles.

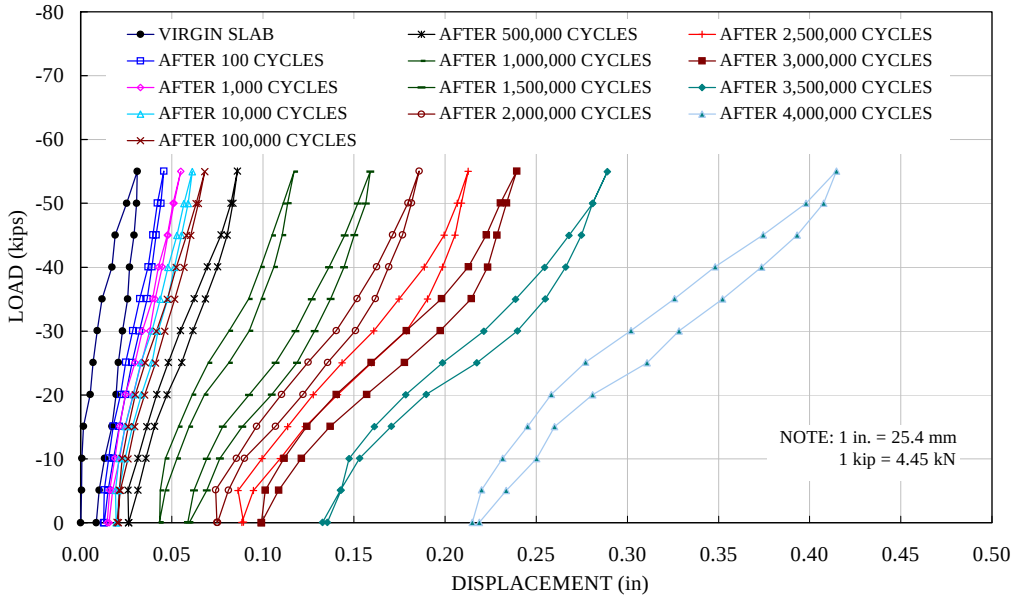

Figure 7.8: Load-displacement response for precast prestressed panel pulsating fatigue Specimen PS1P55, which failed at 4,043,222 cycles.

7.3.4 Stresses in Precast Prestressed Panel Pulsating Fatigue Test Specimens

Reinforcing steel and concrete strains were recorded at regular intervals during fatigue testing as described above. Specimen PS1P77 had a maximum reinforcing steel stress, measured after 10,000 cycles of load, of about 36 ksi (250 MPa) in the longitudinal direction and about 26 ksi (180 MPa) in the transverse direction. Specimen PS1P55 had a maximum reinforcing steel stress of 44 ksi (305 MPa), measured after 3,000,000 cycles in the longitudinal direction (the gage failed before 3,500,000 cycles), and about 36 ksi (250 MPa) in the transverse direction after 4,000,000 cycles.

On the initial load cycle, maximum concrete compressive strains were measured in the longitudinal direction for both specimens PS1P77 and PS1P55. After 10,000 load cycles, compressive strains of 0.00181 in the longitudinal direction and 0.00098 in the transverse direction were recorded for PS1P77. Compressive strains of 0.00257 in the longitudinal direction and 0.00116 in the transverse direction were recorded after 4,000,000 cycles on specimen PS1P55. These top surface strains were recorded between load pads at the center of test specimens. Strains are reported here in lieu of stresses because clearly, a linear stress-strain relationship is not valid for such large compressive strains.

CHAPTER EIGHT
FAILURE MODES AND LOADS

8.1 Introduction

As discussed in Chapter 7 and elsewhere in this thesis, precast prestressed panel (PCP) test specimens experienced static punching shear failures at lower loads than expected. A "post-mortem" analysis was undertaken to help explain the unexpected punching shear failures in PCP test specimens, and to confirm the punching shear failure mode assumed for cast-in-place (CIP) test specimens. A discussion of the failure modes suggested by the post-mortem analysis and by observations made during testing for both CIP and PCP test specimens is included in this chapter. Nominal punching shear stresses for PCP test specimens were adjusted based on observations made during fatigue testing and after the "post-mortem" analysis. These adjustments are also discussed in this chapter. Finally, the experimental test results are compared with results from the analytical models discussed in Chapter 3.

8.2 Post-Mortem Analysis

Seven 2-inch (51-mm) diameter and one 4-inch (102-mm) diameter concrete cores were removed (in pieces) from the first PCP static test specimen. Two of these cores were tested in a universal testing machine. These tests confirmed that the strength of the cast-in-place topping was comparable to the strengths indicated by concrete cylinders cast with concrete topping.

A portion of the partially truncated concrete cone that formed in the first PCP static test specimen was chipped away in order to reveal a portion of the failure plane and to expose panel reinforcement. The size and location of the

welded wire mesh used as reinforcement perpendicular to prestressing strands was determined from this effort. The yield strength of this reinforcement was determined from tests on wires cut from this exposed area. The location, size, and strength of non-prestressed reinforcement used in the precast panels gained in this effort were used in the analytical models discussed in Chapter 3. Figure 8.1 shows the area of concrete removed. Panel reinforcement and flexural cracking are also shown in the figure. Note that strand locations were marked on the panel, and that transverse flexural cracking near the middle of the panel corresponds roughly with those strand locations.

PHOTO

Figure 8.1: Bottom of precast prestressed panel Static Test Specimen #1 showing a portion of the punching shear failure plane and panel reinforcement.

A concrete saw was used to cut open two CIP and two PCP test specimens. For each type of test specimen, one from a static test and one from a pulsating fatigue test were saw cut. The saw had a maximum effective cutting depth of about $3^1/_4$ inches (8.3 mm). After sawing from both sides, pieces were separated by breaking the uncut concrete at mid-depth. The PCP specimens were saw cut in half and then one of these halves was cut into two quadrants. Due to the location of longitudinal reinforcement in CIP test specimens (about mid-depth of the section), saw cuts in the transverse direction would not allow the two halves to be separated. For this reason, CIP test specimens were only saw cut down the longitudinal axis.

The failure planes and cracking patterns revealed in CIP test specimens were surprising, and are discussed in the following section of this thesis. Information gained from sawcut PCP specimens helped confirm their assumed failure modes. Failure modes for PCP test specimens are discussed in Section 8.4 of this thesis. Figures 8.2 through 8.8 are photographs of the saw cut test specimen faces. Hydrostone (gypsum paste) was used to provide a smooth surface for the concrete saw to roll over and to highlight the failure plane surfaces as much as possible. The hydrostone is visible in the figures. Cracks were marked after saw cutting.

PHOTO

Figure 8.2: Saw cut face (longitudinal section) of a cast-in-place static test specimen.

PHOTO

Figure 8.3: Saw cut face (longitudinal section) of cast-in-place pulsating fatigue test Specimen S3P110 (north half).

PHOTO

Figure 8.4: Saw cut face (longitudinal section) of cast-in-place pulsating fatigue test Specimen S3P110 (south half).

PHOTO

Figure 8.5: Saw cut face (longitudinal section) of a precast prestressed panel static test specimen.

PHOTO

Figure 8.6: Saw cut face (transverse section) of a precast prestressed panel static test specimen.

PHOTO

Figure 8.7: Saw cut face (longitudinal section) of precast prestressed panel pulsating fatigue test Specimen PS1P77.

PHOTO

Figure 8.8: Saw cut face (transverse section) of precast prestressed panel pulsating fatigue test Specimen PS1P77.

8.3 Observed Failure Modes in Cast-in-Place Test Specimens

The longitudinal section of the CIP static test specimen shown in Figure 8.2 indicates a punching shear failure mode. Several diagonal cracks sloping down and away from the loaded area are evident in the figure. Note that in addition to the typical punching shear failure planes, a crack begins at the south (left) edge of the loaded area and runs just below the top surface about 18 inches (457 mm) towards the south end of the test specimen. The damage on the bottom near the south end of the specimen occurred when separating the two saw cut halves, and is unrelated to the behavior under testing.

The failure planes and cracking patterns for the CIP pulsating fatigue test specimens are shown in Figures 8.3 and 8.4. Although the load footprint punched through the top surface as occurs in a punching shear failure, a typical punching shear failure did not occur in this test specimen. Note that the failure planes shown in those figures do not slope down and away from the loaded area, but rather run away from the loaded area just below the top surface. This failure

plane extends all the way to the north (left) end of the specimen before it dips down over the last transverse bar (and horizontal hooks in longitudinal bars) and exits at about mid-depth of the section (Figure 8.3). At the opposite end, this crack stops about 6 inches (152 mm) from the panel's edge (Figure 8.4).

The location where this failure plane intersects the edge was denoted by the presence of an intermittent horizontal crack on the north end. This type of cracking was observed, to some extent, on all CIP pulsating fatigue test specimens as discussed in Chapter 6 and illustrated in Figure 6.2. This, and the fact that obvious failure planes were not observed on bottom surfaces of CIP pulsating fatigue test specimens leads to the conclusion that the failure mode exhibited in Figures 8.3 and 8.4 occurred in all pulsating fatigue test specimens.

8.3.1 Discussion of Failure Mode Observed in Cast-in-Place Pulsating Fatigue Test Specimens

Very high compressive stresses developed around the loaded area on the CIP test specimens. These compressive stresses were the result of flexure combined with arching action and increased in magnitude as load cycles accumulated. These compressive stresses were maintained in equilibrium by horizontal shearing stresses, which were greatest in magnitude at the neutral axis location. Results from the finite element analysis of the CIP test specimens indicated these horizontal shearing stresses to be very large near the perimeter of the loaded area. As discussed in Chapter 4 and illustrated in Figures 4.7 and 4.8, maximum horizontal shear stresses observed in the finite element model were about 0.70 ksi (4.8 MPa) in the transverse direction and 0.47 ksi (3.2 MPa) in the longitudinal direction.

Section 11.1.2 of the ACI Code limits values of $\sqrt{f'_c}$ used in shear capacity equations to 0.10 ksi (0.69 MPa) except for special circumstances. As

stated in the Commentary to that Code, this limit is imposed due to the limited amount of test data available for high strength concrete structures. This limit is mentioned here as a means to illustrate the magnitude of horizontal shear stresses predicted by the finite element model.

While the amount of transverse reinforcement provided was not sufficient to cause crushing of concrete due to flexure alone, the presence of even minimal membrane compression in the transverse direction would cause crushing failures to occur. Examination of the moment-axial force interaction diagrams shown in Figures 3.5 and 3.6 for M_{XX} moments illustrates this point. Note that for membrane compressive forces above the balance point (about 9 kips/ft, or 131 kN/m), a crushing failure would be expected in the transverse direction.

It is hypothesized that small regions in CIP pulsating fatigue test specimens experienced horizontal shear failures near the perimeter of the loaded area, as can be seen in Figure 8.2 for the static test specimen. These regions of delamination are believed to have propagated horizontally as load cycles accumulated. It is believed that failure occurred when this horizontal plane reached the outside edge of the CIP pulsating fatigue test specimens. At this instant, compressive forces would be resisted by the concrete below the plane of delamination. The section would then experience a tremendous loss of flexural capacity due to the decreased arm between compressive and tensile forces, and would have manifested this by a large increase in deflection and possible crushing of concrete. The result would be the appearance of a punching shear failure as the load punched through the delaminated plane surrounding the loaded area. Because this phenomenon was not anticipated or discovered until after the completion of testing, this hypothesized failure mode was not confirmed during pulsating fatigue tests.

8.4 Observed Failure Modes in Precast Prestressed Panel Test Specimens

Static test specimens had punching shear failures at loads much lower than predicted by the general punching shear equation discussed in Chapter 3. Observations made during both static and pulsating fatigue tests, and discussed in Chapter 7 of this thesis, suggest that a combination of failure modes occurred. Flexural hinging parallel to the transverse axis (parallel to prestressing strands) were observed, combined with punching shear failures along sloping planes parallel to the longitudinal axis. The "post-mortem" inspection also revealed regions where precast panels had separated from cast-in-place topping. A simple representation of this combined failure mode for PCP test specimens is illustrated in Figure 8.9.

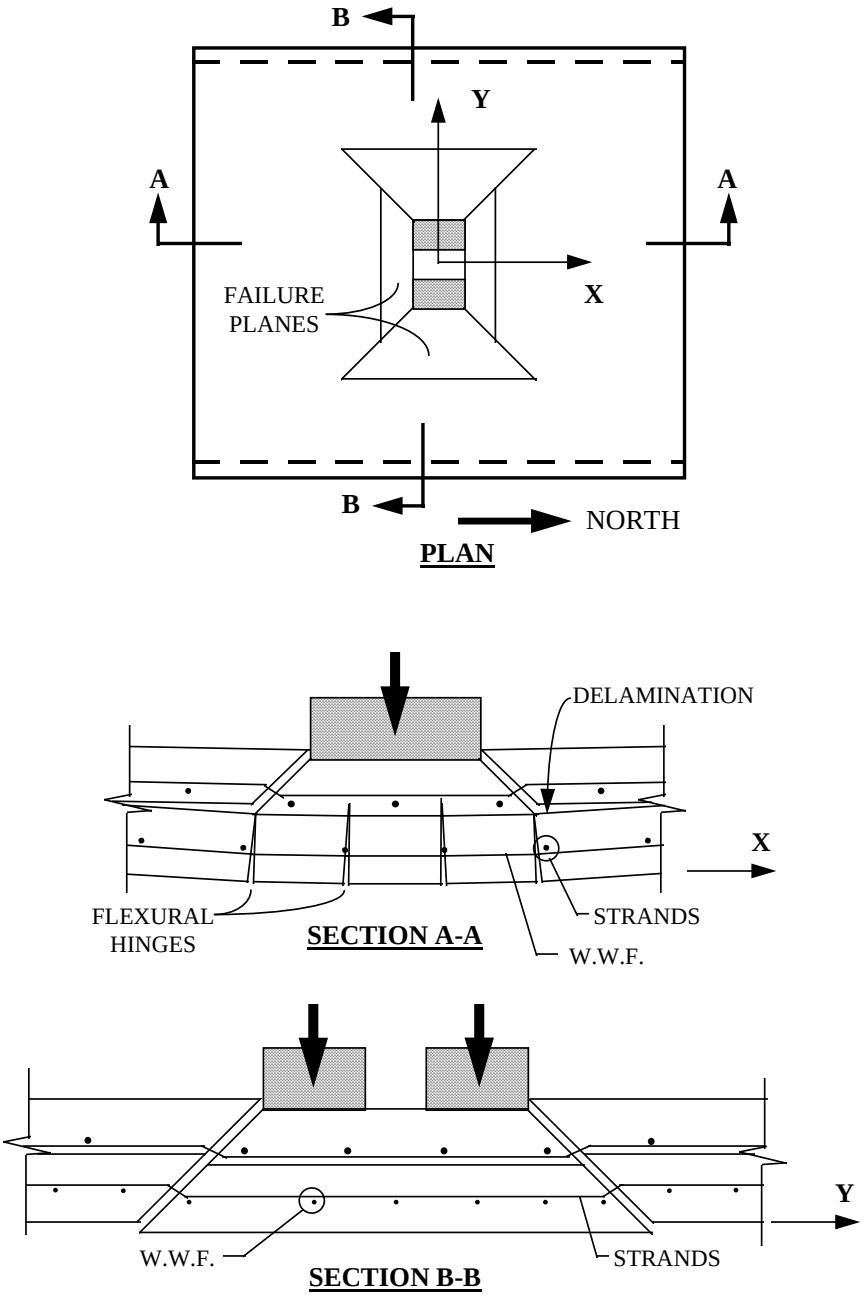

Figure 8.9: Combined failure mode observed in static tests on PCP test specimens.

Similar but more complicated behaviors were observed in PCP pulsating fatigue test specimens. The flexural hinging observed and described above for static test specimens was also observed in PCP pulsating fatigue test specimens. However, Specimen PS1P55 experienced so much deterioration along this hinge line that the welded wire mesh panel reinforcement fractured where it crossed the tremendous crack that developed during fatigue cycling. This crack developed along the south edge of the loaded area, and a punching shear failure was observed only to the north of this crack. Pulsating fatigue test Specimen PS1P77 had a failure mode very similar to that observed in static tests on PCP test specimens.

Both saw cut PCP specimens clearly showed that precast prestressed panels separated to some extent from the cast-in-place topping. As discussed in Chapter 7, this delamination was observed during fatigue cycling only at the north edge of Specimen PS1P77. The delaminations observed in the PCP specimens are believed to have been a secondary effect of the combined failure mode caused primarily by compatibility between transverse and longitudinal deformations, and horizontal beam shear at the moment of failure.

While compatibility of deformations and horizontal beam shear were believed to be the primary causes of the delaminations observed in the PCP specimens, a third factor possibly contributed as well. In the longitudinal section A-A of Figure 8.9, topping reinforcement that is in flexural tension produces a slight upward force due to catenary action in the deflected shape. This results in some direct tension across the panel/topping interface; this was believed to have contributed to the delaminations observed in the PCP test specimens. Obviously, topping reinforcement passing through the punched-out truncated cone does not contribute to this tension. In the longitudinal direction (which “folded”), this vertical force would have been concentrated near the fold lines. The parabolic

deflected shape observed in the transverse direction would have produced a more distributed vertical force component. The panel must remain bonded to the topping around the perimeter of test specimens for this catenary action to exist. As mentioned above, this bond was not maintained at the north end of Specimen PS1P77.

8.4.1 Influence of Support Conditions on Failure Modes Observed in PCP Specimens

The flexural hinging observed in PCP test specimens resulted from the support conditions used in tests. Simple supports were used on all four edges of test specimens, as discussed in Chapter 5. Precast prestressed panels, and bridge decks in general, are designed to transmit forces to supporting girders primarily in one-way action. Two-way action was deliberately imposed on the PCP test specimens in order to increase their flexural capacity by utilizing as much of the reinforcing steel as possible. As a result of the two-way action imposed and the minimal reinforcement provided perpendicular to prestressing strands in standard Texas Department of Transportation (TxDOT) panels, flexural hinging occurred parallel to the transverse axis of PCP test specimens.

Flexural hinging was primarily responsible for the complicated failure modes for PCP test specimens discussed above. Although support conditions used for testing were responsible for the flexural hinging observed in test specimens, similar support conditions are used at end diaframs in bridges constructed in accordance with TxDOT standard details. These details are shown on TxDOT Standard Detail Sheet PCP 1 of 2 for regular end diaframs and on sheet PCP 2 of 2 for skew bridges. Figure 8.10 shows the basic information shown on TxDOT standard detail sheets for this support condition. It seems unlikely that flexural hinging similar to that observed in our test specimens would

occur in a real bridge, because only three sides of a precast prestressed panel would be supported at a regular end diafram. However, cracking very similar to that observed in PCP test specimens was observed in tests conducted at Iowa State University (Abendroth 1991), which to some extent simulated the support condition used at regular end diaframs. Even though similar cracking was observed in the Iowa State University tests, flexural hinging was not reported.

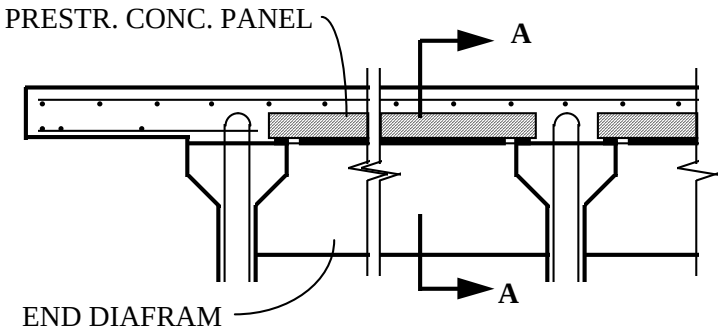

ELEVATION SHOWING REGULAR END DIAFRAM

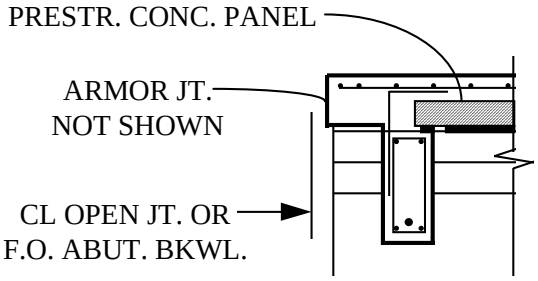

SECTION A-A

Figure 8.10: Typical precast panel support condition used by the Texas Department of Transportation at regular end diaframs in bridges.

8.4.2 Modification of Predicted Punching Shear Capacities to Account for Observed Failure Modes in Precast Prestressed Panel Test Specimens

Predicted punching shear capacities were modified to account for the partial punching shear failures observed in PCP test specimens. This was done by including only the areas that were observed to have experienced punching shear failures in the two punching shear capacity equations discussed in Chapter 3. A plan view of these areas is shown in Figure 8.9 for static test specimens and for pulsating fatigue test Specimen PS1P77. Punching shear capacities for PCP test specimens based on these areas are summarized in Table 8.1, and complete calculations are included in Appendix E. These areas were designated as $(b_0d)_{eff}$, and are included in the table for all test specimens. While only predicted static capacities are included in the table, the effective areas for pulsating fatigue test specimens included in the table were used in the calculation of S-N data, discussed in Chapter 9.

Table 8.1: Summary of punching shear capacities, V_C, for precast prestressed panel test specimens modified to account for observed failure modes.

	AASHTO and ACI Equation		General Model Equation	
SPECIMEN	$(b_0d)_{eff}$ (in^2)	V_C (kips)	$(b_0d)_{eff}$ (in^2)	V_C (kips)
Static	295	81	405	112
PS1P77	295	-	405	-
PS1P55	252	-	342	-

Note: 1 in^2 = 645 mm^2, 1 kip = 4.45 kN

8.5 Comparison of Analytical and Experimental Results

Experimental test results are compared with analytically predicted results in this section. Punching shear capacities, cracking, deflections, reinforcing steel

stresses, and membrane stresses are included. Because test specimens were reinforced to prevent flexural failure, it was impossible to verify the predicted flexural capacities. Furthermore, verification of the increase in flexural capacity due to arching action was beyond the scope of this project.

8.5.1 Comparison of Predicted Punching Shear Capacities

In Figures 8.11 and 8.12, experimental test results are compared with values predicted by the analytical models for design (discussed in Chapter 3) for CIP and PCP test specimens respectively. The predicted punching shear capacities shown in Figure 8.12 for PCP test specimens are adjusted for observed failure modes using the $(b_0d)_{eff}$ values discussed above and shown in Table 8.1.

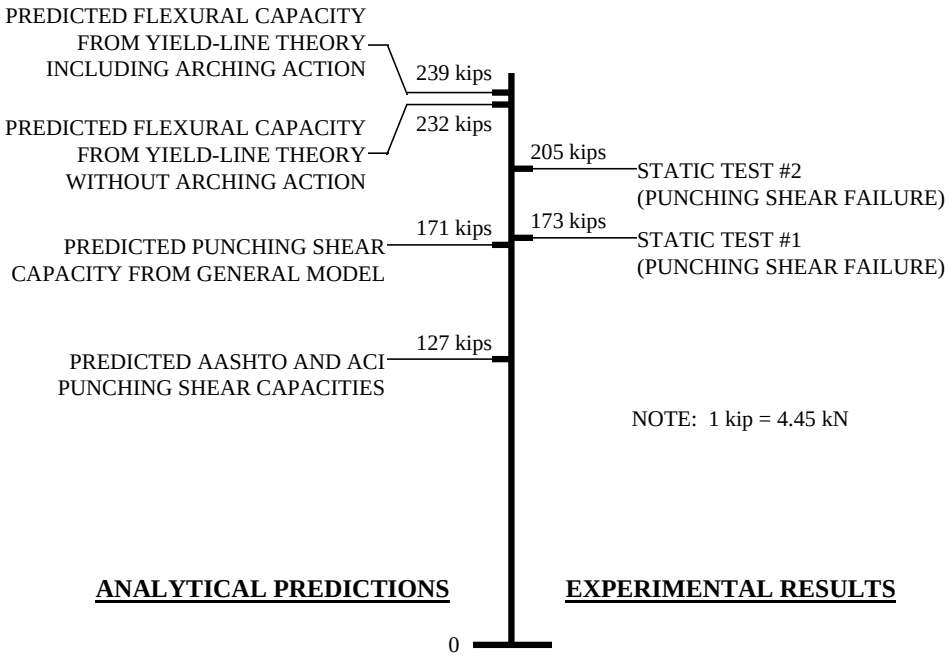

Figure 8.11: Predicted versus observed failure loads for cast-in-place test specimens.

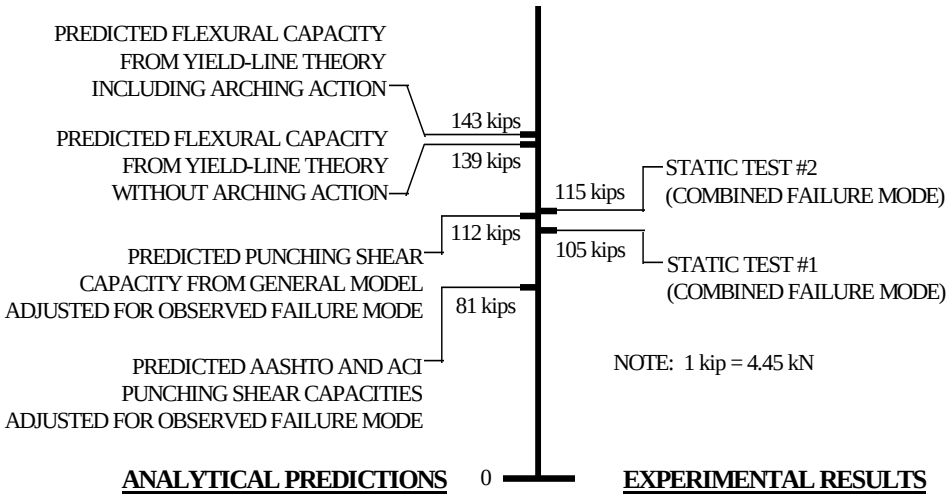

Figure 8.12: Predicted (adjusted for observed failure modes) versus observed failure loads for precast prestressed panel test specimens.

As Figure 8.11 illustrates, experimental punching shear capacities for CIP test specimens averaged 11% higher than that predicted by the general model equation, and nearly 50% higher than that predicted by the AASHTO and ACI equation. Similar relationships were found for PCP test specimens after adjusting the predicted punching shear capacities for observed failure modes. The (adjusted) punching shear capacity predicted by the general model equation is within 2% of the average of experimental punching shear capacities, as illustrated in Figure 8.12. This average was about 36% higher than that predicted by the AASHTO and ACI equations.

8.5.2 Comparison of Cracking

Cracking observed in CIP test specimens was very similar to that predicted by the finite element model discussed in Chapter 4. The radial cracking observed in test specimens could not be predicted by the finite element model because of the orthogonal nature of the cracking criterion used in the analysis. However, the range of cracked elements in the model agreed well with that observed in CIP test

specimens. The depth and horizontal extent of cracking observed in the CIP test specimens was also reasonably consistent with that predicted by the finite element model.

While cracking was not predicted near the outer corner of the finite element model, it was observed in test specimens. This, is again, due to the orthogonal cracking criterion. While stresses in the model parallel to the X and Y axes near this corner were below the cracking stresses, tensile stresses acting on a plane oriented at about 45º to the X and Y axes likely exceeded the cracking stress for this orientation. Examination of these stresses would likely have predicted the cracking that was observed near this outer corner, but this was beyond the scope of the analysis. Examination of these stresses would be automatic in a non-linear analysis. However, as discussed in Chapter 4, a sequential linear analysis was performed so that results could be replicated by TxDOT.

8.5.3 Comparison of Deflections

The center deflection predicted by the finite element analysis was about 0.25 inches (6.4 mm) at 150 kips (668 kN) of load. This is shown in Figure 4.4. This agrees very well with the 0.26-inch (6.6-mm) center deflection that was measured at 150 kips (668 kN) of load during Static Test #2. However, center deflections measured in the initial loading cycle for pulsating fatigue Test Specimens S1P145 through S3P145 were somewhat larger. These deflections, measured at 145 kips of load, were about 0.40 inches (10 mm).

Several factors could have led to the smaller deflection predicted by the finite element analysis. First, the elastic modulus for concrete used in the analysis may not have accurately reflected that of the actual test specimens. This would significantly influence the predicted deflection. Second, the orthogonal cracking criterion of the analysis probably predicted smaller deflections than would have

been predicted by an analysis that considered cracking perpendicular to the direction of principal tension. A third consideration is the flexibility of the support frame used for these tests. As discussed in Chapter 5, the test setup was modified after completion of the tests used for these deflection comparisons. The flexibility of the original test setup, and the interaction between support frame, test specimens, and reaction frame columns may have influenced measured deflections despite efforts taken to remove rigid-body motion from those measurements.

8.5.4 Comparison of Stresses

Reinforcing steel stresses, measured at a load level of 150 kips (668 kN) in Static Test #2, were compared with results from the finite element model. These are shown in Figure 8.13 for transverse reinforcement, and in Figure 8.14 for longitudinal reinforcement. Strain gage locations are shown in Figure 5.8. The predicted stress curves shown in Figures 8.13 and 8.14 are for the stresses along gaged bars.

The average stress measured in bottom transverse reinforcement was 22 ksi (152 MPa), which is about 23% greater than the 18-ksi (124-MPa) stress predicted by the finite element analysis. The measured top transverse bar stress was about 2 ksi (14 MPa), which is very close to the 3-ksi (21-MPa) compressive stress predicted by the finite element analysis. All longitudinal reinforcing steel stresses measured were tensile stresses. A 33-ksi (227-MPa) stress was recorded on a bottom longitudinal bar. This is about 50% greater than the 22-ksi (152-MPa) stress predicted by the finite element analysis. Measured top bar longitudinal stresses were about 9 ksi (62 MPa) and 22 ksi (152 MPa); approximately 5% and 22% greater than the 8.5-ksi (59-MPa) stress predicted.

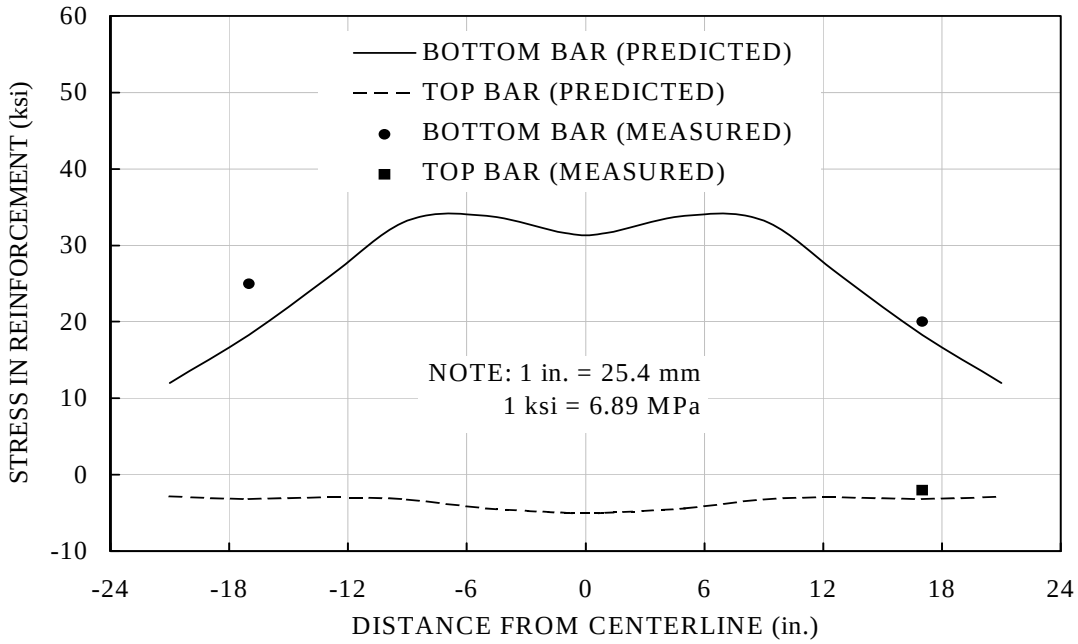

Figure 8.13: Measured and predicted reinforcing steel stresses in transverse bars (tension is positive).

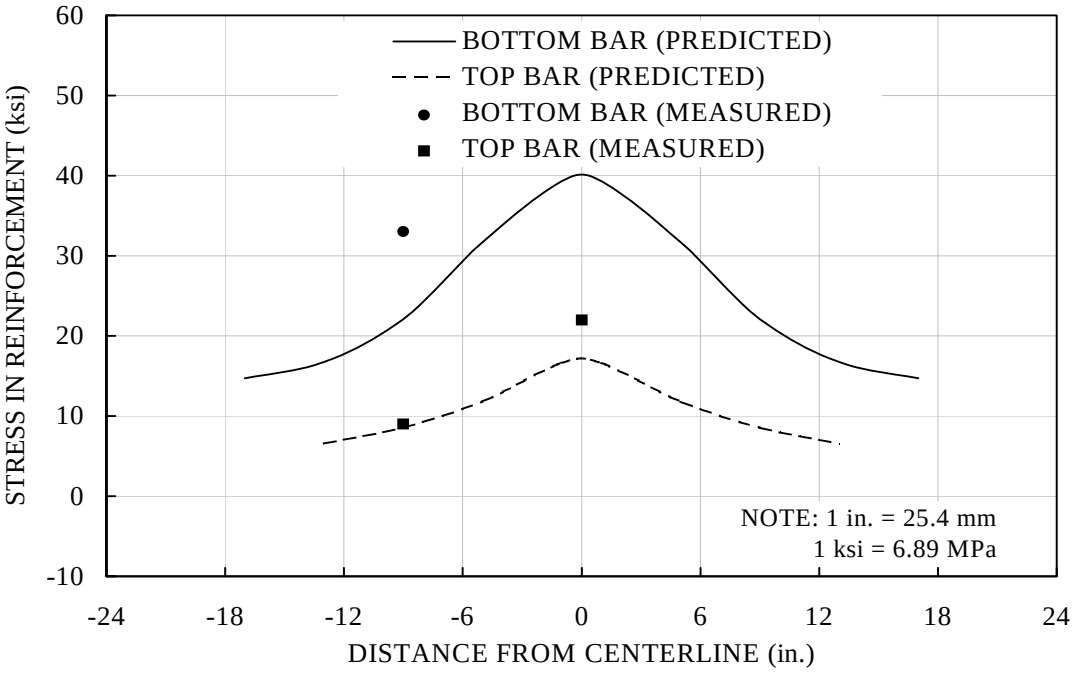

Figure 8.14: Measured and predicted reinforcing steel stresses in longitudinal bars (tension is positive).

8.5.5 Comparison of Membrane Forces

Numerous problems were encountered with strain gage measurements. As discussed in previous reports, none of the concrete strain gages used for the CIP specimen static tests functioned, and only a few of the gages attached to reinforcing steel bars produced reliable results. Similar problems were encountered through the duration of testing. These problems made it impossible to calculate membrane forces in PCP test specimens.

Membrane forces were calculated in both the longitudinal and transverse directions for the initial loading cycle on Specimen S3P110. Reasonable results

were obtained for the longitudinal direction only. This membrane compressive force was 13.2 kips/ft (193 kN/m) at the maximum load applied during the cycle of 110 kips (490 kN). This value is based on a linear relationship between stress and strain. When a non-linear stress-strain relation is considered, this value is increased to about 18.7 kips/ft (273 kN/m). The increase is due to the fact that the initial modulus of the non-linear stress-strain relationship used is greater than that given by the modulus used in the linear relationship. When the increase in actual stress due to Poisson effects are included, the membrane compressive force is increased to about 27.3 k/ft (399 kN/m). These membrane force calculations are included in Appendix C. The value predicted by the finite element analysis at a load of 150 kips (668 kN) was about 7.0 kips/ft (102 kN/m). Assuming linear behavior after the establishment of the final cracking pattern, this would correspond to a predicted membrane force of about 5.1 kips/ft (74 kN/m) in the 110-kip (490-kN) cycle.

CHAPTER NINE
DISCUSSION OF TEST RESULTS

9.1 Presentation of Pulsating Fatigue Test Results Using S-N Curves

Applied loads for all test specimens were plotted against the number of load cycles (N) required to cause failure by punching shear fatigue. The resulting S-N curves were characteristic of typical S-N curves for most engineering materials. When plotted using a logarithmic scale for the horizontal axis (number of cycles to failure), they conformed to a linear relationship between the applied load range (or stress range), and the number of cycles to failure.

9.1.1 Calculation of S-N Data

Nominal punching shear stresses resulting from applied loads were calculated using the relation:

$$v = \frac{P}{b_0 \bar{d}} \tag{9.1}$$

where

v = nominal punching shear stress acting on the failure planes, psi

P = load range used in pulsating tests, lbs.

$b_0 = 2(b_1 + b_2 + 2\bar{d})\bar{d}$ (as defined in Section 3.2.1),

$\bar{d}$ = average effective depth of section (as defined in Section 3.2.1)

These nominal stresses were then normalized to a dimensionless quantity by dividing by $\sqrt{f_c}$, which carries the units of pounds per square inch in punching shear calculations. The value of f_c used was that determined from concrete

cylinders tested on the same day as specimen failure. This nominal stress was calculated for all test specimens, and is summarized in Table 9.1 for the cast-in-place (CIP) test specimens. Also shown in that table is the number of cycles to failure for each specimen. The load range corresponding to static tests (one cycle only) was simply taken as the static failure load.

Table 9.1: S-N data for cast-in-place test specimens.

SPECIMEN	P (kips)	$b_0\bar{d}$ (in^2)	v (psi)	f'_c (psi)	$\frac{v}{\sqrt{f_c}}$	N
Static #1	173	412	420	5,950	5.44	-
Static #2	205	412	498	5,950	6.45	-
S1P145	130	395	329	6,200	4.18	1,443
S2P145	130	395	329	6,200	4.18	29,581
S3P145	130	395	329	6,200	4.18	6,019
S1P110	100	395	253	5,490	3.41	576,454
S2P110	100	395	253	5,710	3.35	697,446
S3P110	100	395	253	5,870	3.30	507,287

Note: 1 in. = 25.4 mm, 1 kip = 4.45 kN, 1 ksi = 6.89 MPa

As noted previously in this thesis, precast prestressed panel (PCP) test specimens did not fail in pure punching shear modes as expected. The observed failure modes were complicated combinations of punching shear, flexural hinging and debonding of the topping slab from the panels. Debonding of prestressing

strands due to flexural cracking parallel to strands was suspected as well, but was not confirmed with certainty. In order to obtain nominal punching shear stresses for PCP test specimens, only those areas that actually appeared to have experienced punching shear failure were included in the above calculations. Discussion of the observed failure modes, as well as the adjustments made to nominal punching shear stresses, was covered in detail in Chapter 8. The S-N data for the PCP test specimens is summarized in Table 9.2. The values of $b_0\bar{d}$ included in the table have been so adjusted to account for observed failure modes; these values were used to calculate the nominal punching shear stresses (v).

Table 9.2: S-N data for precast prestressed panel test specimens.

SPECIMEN	P (kips)	$b_0\bar{d}^*$ (in^2)	v (psi)	f'_c (psi)	$\frac{v}{\sqrt{f_c}}$	N
Static #1	105	295	356	4,770	5.16	-
Static #2	115	295	390	4,720	5.67	-
PS1P77	70	295	237	4,830	3.41	56,169
PS1P55	50	252	198	4,840	2.85	4,043,222

Note: 1 in. = 25.4 mm, 1 kip = 4.45 kN, 1 ksi = 6.89 MPa

* Values were adjusted to account for observed failure modes.

9.1.2 S-N Curves Established From Pulsating Fatigue Test Results

The data presented in Tables 9.1 and 9.2 were analyzed by taking the logarithm of the number of cycles to failure (N), and then performing linear regression analyses on the resulting data sets. The least squares linear regression technique was used to calculate the best-fit line through the data. Figures 9.1 and Figure 9.2 are plots of the S-N data for CIP and PCP test specimens respectively. The best-fit lines are shown in both figures.

A third-least squares linear regression analysis was performed on the combined data set. Figure 9.3 shows all of the S-N data for CIP and PCP test specimens. The best-fit line through the combined data set is shown in the figure.

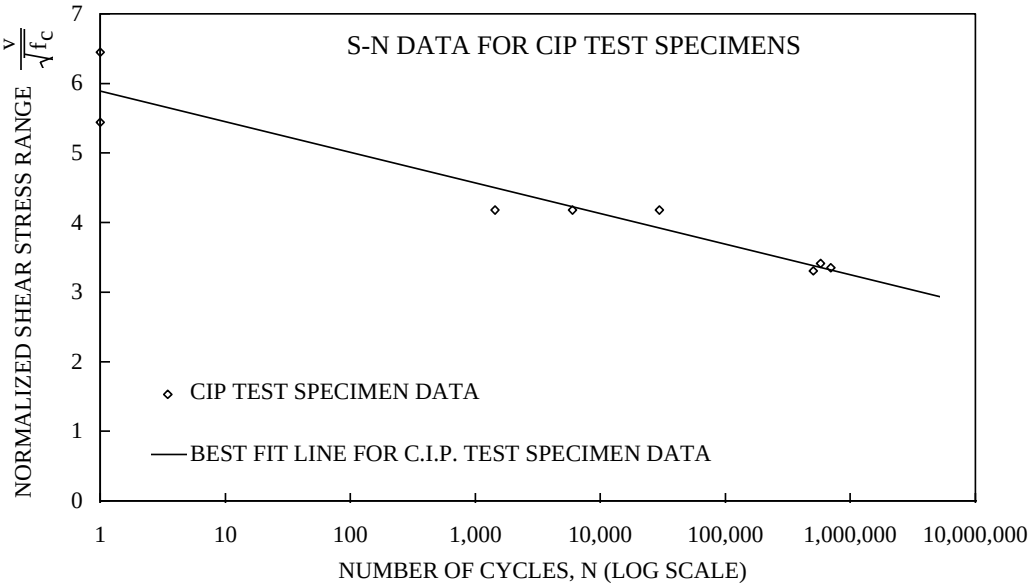

Figure 9.1: S-N curve for cast-in-place test specimens.

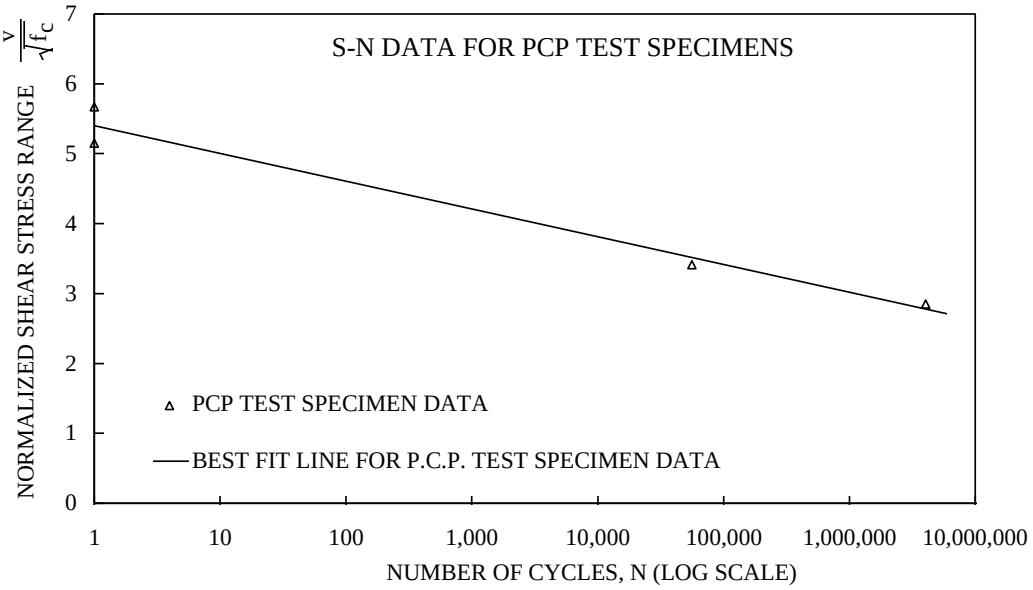

Figure 9.2: S-N curve for precast prestressed panel test specimens.

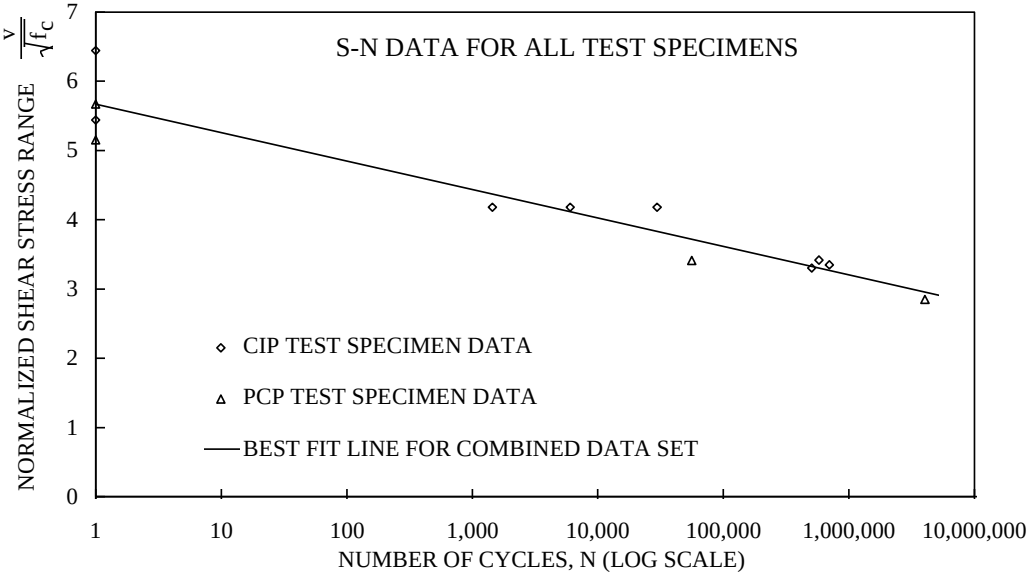

Figure 9.3: Combined S-N data for cast-in-place and precast prestressed panel test specimens.

As was discussed previously in this thesis, the nominal stress ranges for the precast prestressed panel specimens had been adjusted to account for observed failure modes. Uncertainties in the actual failure modes, and therefore in the adjustment calculations made, raise some question as to the validity of combining the respective data sets. However, the limited number of PCP specimens tested, especially under fatigue loading, does not lead to a high degree of confidence in the S-N curve calculated through those data alone. For this reason, and to facilitate a comparison of the data, the data sets were combined as discussed above.

9.2 Comparison of S-N Data for Cast-in-Place Versus Precast Prestressed Panel Specimens

Good correlation was found in the S-N data for CIP and PCP test specimens. Correlation coefficients, commonly referred to as *r* values, were calculated as 0.959 and 0.986 for CIP and PCP test specimens (adjusted for failure modes), respectively. The coefficient for the combined data set was calculated as 0.957. It is interesting to note that the *r* values for the separate data sets were slightly closer to unity (indicating that all data points would lie on a straight line) before normalization and adjustment of the data for observed failure modes.

After adjusting the PCP test specimen results for observed failure modes, the S-N data for CIP and PCP specimens are very similar. The Y-intercept value for CIP test specimens was calculated to be 5.89, less than 10% greater than the 5.40 intercept calculated for PCP specimens. The slopes of the calculated best-fit lines are also very close to one another. The slope of the best-fit line through the CIP data was calculated to be -0.4399 Log(N), while the slope through the PCP data was calculated as -0.3966 Log(N). Because the best-fit line through the PCP

test data is flatter and has a lower Y-intercept value than that for the CIP data, the best-fit lines are farthest apart at their intersection with the Y-axis.

9.3 Comparison of Behavior for Cast-in-Place versus Precast Prestressed Panel Test Specimens

In some aspects of this testing program, CIP and PCP test specimens had very similar behaviors. The complicated failure modes observed in the PCP test specimens made other aspects of behavior difficult to compare. This section compares and contrasts the observed and calculated characteristics of test specimen behavior wherever possible. Cracking, fatigue deterioration, deflections, and stresses are discussed.

9.3.1 Comparison of Cracking Observed in Test Specimens

In general, the typical radial cracking pattern discussed in Chapters 6 and 7 was observed in CIP and PCP test specimens. Both had transverse cracks that were typically wider than those in the longitudinal direction, and that tilted away from the specimen centerlines at the supported edges. However, transverse cracks in PCP test specimens were much wider and less numerous than those in the longitudinal direction. PCP specimens developed a single wide transverse flexural crack (parallel to the strands) on both sides of the loaded area, while CIP specimens exhibited the “alligator scale” cracking noted in (Perdikaris 1988, 1989). Longitudinal cracks in PCP test specimens were typically closer-spaced and more numerous in the vicinity of the load than were those in CIP test specimens.

9.3.2 Comparison of Fatigue Deterioration Observed in Test Specimens

CIP and PCP test specimens experienced similar deterioration due to fatigue cycling. Most flexural cracking occurred at a very small number of load cycles relative to the number of cycles required to cause failure. As loading cycles accumulated, abrasion between crack surfaces seemed to be the primary cause of test specimen deterioration. All pulsating fatigue test specimens lost material due to this abrasive wearing of crack surfaces. As this occurred, flexural cracks propagated upward toward the top surfaces of test specimens.

One major difference in observed cracking was that PCP test specimens developed one large transverse flexural crack on both sides of the loaded area, as described above. These cracks resulted in punching shear and flexural stresses being resisted primarily in the transverse direction, while virtual flexural hinging occurred at these cracks. These cracks deteriorated much more than other cracks in the PCP test specimens.

Test Specimen PS1P55 was cycled at a relatively low load range (5 kips to 55 kips (22 kN to 245 kN)). This specimen experienced so much deterioration along one of these transverse cracks that it practically folded in half. The entire south edge of the specimen began to lift off the support frame with each load cycle. When the edge began to pound the support (at 3 Hz), continuation of the test became questionable. In a matter of minutes this pounding became violent and the specimen suddenly failed at 4,043,222 cycles. Close inspection of the gaping crack which had developed showed that welded wire fabric crossing this crack had fractured. Strongbacks were required to remove the specimen safely from the test frame.

In PCP Test Specimen PS1P77, the topping separated from the panel, and the interface between panel and topping degraded during load cycling. This was evident from the accumulation of fine sand along the north end of the test frame. The source of this sand could only have been the interface between the panel and

the cast-in-place concrete topping. Though areas of delamination were believed to have existed in all PCP test specimens after punching shear failure, Specimen PS1P77 was the only specimen observed to have experienced this phenomenon before failure.

9.3.3 Comparison of Deflections Observed in Test Specimens

In the early stages of cycling, PCP specimens were stiffer than CIP test specimens. Total deflections increased with cycling for all test specimens, as discussed in Chapters 6 and 7. However, maximum deflections due to load (live-load deflection) did not increase as rapidly as did total deflections for either CIP or PCP test specimens. The difference is accounted for in the permanent set (dead-load deflection) due to fatigue deterioration. Figure 9.4 is a plot of total and live load deflections versus number of cycles for Test Specimens S3P110 and PS1P55. Note that a logarithmic scale is used for the number of cycles. Also note that for each specimen, the difference between total deflection and live load deflection represents the permanent set caused by fatigue cycling.

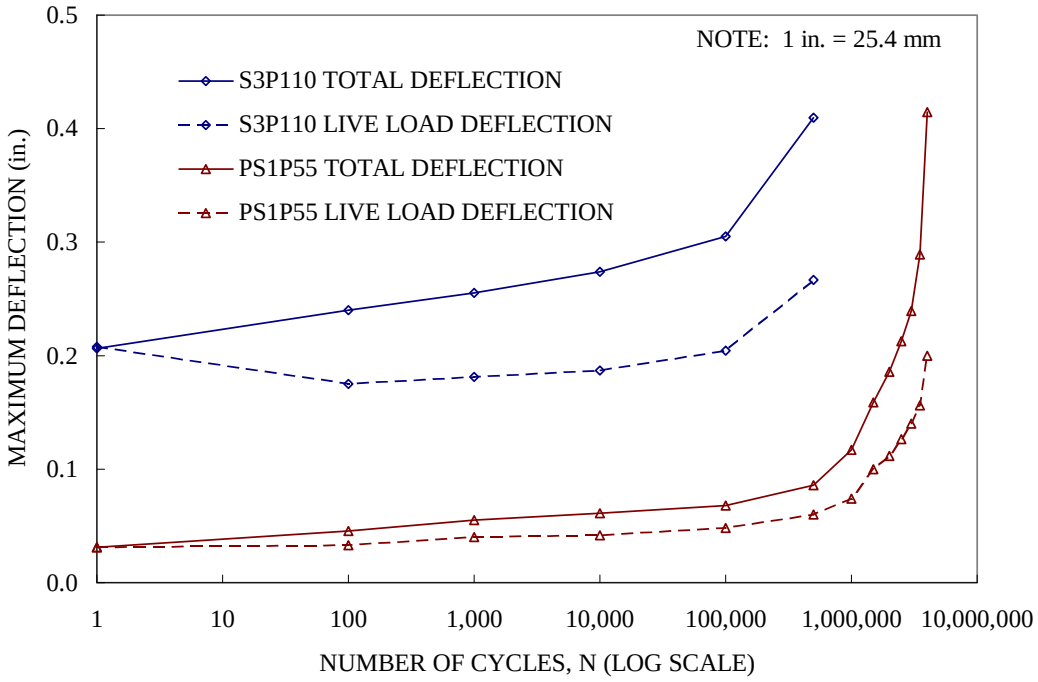

Figure 9.4: Total and live load deflections versus number of cycles for Test Specimens S3P110 and PS1P55.

Figure 9.4 illustrates similarities as well as differences that were observed in the behavior of CIP and PCP test specimens. Most obvious is the difference in relative deflections. As discussed in Chapter 5, the maximum load applied to Specimen S3P110 was twice that applied to Specimen PS1P55; however for ordinates less than 100,000 cycles, the CIP specimen had deflections about 4 times those for the PCP specimen. The figure also clearly illustrates that in contrast to the CIP specimen, the PCP specimen had very little permanent set throughout most of its fatigue life.

9.3.4 Comparison of Stresses Observed in Test Specimens

Measured stresses for CIP and PCP indicated similar trends. Reinforcing steel stresses were larger in the longitudinal direction for both CIP and PCP specimens and increased while cycling. Reinforcing steel stresses remained below yield at all gauged locations. Concrete compressive strains indicated stresses well beyond the elastic limit of approximately $0.5 f'_c$ for concrete as specimens approached the end of their fatigue lives. Longitudinal compressive strains were generally greater than those in the transverse direction for both CIP and PCP specimens.

9.4 Rolling Fatigue

As discussed in Chapter 5, rolling fatigue tests were not completed as part of this research effort. Matsui *et al.* (1986) reported rolling fatigue punching shear test results in detail. The testing program reported in that reference and the conclusions reached by those researchers are summarized in this section.

9.4.1 Other Research

As reported in a previous report on this project (Kim 1994), Matsui *et al.* (1986) developed two rolling fatigue test setups, one for small-scale specimens and another for full-scale specimens. The test setup used for testing full-scale specimens had a running wheel load with a travel of 6.56 feet (2 m). Ten slabs measuring 6.56 feet (2 m) by 9.84 feet (3 m) by 7.48 inches (19 mm) thick were tested. Slabs were simply supported along all four edges and the corners were restrained against uplift by unknown means.

It is not clear from (Matsui 1986) how the size and shape of the loaded area were determined. Furthermore, the data of that reference was normalized by

dividing the applied load by the calculated punching shear failure load due to static loading. Static tests were apparently performed, but the reported results indicate that their Test Series "A" had an observed static failure load of 128 kips (58.0 metric tons), while their Test Series "B" had an observed static failure load of 156 kips (66.2 metric tons). These results are puzzling; Series A would have been expected to have a greater static capacity than the Series B due to its slightly greater depth to the bottom reinforcement. Also, a logarithmic scale was used for their S-N curve's Y axis. Their S-N data indicates a linear relationship between the applied stress range and the number of cycles to failure on this log-log plot. This is inconsistent with the results observed in our tests, which showed a linear relationship on a semi-log plot. Because the loading footprint was not reported, it was impossible to compare the above results directly with data from this research study.

9.4.2 Conclusions of Other Researchers

In spite of the uncertainties associated with the rolling fatigue results reported by Matsui *et al*, some of their conclusions seem justified by their experimental data. They concluded that:

1) The fatigue strength of slabs subjected to rolling loads is only about half that of slabs subjected to fixed pulsating loads of the same magnitude.
2) The main cause for decreased capacity under rolling loads versus fixed pulsating loads seemed to be degradation of crack faces due to alternating repetitions of shear and twisting moments.
3) Crack density and maximum live load deflection were useful indexes for rating fatigue damage to reinforced concrete slabs.
4) Fatigue design using S-N curves obtained from rolling fatigue tests should be introduced into the design of highway bridge decks.

Their first conclusion is somewhat alarming, but stems directly from the S-N curves developed from their rolling fatigue tests. In their report, they state: "From the point of fatigue strength, the present S-N curves [for rolling fatigue] dropped to about half of the ordinary ones [those obtained from fixed, pulsating fatigue tests]. Concerning the fatigue life, the present S-N relations dropped about 10^3 - 10^4 cycles from the ordinary ones." However, their S-N curves indicate that at about 300,000 cycles of load, a specimen subjected to rolling fatigue will fail at an applied stress range of about half of that required to cause failure in a specimen subjected to fixed, pulsating loads. At other N-values, the same relationship between rolling and pulsating fatigue varies approximately linear on their log-log plot. This is illustrated in Figure 9.5 at the end of this Chapter. Their S-N curves do not cover the low-cycle end of behavior (below about 1,000 cycles) and the endurance limit (the stress range below which fatigue failure will not occur) are not addressed in their report.

Their second conclusion stems from a mechanism of deterioration that exists in rolling fatigue tests and in real bridge decks, but not in pulsating fatigue tests -- specifically, the alternating repetitions of movements across a crack. In pulsating fatigue tests, cracks directly under the loaded area simply open and close. In a rolling fatigue test, the opposing faces defining a transverse crack experience shear deformation in one sense as the load approaches. When the rolling load is directly over the crack, the crack opens due to flexure, and the shear deformation across the crack approaches zero. As the rolling load continues past the crack, the opposing faces experience shear deformations in the opposite sense, and of the same magnitude, as when the load first approached. The same is true for twisting moments, M_{XY}. Certainly, the degradation experienced by each

specific crack is greater for a single pass of a rolling load than for a full cycle from a fixed pulsating load.

The third conclusion reached by Matsui *et al*. seems to contradict the observations made during the pulsating fatigue tests of the current research effort. Crack density is defined as the total length of cracks in a unit surface area and, as stated in (Matsui 1986), is a conventional index for rating reinforced concrete slabs in Japan. As stated throughout this thesis, the majority of cracks formed in the very early stages of fatigue cycling. As a result, relatively high crack densities would be reported for test specimens with high remaining fatigue life. This suggests that crack density would be a poor index for rating fatigue deterioration in slabs. It is possible that the development of cracks in rolling tests was in some way different from those in fixed, pulsating tests; however this was not reported in (Matsui 1986).

As discussed in Section 9.3.3 and illustrated in Figure 9.4 of this thesis, live load deflections were nearly constant through most of the fatigue life of the test specimens studied here. As specimens approached fatigue failure, their measured live load deflections did increase, especially in the PCP test specimens. This suggests that in the latter stages of fatigue life, live load deflection would be a useful predictive index of damage. Dead load deflection did increase throughout the entire fatigue life of pulsating fatigue test specimens, and might be a better index than live load deflection for rating slabs through their entire fatigue life.

9.4.3 Correlation Between Pulsating and Rolling Fatigue Tests

Based upon the rolling fatigue tests conducted by Matsui *et al*., and without additional data to contradict or support their conclusions, the rolling fatigue strength of a bridge deck at 300,000 cycles of load would be reduced to half of

that predicted by fixed, pulsating fatigue tests. This relationship is illustrated schematically in Figure 9.5. Note that a logarithmic scale is used for both the X and Y axes in the figure, and that the low-cycle range of values is not included. Although not reported in (Matsui 1986), the S-N curves for rolling and pulsating fatigue loads should originate from the same point (the static failure load) at the zero cycle ordinate.

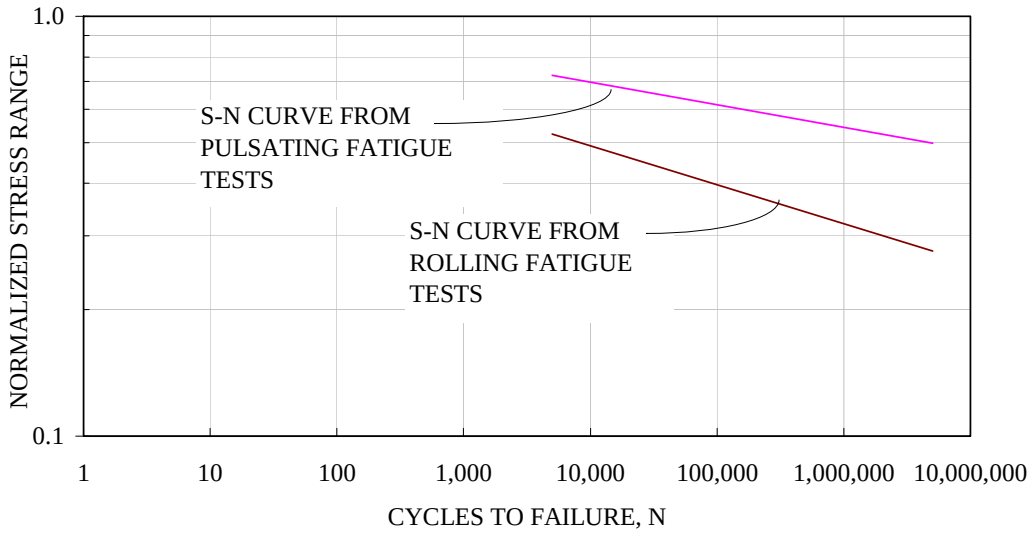

Figure 9.5: Schematic representation of the correlation between pulsating and rolling fatigue test data (after Matsui 1986).

CHAPTER TEN
APPLICATION OF RESULTS TO BRIDGE DECK DESIGN

10.1 Nominal Versus Actual Punching Shear Stress Range

S-N curves were developed from test results, as discussed in Chapter 9, based on nominal punching shear stresses. These nominal stresses are an idealization of the actual stresses that act on the assumed failure planes, and are the basis for the AASHTO and ACI punching shear capacity equation (Eq. 3.1) discussed in Chapter 3. The general punching shear capacity equation (Eq. 3.3) discussed in Chapter 3, also idealizes stresses acting on the assumed failure planes as nominal stresses. The general model equation adjusts the area over which these nominal stresses act, by inclusion of the tan θ term. Angles of 38º (Tsui 1986) and 39º (Whitt 1993, Kim 1994) have been used in the general model equation to predict punching shear capacities with reasonable accuracy. These angles were estimated from observations made after punching shear failures.

The actual stresses acting on the assumed failure planes are quite different from the nominal stresses assumed in design, as was illustrated in Figures 4.11 and 4.12. Those figures were created using results from the finite element analysis of cast-in-place (CIP) test specimens, as was discussed in Chapter 4, and only illustrated stresses acting normal to the assumed failure planes. The actual stresses that act on punching shear failure planes in a bridge deck include: transverse and longitudinal flexural stresses due to bending of the deck; in-plane compressive stresses due to both arching action and composite flexural behavior between the deck and its supporting girders; and shearing stresses.

10.2 Beneficial Affects of Arching Action on Punching Shear Capacity

Arching action increases the punching shear capacity of bridge decks and of slabs simply supported on four edges. Unlike the insignificant increases in flexural capacity for test specimens discussed in Chapter 3, the radial membrane compressive forces (illustrated schematically in Figure 2.1) can significantly increase the punching shear capacity of simply supported test specimens. The difference is that compressive membrane forces radiate through the punching shear failure planes, whereas tensile membrane forces act normal to the test specimens' flexural yield lines.

Some researchers (Batchelor 1978, Kuang 1992) report increases in "punching capacity" with increased percentages of flexural reinforcement. Close scrutiny of their publications reveals that "punching capacity" refers to both flexural capacity and punching shear capacity. Dragosavic (1987) clearly distinguishes between flexural capacity and punching shear capacity. Data included in that publication indicates that no significant increase in punching shear capacity is realized with increasing percentages of flexural reinforcement.

The affect of membrane compression on punching shear capacity is best illustrated by a Mohr's circle diagram. Figure 10.1 shows Mohr's circles for a thickness of slab adjacent to a loaded area. The solid circle in the figure represents the nominal state of stress given by the AASHTO and ACI punching shear capacity equation (Eq. 3.1) at nominal capacity. The dashed circle indicates the influence of membrane compression on this same state of stress. The sloping lines shown in the figure are the orientations of the planes on which principal tensile stresses act. Note in the figure that the orientation of the principal tensile plane (punching shear failure plane) implied by the AASHTO and ACI punching shear capacity equation is oriented at 45º to the plane of the deck.

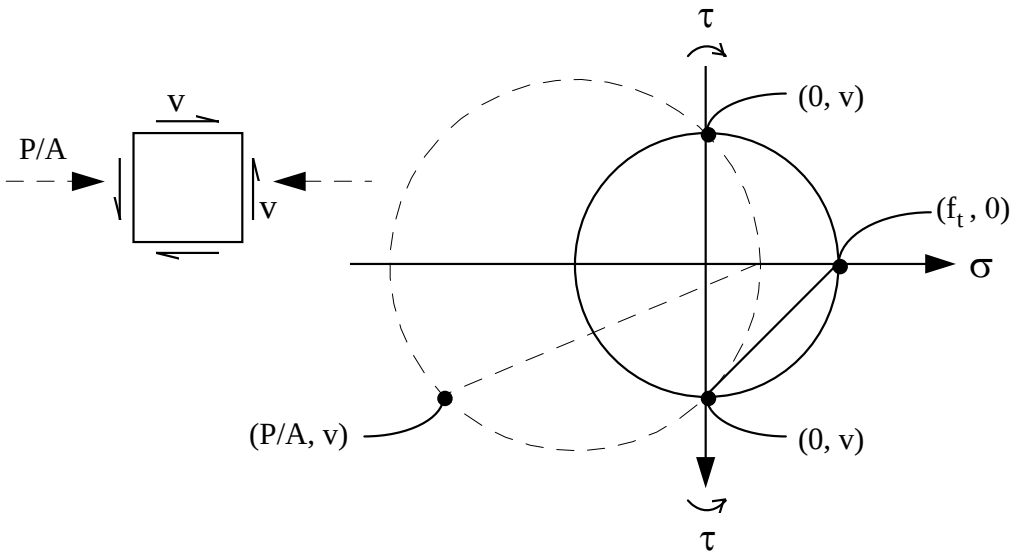

Figure 10.1: Mohr's circles for nominal stresses.

The punching shear capacity equations discussed in Chapter 3, imply that a punching shear failure occurs when the nominal principal tensile stress acting over the area of the failure planes reaches a limiting value. This limiting value is given by the point where the solid circle crosses the σ axis in Figure 10.1, and is simply the ultimate tensile capacity of concrete, f_t, given by (Eq. 3.2). In the presence of membrane compression, the nominal shear stress, v, must be increased (by applying more out-of-plane load) in order for the principal tensile stress to reach this limiting value. This is illustrated in Figure 10.2, which shows the states of stress representing imminent punching shear failure with (shown dashed) and without (shown solid) the presence of membrane compression. The sloping lines shown in the Figure 10.2 are the orientations of the theoretical punching shear failure planes on which the nominal principal tensile stresses act. Note (Figure 10.2) that these stresses must act over a larger area due to the

"flatter" slope of this principal tensile plane. The net result is a higher punching shear capacity in the presence of membrane compression.

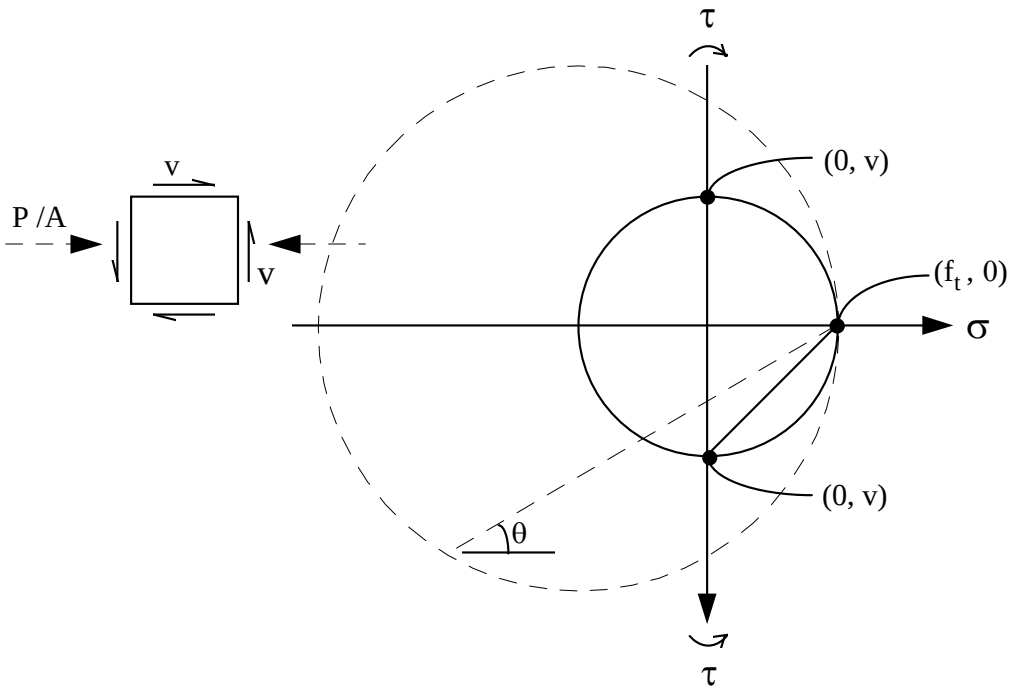

Figure 10.2: Mohr's circles for nominal stresses at nominal punching shear capacity.

10.2.1 Calculation of Punching Shear Capacity Including The Affects of Arching Action

The slope of the punching shear failure planes is accounted for in the general punching shear capacity equation (Eq. 3.3) discussed in Chapter 3. As discussed in that chapter, and above, reasonable agreement between predicted and observed punching shear failure loads was obtained when an angle of 38º or 39º was used in that equation. These angles were based on observations made after

punching shear failures. Using the geometric properties of Mohr's circle, an equation can be derived that expresses the angle of the principal tensile plane (punching shear failure planes) as a function of membrane compression and the ultimate tensile capacity of concrete. This equation can be expressed as:

$$\theta = \frac{1}{2}\text{Cos}^{-1}\left(\frac{P_{memb}}{2\,f_t + P_{memb}}\right) \qquad (10.1)$$

where

θ = acute angle between horizontal and the punching shear failure planes

P_{memb} = the absolute value of membrane compressive stress

f_t = ultimate tensile capacity of concrete (as defined by Eq. 3.2)

(consistent units of stress must be used for P_{memb} and f_t)

As discussed in Chapter 4, average values of transverse membrane compression of about 1.87 kips/ft (27.3 kN/m) at 20 kips (89 kN) of applied wheel load, were predicted by the finite element model of the full bridge. This value agreed reasonably well with the value of approximately 2.08 kips/ft (30.4 kN/m) at 20 kips (89 kN) of applied wheel load measured by (Fang 1986) during tests of a full-scale bridge. If the value for membrane compression is simply taken as 2.0 kips/ft (29 kN/m) at 20 kips of applied wheel load, then a value for membrane stress of 0.0222 ksi (0.153 MPa) for each 20 kips of applied wheel load results for the $7^1/_2$-inch (191-mm) thickness used for CIP test specimens and for the tests conducted by (Fang 1986). At 150 kips (668 kN) of applied load, a compressive membrane stress of about 0.167 ksi (1.15 MPa) is calculated using this value. This agrees very well with the value of compressive membrane stress

predicted by the finite element model for test specimens in the area of the punching shear failure planes (see Figure 4.11).

Using the value of 2.0 kips/ft (29 kN/m) of membrane compression for each 20 kips of applied wheel load given above, and the value for ultimate tensile capacity of concrete, f_t, given by (Eq. 3.2), values of θ can be calculated using (Eq. 10.1). Using this value for θ in the general punching shear capacity equation results in predicted punching shear capacities that agree reasonably well with experimental results. However, this technique requires an initial estimate of the maximum wheel load that can be applied to a bridge deck in order to estimate the compressive membrane stress that will result. The AASHTO and ACI punching shear capacity equation can be used to provide this initial estimate. Because the punching shear capacity predicted by the AASHTO and ACI punching shear equation does not include the beneficial affects of arching action, the capacity predicted by the technique discussed above will be higher than the initial estimate. Therefore the membrane compressive stress will also be higher than the initial estimate, and one or two iterations are required to calculate a punching shear capacity using this technique. This process is illustrated in Appendix F.

The increase in punching shear capacity predicted using the method presented above is significantly influenced by the size and aspect ratio of the loaded area. This is illustrated by Figure 10.3. The quantity α that defines the vertical axis in that figure is the punching shear capacity calculated using the method above, divided by the capacity calculated using the AASHTO and ACI equation (Eq. 3.1). The aspect ratio of the loaded area, β_C, is plotted on the horizontal axis for values between 1 and 4. Figure 10.3 covers a range of parameters well beyond the scope of this research and only illustrates how a loaded area's size and aspect ratio, as predicted by the method above, influences the punching shear capacity of a bridge deck.

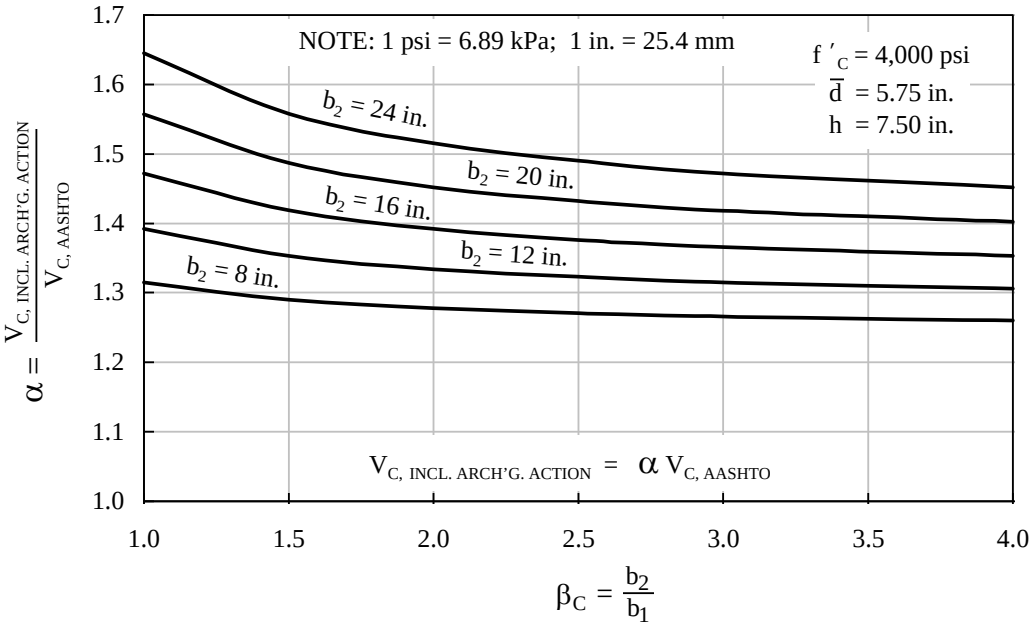

Figure 10.3: Influence of a loaded area's size and aspect ratio on the predicted increase in punching shear capacity due to membrane compression.

It must be repeated here that the nominal punching shear stresses, v, calculated using the AASHTO and ACI punching shear capacity equation are not representative of the actual stresses that act on punching shear failure planes. That punching shear capacity equation is an empirical equation used in most strength design codes in the United States. Although based on principles of mechanics illustrated by the Mohr's circle diagrams above, the equation for θ (Eq. 10.1) was derived from the nominal punching stresses at nominal capacity given by the AASHTO and ACI punching shear capacity equation.

The general punching shear capacity equation and design recommendations presented above are also based on these nominal punching shear stresses. The method presented above calculates punching shear capacities that are reasonably

close to those observed in test specimens from this research project and to those reported by (Fang 1986) for tests on a full-scale bridge. The range of parameters used in testing was limited, and the applicability of design recommendations should also be limited accordingly.

The average effective depth to the bottom mat of reinforcement, $\bar{d}$, and the 4,000-psi (27.6-MPa) concrete compressive strength indicated in Figure 10.3, are representative of a typical isotropic bridge deck constructed in accordance with the Texas Department of Transportation's (TxDOT) recommendations. A different family of curves results when either of these quantities is varied, and the curves shown in Figure 10.3 are not representative of the parameters used in either CIP or PCP test specimens. The value of α calculated for CIP test specimens is 1.33, based on the constants shown in Table 3.1, and the value of α for PCP test specimens was calculated to be 1.38, based on the constants shown in Table 3.2. The increase in punching shear capacity due to membrane compression was inherently included in the S-N data obtained from pulsating fatigue tests. It is not clear how the complicated failure modes observed in PCP test specimens affect the value for α calculated for these specimens. For this reason, and because of the small difference between the value of α calculated for CIP test specimens versus that calculated for PCP test specimens, S-N data were not adjusted to account for the different α values.

The increase in punching shear capacity that results from membrane compression is diminished whenever conditions do not allow arching action to develop. This can occur when multiple closely spaced axles load a bridge deck, or when an open joint through a deck does not allow the formation of a complete "dome." This phenomenon was not studied during the current research program, but is suggested by simple models such as the schematic illustration of arching action shown in Figure 2.1. Such conditions result in no increase in punching

shear capacity due to arching action and must be considered when evaluating bridge decks for adequacy in punching shear fatigue.

10.3 S-N Curves for Punching Shear Fatigue

A primary goal of this research program was to develop S-N curves for punching shear fatigue in bridge decks. The S-N curves established from static and pulsating fatigue tests were presented and discussed in detail in Chapter 9. The correlation between the deterioration determined from pulsating fatigue tests and that determined from rolling fatigue tests was established from research conducted by others and reported in (Matsui 1986), as discussed in Chapter 9.

The development of S-N curves suitable for design and assessment purposes began with the best-fit line through the combined data set presented in Figure 9.3. The standard deviation of regression was calculated for the combined data set. Another line, offset two standard deviations below the best-fit regression line, was established as a S-N curve suitable for pulsating fatigue design purposes. A S-N curve suitable for rolling fatigue design and assessment purposes was established using the correlation between rolling and pulsating fatigue discussed in Chapter 9. This relationship was applied to the design S-N curve that was offset two standard deviations below the best-fit regression line.

The endurance limit for punching shear fatigue was not established here, because of the limited number of pulsating fatigue tests performed. An endurance limit of 40% of the nominal static capacity was recommended by (Batchelor 1978) as being a safe endurance limit for bridge decks designed with 0.2% isotropic reinforcement and for unreinforced slabs. An endurance limit of 50% of the nominal static capacity was also recommended by (Batchelor 1978) as being a safe endurance limit for the design of conventionally reinforced bridge decks. Mallet (1991) states that plain concrete has “no fatigue limit since high-cycle,

low-stress loading can contribute to fatigue damage," and recommends that the fatigue strength at 10 million cycles be taken as approximately 55% of the static compressive strength.

A limit of 50% of the nominal static capacity was assumed as a safe endurance limit for punching shear fatigue design due to pulsating loads. S-N curves obtained from rolling fatigue tests conducted by (Matsui 1986) indicated failures at loads as low as 25% of the nominal static capacity. Based on those results, an endurance limit of 20% of the static capacity was established for punching shear fatigue design under rolling loads. The S-N curves developed for both rolling and pulsating fatigue design and assessment purposes are shown in Figure 10.4. The proposed endurance limits are included in the figure.

The S-N curves for design shown in Figure 10.4 were developed from test specimens, which as predicted by finite element modeling, had membrane compressive forces comparable to those observed by (Fang 1986) in tests on a full-scale bridge. As a result, the increase in punching shear capacity due to membrane compression is included in that figure. The increase is about 1.4 times the capacity predicted by the AASHTO and ACI punching shear capacity equation (Eq. 3.1). Examples that illustrate the calculations necessary to evaluate the adequacy of a bridge deck in punching shear fatigue using the S-N curves for design shown in Figure 10.4 are included in Appendix G and discussed in Section 10.6 of this thesis.

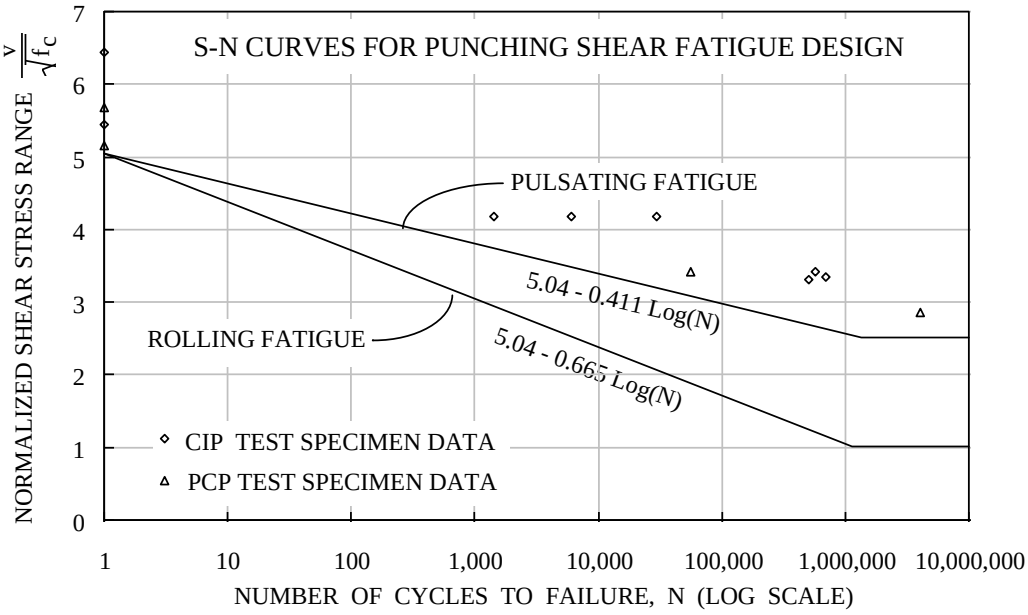

Figure 10.4: S-N curves for rolling and pulsating fatigue design and assessment purposes.

10.3.1 Combining Fatigue Cycles of Different Amplitudes

If a structure is subjected to constant-amplitude fatigue loading cycles, its service life can be estimated directly from S-N curves. This is not possible when loads of varying amplitude are applied. Numerous methods are available for assessing the cumulative effects of fatigue damage that result from variable-amplitude loading. The classical Palmgren/Miner approach is a popular method that has been adopted in various codes (Mallet 1991). A detailed discussion of the Palmgren/Miner method of evaluating the cumulative effects of fatigue damage is included in (Mallet 1991) and in most texts covering the subject of fatigue deterioration. This method can be used to assess whether or not a structure subjected to variable-amplitude fatigue loading can be expected to reach

its design service life. The design service life, expected loading history, and S-N data for the type of element under consideration are required to accomplish this. Loading histories are generally obtained through deterministic means, and obtaining S-N data for punching shear fatigue was a primary goal of this research effort.

Assessing the stress range and number of loading cycles from the passage of a standard AASHTO truck is a relatively simple task. The stress range is simply the wheel load divided by the area effective in resisting the punching shear stresses that result from that load, and the number of cycles is simply the number of axles. Calculating these quantities for a vehicle with multiple, closely spaced axles is more complicated. The reasons for this are illustrated in Figure 10.5. As illustrated in that figure, the fatigue damage associated with the passage of this type of vehicle must be evaluated using a method, such as the Palmgren/Miner approach mentioned above, that takes into account the effect of variable amplitude loading.

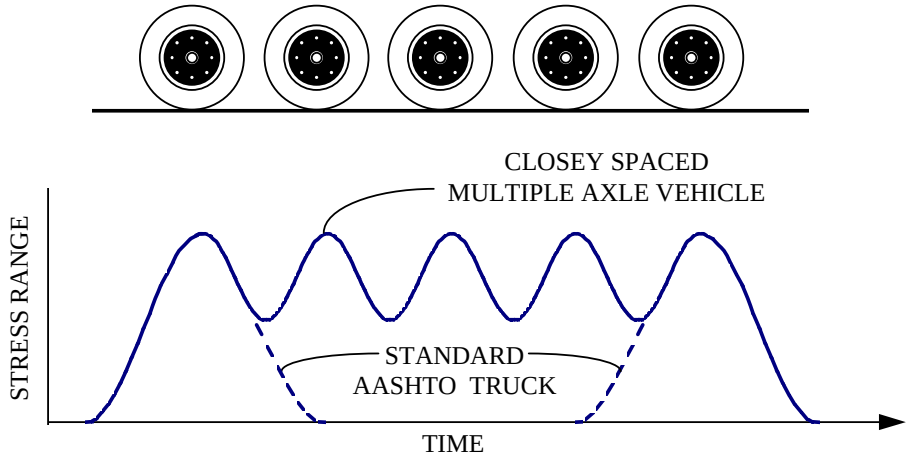

Figure 10.5: Schematic representation of the punching shear stress range in a bridge deck as a function of axle spacing.

The task of evaluating the fatigue damage caused by a vehicle with multiple, closely spaced axles is further complicated by the fact that the amplitude of the intermediate waves shown in Figure 10.5 is a function of axle spacing. As the axle spacing decreases, the amplitude of these waves also decreases, and the number of cycles associated with this vehicle approaches unity. The maximum stress associated with each wave shown in Figure 10.5 is a function of the load per wheel and the area over which this load is distributed. Smaller-diameter tires would allow closer axle spacing and decrease the number of effective cycles, but would increase the peak stress due to the decrease in loaded area. It would seem that an optimum configuration of axle spacing and tire diameter exists such that the punching shear fatigue damage associated with the passage of this type of vehicle would be minimized. Determining this optimum configuration was beyond the scope of this research effort.

It is clearly conservative to count each axle of a vehicle as producing one cycle of load. The cumulative damage associated with loads of varying magnitude can be assessed using methods such as the Palmgren/Miner approach. The methods available for combining variable amplitude loads are not exact, but do provide a method for assessing the expected fatigue life of a structure.

10.4 Beneficial Affects of Arching Action on Flexural Capacity

The flexural capacity of a bridge deck is increased due to the presence of membrane compression. This increase is quantifiable through the use of moment-axial force interaction diagrams. If both the magnitude and distribution of membrane force in a bridge deck are known (as a function of applied wheel load), a flexural failure load can be predicted using a yield-line analysis that includes the effects of membrane forces on flexural capacity.

Typical bridge decks carry flexural forces primarily through one-way (transverse) flexure. Significant increases in a bridge deck's flexural capacity are realized through the large transverse compressive membrane forces that develop near the girders. While compressive membrane forces are greatest near the point of load, it is near the girders where the negative moment yield lines will develop. Transverse compressive membrane forces in these regions are the primary reason for the significant increases in flexural capacity observed in tests on bridge decks.

A complete yield-line mechanism in a bridge deck requires the development of yield lines in the transverse direction. In the longitudinal direction, membrane compression resulting from arching action combines with longitudinal compression that results from composite flexural behavior between the deck and its supporting girders. However, near the ends of a bridge the compression resulting from composite behavior approaches zero in a simple span bridge, and tensile forces exist over the supports of a multiple span bridge with a continuous deck. As a result, the amount of longitudinal membrane compression that contributes to increases in flexural capacity can vary significantly.

Even though arching action was observed in the finite element model of the test specimens, it did not significantly increase the load calculated to cause flexural failure. This is due to the fact that membrane tensile forces were predicted in some regions of the test specimen model, which offset the affects of membrane compression in other regions. These membrane tensile forces surrounded the loaded area, as was illustrated schematically in Figure 2.1. Because the membrane tensile forces formed "hoops" around the loaded area, they resulted in tensile forces acting normal to the diagonal yield lines used in the yield line analyses of test specimens. The net result of arching action on the test specimens' flexural capacity was a virtually insignificant increase in flexural capacity. This was discussed in Chapter 3.

Evaluating the increase in flexural capacity due to arching action was not an objective of this research program. Because punching shear failure modes were required, test specimens were provided with sufficient reinforcement to prevent flexural failures. Furthermore, yield line analyses that included the affects of membrane compression on flexural capacity, indicated no significant increase in flexural capacity for the simply supported test specimens used in this testing program.

10.4.1 Standard AASHTO Trucks

A standard AASHTO truck has sufficient spacing between its axles for a zone of membrane tension to development that equilibrates the compressive membrane forces resulting from arching action. Numerous tests have confirmed the adequacy of the isotropically reinforced "Ontario-type" bridge decks under this type of load. These tests indicate that the increase in flexural capacity due to arching action results in a bridge deck design controlled by punching shear capacity and serviceability requirements.

10.4.2 Permit Loads (Multiple, Closely Spaced Axles)

As discussed in Chapter 2, it is not completely understood how arching action is affected when loads are applied simultaneously at multiple locations. This type of loading "spreads" the zone of tension and reduces the effectiveness of arching action. This was illustrated schematically in Figure 2.2. As illustrated in that figure, the presence of tension ties between supporting girders might compensate for the "spreading" of the tension zone. However, many questions regarding how arching action is affected by multiple, closely spaced loads, and how (and if) tension ties might compensate for this phenomenon, remain unanswered.

10.5 Summary of Applicability of Results to Design

Current design provisions used in the United States estimate punching shear capacities based on nominal stresses, and do not consider the beneficial affects of arching action. A method for estimating the punching shear capacity including the affects of arching action in a bridge deck was discussed above. An average value for membrane compression of about 2.0 kips/ft (29 kN/m) for each 20 kips (290 kN) of applied wheel load is recommended for use in that procedure. This value was determined from finite element models and from tests on a full-scale bridge conducted by (Fang 1986). Parametric curves can be developed using this method that cover a wide range of typical load and bridge deck configurations, and simplify the estimation of punching shear capacity including the affects of arching action. However, the range of parameters used in tests was very limited and the application of the method presented above should be limited accordingly.

S-N curves for punching shear fatigue design were presented in Figure 10.4 for both rolling and pulsating loads. The correlation between the damage that results from rolling loads and that resulting from pulsating loads was established from rolling fatigue tests conducted by (Matsui 1986). Endurance limits were not established from tests conducted in the current research effort, nor from those conducted by Matsui *et. al*. The endurance limit indicated in Figure 10.4 for pulsating fatigue was based on recommendations included in (Batchelor 1978). The endurance limit for rolling fatigue shown in Figure 10.4 was estimated from the S-N diagram included in (Matsui 1986). Several methods are available for assessing the fatigue damage that results from varying magnitude loads. Although none are exact, the classical Palmgren/Miner approach has been adopted in various codes (Mallet 1991).

Moment-axial force interaction diagrams can be used to estimate the flexural capacity of bridge decks including the affects of arching action. Yield line analyses can then be used to estimate the load that will cause flexural failure. The inclusion of membrane compression in the calculation of a bridge deck's flexural capacity is a cumbersome process that is dependent upon the magnitude and distribution of membrane forces throughout a bridge deck. For a standard AASHTO truck, or any vehicle with a relatively large axle spacing, arching action will significantly increase the load that will cause flexural failure. However, many questions remain as to how arching action is affected by multiple, closely spaced loads.

10.6 Sample Calculations for Adequacy of Bridge Decks in Punching Shear Fatigue

Four examples are included in Appendix G that illustrate the calculations necessary to evaluate the adequacy of a bridge deck in punching shear fatigue. Those calculations are for a typical $7^1/_2$-inch (191-mm) thick isotropically reinforced bridge deck and are summarized in Table 10.1. The examples indicate that punching shear fatigue would not be expected to control the design thickness of a bridge deck subjected to HS20-44 axle loads (Example G1). This is true even if closely spaced axles negate the increase in punching shear capacity that results from membrane compression (Example G2). Example G3 indicates that overloads of 4 times the HS20-44 axle load may result in punching shear fatigue failures, and Example G4 illustrates the dramatic way in which the absence of membrane compression reduces the punching shear fatigue life of a bridge deck. This situation could result from closely spaced axles, or from the presence of an open joint through a bridge deck, as discussed above.

The PCP specimens tested in this project showed failure loads well below those predicted by the analytical models used for design; the reasons for this are discussed in detail in Chapter 8. As discussed in that chapter, simple supports along all four edges of the test specimens were responsible for the complicated failure modes observed. If two-way action is forced into a bridge deck constructed with precast prestressed panels, a failure mode similar to that observed in PCP test specimens may occur, and designers should be aware of this possibility.

Table 10.1: Summary of the example punching shear fatigue calculations included in Appendix G for a typical TxDOT isotropic bridge deck.

Case	Minimum Number of Cycles to Causea Punching Shear Fatigue Failure	Comments
Standard HS20-44 Vehicle (Example G1)	-	Stress range is below endurance limit
HS20-44 Loads, Closely Spaced Axles (Example G2)	-	Stress range is below endurance limit
Overload Vehicle, Large Axle Spacing (Example G3)	900,000	Overload is 4 times the max. HS20-44 axle load
Overload Vehicle, Closely Spaced Axles (Example G4)	70,000	Overload is 4 times the max. HS20-44 axle load

CHAPTER ELEVEN
SUMMARY, CONCLUSIONS AND RECOMMENDATIONS

11.1 Introduction

The research program discussed in this thesis is summarized in this chapter. The experimental testing program and supporting analytical investigations are summarized. S-N data for rolling and pulsating fatigue are discussed. Conclusions drawn from the research, recommendations for flexural and punching shear capacity design, and recommendations for further research are also presented.

11.2 Summary of Experimental Tests

An experimental testing program that studied the punching shear fatigue behavior of bridge decks was completed. This testing program required the development of a test setup capable of loading full-scale test specimens to failure under both static, and pulsating loads. Both cast-in-place (CIP) and precast prestressed panel (PCP) specimens were tested, and S-N curves for punching shear fatigue were developed. Rolling fatigue tests were to be performed as part of this testing program, but were not completed, as was discussed previously in this thesis. The behaviors observed during the testing program are summarized in the following sections.

11.2.1 Summary of the Deterioration Observed During Pulsating Fatigue Tests

As load cycles accumulated during pulsating fatigue tests, the fatigue deterioration was clearly evidenced by loss of material from opposing faces of flexural cracks. Most cracks formed during the very early stages of fatigue cycling. These cracks generally propagated upward into the test specimens as load cycles accumulated. Dead-load deflections, or permanent set as a result of fatigue deterioration, increased with cycling for both CIP and PCP test specimens. This increase was greater for the CIP specimens than for the PCP specimens. Live load deflections remained relatively constant during fatigue cycling until late in the fatigue lives of both CIP and PCP specimens. These live load deflections increased dramatically as test specimens neared the end of their fatigue lives.

Fracture of welded wire reinforcement was observed in one of the two PCP pulsating fatigue test specimens. Partial separation of cast-in-place topping from the precast panel and degradation of the interface were observed during fatigue cycling of the other PCP specimen tested under pulsating fatigue loading.

11.2.2 Summary of Failure Modes and Loads

Failure modes and loads were discussed in detail in Chapter 8 for both CIP and PCP test specimens and are briefly summarized here. Static tests on CIP specimens resulted in punching shear failures at loads of about 1% and 20% greater than predicted by the general punching shear capacity equation discussed in Chapter 3. The observed average capacity was about 1.5 times greater than that predicted by the AASHTO and ACI equation, also discussed in Chapter 3.

Complicated combinations of punching shear failures, flexural hinging, and separation of the precast panels from the cast-in-place topping were observed during static tests on PCP specimens. This resulted in static punching shear

failures at loads much smaller than those predicted by the analytical models used for design. Two-way action in the PCP test specimens was responsible for the complicated failure modes, and for the resulting reduction in punching shear capacity for these test specimens. Adjustments were made to the analytical models to account for the observed failure modes. After these adjustments, the observed static punching shear failure loads were within 7% of those predicted by the general punching shear equation and the average observed failure load was only 2% less than that predicted by the general punching shear equation. The average observed static punching shear capacity was about 36% greater than that predicted by the AASHTO and ACI equation after adjustment for observed failure modes. Under pulsating fatigue loading, PCP specimens failed in modes similar to those observed in static tests on PCP test specimens.

CIP specimens appeared to have experienced punching shear fatigue failures, but a "post-mortem" inspection revealed that this was not the case. This inspection revealed that horizontal shear failures near the neutral axis apparently occurred in the CIP pulsating fatigue specimens. This gave the appearance of a punching shear failure as the loaded area punched through the delaminated top surface. This was discussed in detail in Chapter 8.

11.3 Summary of the Analytical Investigations

Analytical procedures were used to develop laboratory test specimens that would reflect the actual behavior of bridge decks, and used to extend the applicability of experimental test results. Both a complete bridge deck and test specimens were analyzed using the widely used structural analysis program SAP90™. The analysis considered non-linear elastic behavior due to cracking using the smeared cracking approach. A sequence of linear elastic analyses was

used to model a fully cracked state in both the full bridge and the test specimen finite element models.

Results from the finite element models agreed well with experimental test results. The extent and pattern of cracking predicted by the finite element models was very similar to that observed in experimental tests on CIP test specimens. Membrane forces predicted by the full-bridge model agreed reasonably well with those measured by (Fang 1986) in tests on a full-scale bridge. The membrane forces predicted by the finite element model for test specimens were not verified due to questionable strain gage readings. However, the good agreement between other experimental test results and the finite element analysis results suggests that the membrane forces predicted by the finite element analysis of test specimens are reasonable estimates of the actual membrane forces.

Arching action was clearly present in the fully cracked finite element models. The magnitude of membrane compressive forces predicted by the finite element test specimen model was very close to those in the full-bridge model and to those observed by (Fang 1986).

11.4 Summary of the Effects of Rolling Fatigue Versus Pulsating Fatigue

Rolling loads produce more fatigue deterioration than pulsating (fixed location) loads of the same magnitude. As discussed in (Matsui 1986), this is primarily the result of the alternating repetitions of movements across a crack that rolling loads produce, and was discussed in detail in Chapter 9. S-N curves obtained from pulsating fatigue tests must be correlated with those obtained from rolling fatigue tests in order to obtain results that can be used in design.

11.5 Summary of S-N Results

Results from pulsating fatigue tests on both CIP and PCP test specimens were normalized as discussed in Chapter 9 and plotted to create S-N diagrams. The data obtained from tests on PCP panel test specimens required adjustments to account for their complicated failure modes. Linear regression analyses were performed in order to calculate the best-fit line through that data. Good correlation was found between the applied load (or stress) range and the number of cycles required to cause punching shear failure in fatigue. S-N curves for pulsating and rolling fatigue design purposes were developed, as discussed in Chapter 10 and shown in Figure 10.4.

11.6 Conclusions

Based on the results of the research program discussed in this thesis, and on the results of research conducted by others, conclusions about arching action and general behavior were reached. These conclusions, as well as those regarding the applicability of the results to design, are summarized in the following sections.

11.6.1 General Conclusions about Arching Action

- Punching shear capacity is significantly increased by the presence of membrane compression that results from arching action (Section 10.2).
- Finite element models can be used to predict the distribution of membrane forces throughout a cracked bridge deck (Chapter 4).
- Arching action exists in simply supported slabs (Chapter 4), but results in an insignificant increase in flexural capacity (Section 3.3.4).
- In order to measure membrane forces in test specimens, redundant strain gages should be used to compensate for their unreliable nature (Section 8.5.5).

11.6.2 Conclusions on Observed Behaviors

- Rolling loads produce more fatigue damage than do fixed, pulsating loads of the same magnitude (Section 9.4.2).
- Good correlation exists between the applied stress range and the number of cycles required to cause a punching shear fatigue failure under fixed, pulsating loads (Section 9.2).
- Horizontal shear may be the failure mode associated with pulsating fatigue in slabs with unrestrained edges (Section 8.3).
- Two-way flexure in a bridge deck constructed with precast prestressed panels can result in capacities well below those predicted by current design models, and also in a loss of composite behavior between the panels and the cast-in-place concrete topping (Section 8.4).

11.6.3 Conclusions on the Applicability of Results to Design

- The thickness of a bridge deck should be based initially on the empirical provisions established for design of isotropically reinforced decks. The bridge deck design should then be checked against punching shear fatigue (Section 10.6).
- Standard AASHTO truck traffic on typical isotropically reinforced bridge decks would not be expected to result in punching shear fatigue failures (Section 10.6, Appendix G).
- Overload truck traffic may result in punching shear fatigue failures in typical TxDOT isotropic bridge decks (Section 10.6, Appendix G).
- The increase in punching shear capacity that results from membrane compression can be estimated using the procedure discussed in Chapter 10 and illustrated in Appendix F.

11.7 Recommendations

Recommendations for flexural and punching shear capacity design, as well as for further research are proposed in the following sections. The recommendations are based on results from the current research program along with results obtained from other researchers.

11.7.1 Recommendations for Punching Shear Design

Membrane compression should be included in the calculation of punching shear capacity. This can be accomplished using the procedure discussed in Chapter 10 and illustrated in Appendix F. A value of 2.0 kips/ft (29 kN/m) of membrane compression for each 20 kips (290 kN/m) of applied wheel load may be used to estimate the amount of membrane compression to be included in punching shear capacity calculations.

11.7.2 Recommendations for Flexural Design

The flexural design of restrained slabs and bridge decks should include the beneficial affects of arching action using the empirical design provisions established for isotropically reinforced bridge decks. Evaluating the increase in flexural capacity of a bridge deck due to arching action was not an objective of this research program. Very large reinforcement ratios and other precautions were taken to prevent flexural failures in test specimens. However, the analytical results obtained from finite element modeling of a complete bridge seem to corroborate the results obtained by (Fang 1986) from tests on a full-scale bridge.

Arching action, although present, will have little effect on the load calculated to cause flexural failure in a simply supported slab. Flexural capacities should be calculated for such slabs based on yield-line theory or other accepted methods, without including the affects of membrane forces.

11.7.3 Recommendations for Further Research

A parametric study should be undertaken in order to establish the limits for recommendations made in this thesis for including membrane compression in punching shear capacity calculations. A test setup capable of simulating the affects of rolling loads should be developed and used to confirm the rolling fatigue test results reported by (Matsui 1986). The endurance limit for rolling fatigue should be established using this test setup. The question of whether or not addition of "tension ties," as shown in Figure 2.2, can counter the reduction in effectiveness of arching action due to closely spaced, multiple axles should be investigated. The influence of stiff end diaframs on precast prestressed panel bridge decks should be investigated in order to verify that the complicated failure mode (at loads much lower than predicted by current design models) observed in PCP test specimens will not occur.

APPENDIX A

CALCULATION OF PRESTRESS LOSSES IN PRECAST PRESTRESSED CONCRETE PANELS

The following calculations estimate prestress losses following the procedure of Section 4.5.3 of the PCI Design Handbook.

T.L. = ES + CR + SH + RE = Total Loss

ES = elastic shortening
CR = creep of concrete
SH = shrinkage of concrete
RE = relaxation of tendons

$$ES = \frac{K_{es}\, E_s\, f_{cir}}{E_{ci}} = 4.20 \text{ ksi}$$

$K_{es} = 1.0$

$E_s = 28{,}000$ ksi

$$f_{cir} = K_{cir}\frac{P}{A} = 0.9\left(\frac{16.1}{6*4}\right) = 0.604 \text{ ksi}$$

$$E_{ci} = 57\sqrt{5{,}000} = 4{,}030 \text{ ksi}$$

$$CR = K_{cr}\frac{E_s}{E_c}\left(f_{cir} - f_{cds}\right) = 7.09 \text{ ksi}$$

$K_{cr} = 2.0$

$$E_c = 57\sqrt{7{,}000} = 4{,}770 \text{ ksi}$$

$f_{cds} = 0$

$$SH = \left(8.2 \times 10^{-6}\right) K_{sh} E_s \left(1 - 0.06\, V/S\right)\left(100 - RH\right) = 6.13 \text{ ksi}$$

$K_{sh} = 1.0$

$V = \left(96 \times 77 \times 4\right) = 29{,}568 \text{ in}^3$

$S = 2\left(96 \times 77\right) + 2\left[\left(96 \times 4\right) + \left(77 \times 4\right)\right] = 16{,}168 \text{ in}^2$

$RH = 70$

$$RE = \left[K_{re} - J\left(SH + CR + ES\right)\right] C = 4.30 \text{ ksi}$$

$K_{re} = 5.0$ ksi

$J = 0.040$

$C = 0.95$

T.L. = 4.20 + 7.09 + 6.13 + 4.30 = 21.7 ksi = Total Loss

$f_{se} = 189 - 21.7 = 168$ ksi

$$\text{Percent Loss} = 100\left(1 - \frac{168}{189}\right) = 11\%$$

APPENDIX B

CALCULATION OF MEMBRANE STRESSES IN THE FINITE ELEMENT MODEL

The following example is used to illustrate the calculation of membrane stresses in the finite element model for cast-in-place test specimens. Illustrated is the longitudinal membrane stress calculation for elements at the origin of coordinate axes. In the example, tension is positive.

$$\text{Membrane Stress} = \frac{\sum[(\text{Stress at Center of Element})(\text{Element Thickness})]}{\text{Total Model Thickness}}$$

LAYER	STRESS (ksi)	THICKNESS (in)	PRODUCT (kips/in)
7 (top)	-2.802	1.625	-4.553
6	0	0.625	0
5	0.602	0.50	0.301
4	0	0.75	0
3	4.379	0.75	3.284
2	0	0.75	0
1	0	2.50	0
	Σ =	7.50 in.	-0.968 kips/in

$$\text{Membrane Stress} = \frac{-0.968 \text{ kips/in}}{7.50 \text{ in}} = -0.129 \text{ ksi (compression)}$$

$$\text{Membrane Force} = (-0.968 \text{ kips/in}) \times (12 \text{ in/ft}) = -11.6 \text{ kips/ft (compression)}$$

APPENDIX C

CALCULATION OF MEMBRANE STRESSES FROM STRAIN GAGE READINGS

The following example is used to illustrate the calculation of membrane stresses in cast-in-place test specimens using strain gage readings. Illustrated is the longitudinal membrane force calculation for Test Specimen S3P110. Tension is positive. Measured strains are shown in Figure C.1

Material Properties:

E_S = 29,000 ksi

f'_c = 5,870 psi

$E_C = 57\sqrt{f'_c}$ = 4,367 ksi

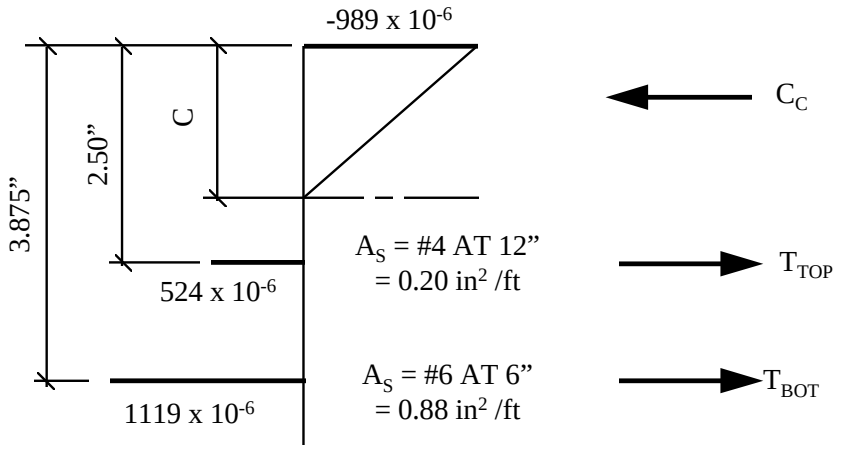

Figure C.1: Measured strains and nomenclature used in calculations.

From similar triangles (refer to Figure C.1):

$$C = 989\left(\frac{2.5}{989+524}\right) = 1.63 \text{ in} \qquad \text{or} \qquad C = 989\left(\frac{3.875}{989+1119}\right) = 1.82 \text{ in}$$

$$\text{Assume:} \quad C = \frac{1.63+1.82}{2} = 1.73 \text{ in}$$

$$T_{TOP} = \left(524\times10^{-6}\right)\left(29{,}000 \text{ ksi}\right)\left(0.20 \text{ in}^2 / \text{ft}\right) = 3.04 \text{ kips/ft (tension)}$$

$$T_{BOT} = \left(1119\times10^{-6}\right)\left(29{,}000 \text{ ksi}\right)\left(0.88 \text{ in}^2 / \text{ft}\right) = 28.56 \text{ kips/ft (tension)}$$

CASE 1: Linear Stress-Strain Relation for Concrete

$$C_C = \frac{\left(-989\times10^{-6}\right)\left(4{,}367 \text{ ksi}\right)\left(1.73 \text{ in}\right)\left(12 \text{ in} / \text{ft}\right)}{2} = -44.83 \text{ kips/ft}$$

(compression)

Membrane Force = $C_C + T_{TOP} + T_{BOT}$ = -13.2 kips/ft (compression)

CASE 2: Non-Linear Stress-Strain Relation for Concrete

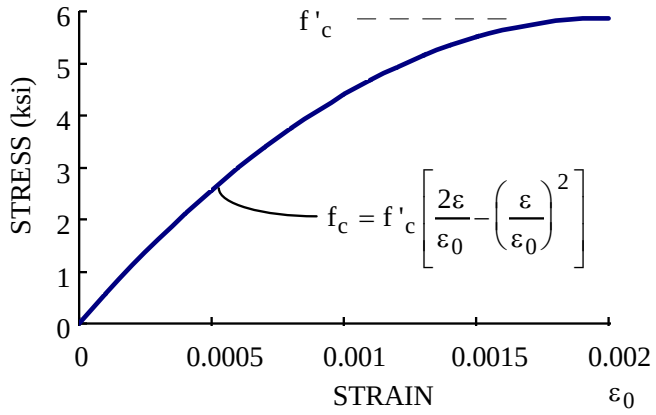

Figure C.2: Hognestad's non-linear stress-strain curve for concrete.

The total compression force is obtained by integrating the stress over the compression zone's area. Integrating the stress-strain relation shown in Figure C.2 results in the equation:

$$C_C = bf'_c\frac{\varepsilon_{max}C}{\varepsilon_0}\left[1-\frac{\varepsilon_{max}}{3\varepsilon_0}\right]$$

$$= (12\text{ in / ft})(5.87\text{ ksi})\frac{\left(-989\times10^{-6}\right)(1.73\text{ in})}{(0.002)}\left[1-\frac{989\times10^{-6}}{3(0.002)}\right]$$

$$= -50.3\text{ kips/ft (compression)}$$

which is greater than the compression force calculated for the linear elastic case due to the value of ε_0 (0.002) used in the equation.

Membrane Force = $C_C + T_{TOP} + T_{BOT}$ = -18.7 kips/ft (compression)

CASE 3: Inclusion of Poisson Effects

The actual stress in the concrete increases when the 2-dimensional state of stress is considered in the above calculations. Assuming an equal concrete strain in the direction perpendicular to the measured concrete strain shown in Figure C.1, the actual stress can be calculated using the relation:

$$\left(f_c\right)_{ACTUAL} = \frac{\left(f_c\right)_{APPARENT}}{\left(1-\nu\right)}$$

Where ν is Poisson's ratio for concrete. The membrane force calculated for the non-linear case was modified using a value of 0.15 for Poisson's ratio in the above expression. This increased the calculated compression force in the concrete to approximately 59.2 kips/ft.

Membrane Force = $C_C + T_{TOP} + T_{BOT}$ = -27.6 kips/ft (compression)

APPENDIX D

MATERIAL CHARACTERISTICS

Table D.1: Concrete properties for CIP Test Specimens

Specimen	Casting Date	Slump (in)	Test Date	f'_c (psi)		
				14 Day	28 Day	Test Date
Static #1	12/23/92	5.0	4/23/93	5,360	5,520	5,950
Static #2	12/23/92	5.0	5/17/93	5,360	5,520	5,950
S1P145	7/19/93	5.5	3/22/94	3,990	5,150	6,200
S2P145	7/19/93	5.5	3/30/94	3,990	5,150	6,200
S3P145	7/19/93	5.5	4/6/94	3,990	5,150	6,200
S1P110	5/11/94	5.5	7/18/94	4,580	4,990	5,490
S2P110	5/11/94	5.5	8/2/94	4,580	4,990	5,710
S3P110	5/11/94	5.5	9/15/94	4,580	4,990	5,870

Note: 1 in = 25.4 mm, 1 psi = 6.89 kPa

Table D.2: Concrete properties for PCP Test Specimens

Specimen	Casting Date	Slump (in)	Test Date	f'_c (psi)		
				14 Day	28 Day	Test Date
Static #1	8/26/94	6.0	9/27/94	4,220	4,590	4,770
Static #2	8/26/94	6.0	10/10/94	4,220	4,590	4,720
PS1P55	8/26/94	6.0	10/28/94	4,220	4,590	4,840
PS1P77	8/26/94	6.0	11/15/94	4,220	4,590	4,830

Note: 1 in = 25.4 mm, 1 psi = 6.89 kPa

APPENDIX E

MODIFICATION OF PREDICTED PUNCHING SHEAR CAPACITIES TO ACCOUNT FOR OBSERVED FAILURE MODES IN PRECAST PRESTRESSED PANEL TEST SPECIMENS

As discussed throughout this thesis, calculated punching shear capacities were adjusted to account for the observed failure modes in PCP test specimens. The adjusted values were summarized in Table 9.2 and used in the calculation of S-N data. The adjustment calculations for effective areas, $(b_0d)_{eff}$, were discussed in detail in Section 8.4 of this thesis and are illustrated here.

Topping thickness = 3.25 in.
Panel thickness = 4.00 in.
Total effective depth for punching shear calculations = 5.25 in.
b_1 = 10.0 in.
b_2 = 17.5 in.

Static Test Specimens and Specimen PS1P77 (Refer to Figure 8.6)

Failure planes through cast-in-place topping on all sides of loaded area, and through panel only on east and west edges of load.

Topping:

$$A_{eff} = 2\left[17.5\text{ in} + 10\text{ in} + (2)3.25\text{ in}\right](3.25\text{ in}) \quad = 221\text{ in}^2$$

Precast Panels:

$$A_{eff} = 2\left[16.5\text{ in} + 2\text{ in}\right](2.00\text{ in}) \quad = 74\text{ in}^2$$

Total Effective Area:

$$(b_0d)_{eff} = (221\text{ in}^2 + 74\text{ in}^2) = 295\text{ in}^2$$

Test Specimen PS1P55

Punching shear failure planes through topping and precast panel, but only on three sides north of the loaded area's south edge.

Total Effective Area:

$$(b_0 d)_{eff} = (17.5\text{ in} + 5.25\text{ in})(5.25\text{ in}) + (2)\left(10\text{ in} + \frac{5.25\text{ in}}{2}\right)(5.25\text{ in}) = 252\text{ in}^2$$

APPENDIX F

CALCULATION OF PUNCHING SHEAR CAPACITY INCLUDING THE AFFECTS OF MEMBRANE COMPRESSION

The following example illustrates the calculation of punching shear capacity including the affects of membrane compression.

For CIP Static Test Specimens:

f'_c = 5,950 psi

$\bar{d}$ = 4.25 in.

b_1 = 16 in.

b_2 = 24 in.

$$\beta_c = \frac{b_2}{b_1} = 1.5$$

$$f_t = \left(2 + \frac{4}{\beta_c}\right)\sqrt{f'_c} \le 4\sqrt{f'_c} = 309 \text{ psi}$$

Estimate maximum wheel load using the AASHTO and ACI punching shear capacity equation (Eq. 3.1):

$$V_C = 2\left(b_1 + b_2 + 2\bar{d}\right)\bar{d}\, f_t = 127 \text{ kips}$$

Estimate membrane compressive stress in the $7^1/_2$ inch thick slab resulting from this load, assume 2.0 kips/ft of membrane compression for each 20 kips of applied wheel load:

$$P_{memb} = \left(\frac{2.0 \text{ kips / ft}}{20 \text{ kips}}\right)\left(\frac{127 \text{ kips}}{\left(12\frac{\text{in}}{\text{ft}}\right)\left(7\frac{1}{2} \text{ in}\right)}\right) = 0.141 \text{ ksi}$$

Use (Eq. 10.1) to calculate θ based on this value of P_{memb}, and the value of f_t calculated above (f_t = 309 psi = 0.309 ksi):

$$\theta = \frac{1}{2}\text{Cos}^{-1}\left(\frac{P_{memb}}{2\,f_t + P_{memb}}\right) = 39.6^o$$

Use the general punching shear capacity equation (Eq. 3.3) to estimate V_C using the parameters above and θ = 39.6º:

$$V_C = 2\left(b_1 + b_2 + \frac{2\bar{d}}{\tan\theta}\right)\frac{\bar{d}}{\tan\theta}\,f_t = 159 \text{ kips}$$

Now repeat, using this value to estimate P_{memb} in lieu of the initial 127 kip estimate:

P_{memb} = 0.177 ksi

θ = 38.5º

V_C = 167 kips

Repeat again:

P_{memb} = 0.186 ksi

θ = 38.3º

V_C = 169 kips SAY 170 kips

Note: Observed punching shear failure loads for CIP static test specimens were 171 kips and 205 kips.

APPENDIX G

EXAMPLE CALCULATIONS FOR EVALUATION OF ADEQUACY IN PUNCHING SHEAR FATIGUE, INCLUDING THE AFFECTS OF ARCHING ACTION

The following examples illustrate how the S-N curves for design, shown in Figure 10.4, are used to evaluate the minimum number of load cycles required to cause a punching shear fatigue failure in a typical isotropically reinforced bridge deck.

For a typical $7^1/_2$ inch thick TxDOT isotropically reinforced bridge deck:

$f'_c = 4{,}000$ psi

$\bar{d} = 5.75$ in.

G1: Typical TxDOT Isotropic Bridge Deck, Standard HS20-44 Vehicle

Assume a standard HS20-44 vehicle. Axle loads for this vehicle are shown in Figure 4.3. The maximum wheel load, P, for this vehicle is 16 kips.

Estimate the tire contact area using the provisions of Section 3.30 of the AASHTO Code:

$$A = 0.01P = 0.01\,(16{,}000\text{ lb}) = 160\text{ in.}^2$$

$$\frac{\ell}{w} = \frac{1}{2.5} = \frac{b_1}{b_2} \quad \Rightarrow \quad b_1 = \sqrt{\frac{A}{2.5}} = 8\text{ in.}$$

$$b_2 = 20\text{ in.}$$

Calculate the nominal punching shear stress, v, and normalize this stress for use with the S-N curves for design shown in Figure 10.4:

$$v = \frac{P}{b_0 d} = \frac{16{,}000\text{ lb.}}{(2)\left[(8\text{ in.}) + (20\text{ in.}) + (2)(5.75\text{ in.})\right](5.75\text{ in.})} = 35.2\text{ psi}$$

$$\text{Normalized Stress} = \frac{v}{\sqrt{f'_c}} = \frac{35.2}{\sqrt{4{,}000}} = 0.557$$

The S-N curves for design shown in Figure 10.4 include a factor of about 1.4, that increases the punching shear capacity of a bridge deck due to arching action. This is about the increase in punching shear capacity that can be expected, associated with a standard AASHTO truck on the $7^1/_2$-inch thick isotropically reinforced bridge deck used for this example. Therefore, the normalized stress calculated above can be used directly (without further adjustment) with the S-N curves for design shown in Figure 10.4. Referring to that figure, this value of normalized stress (0.557) falls below the fatigue, or endurance limit, for rolling fatigue. Therefore, a punching shear fatigue failure would not be expected, and the slab is adequate with respect to punching shear fatigue.

G2: Typical TxDOT Isotropic Bridge Deck, Permit Vehicle With Closely Spaced HS20-44 Axle Loads

Assume a vehicle with many, closely spaced axles. For this vehicle, the beneficial affects of arching action on punching shear capacity are diminished. Note that, as discussed in Section 10.6, the affects of arching action are also diminished under a standard HS20-44 vehicle near open joints in a bridge deck. Conservatively assume no increase in punching shear capacity, and also assume that each wheel has a load and a tire contact area equivalent to that of a standard HS20-44 truck.

From Section G1 above:

$$P = 16{,}000 \text{ lbs.}, \quad b_1 = 8 \text{ in.}, \quad b_2 = 20 \text{ in.}, \quad \beta_c = \frac{b_2}{b_1} = \frac{20}{8} = 2.5$$

Normalized Stress = 0.557

Since the S-N curves shown in Figure 10.4 include the beneficial affects of arching action, the normalized stress that results from this vehicle must be increased to account for the lack of arching action due to the multiple, closely spaced axles assumed in this example. Since the S-N curves for design include a factor of about 1.4 accounting for the presence of arching action, multiply the normalized stress calculated above by this factor:

Adjusted Normalized Stress = 1.4 (0.557) = 0.780

Referring to the S-N curve for design shown in Figure 10.4, this value of adjusted normalized stress (0.780) falls below the fatigue, or endurance limit, for rolling fatigue. Again, a punching shear fatigue failure would not be expected.

G3: Typical TxDOT Isotropic Bridge Deck, Overload Vehicle With HS20-44 Axle Spacing

Assume a vehicle with a wheel load of 64 kips (4 times that of an HS20-44 truck). Estimate the tire contact area using the provisions of Section 3.30 of the AASHTO Code:

$$A = 0.01P = 0.01\left(64{,}000 \text{ lb}\right) = 640 \text{ in}^2$$

$$\frac{\ell}{w} = \frac{1}{2.5} = \frac{b_1}{b_2} \quad \Rightarrow \quad b_1 = \sqrt{\frac{A}{2.5}} = 16 \text{ in.}$$

$$b_2 = 40 \text{ in.}$$

Calculate the nominal punching shear stress, v, and normalize this stress for use with the S-N curves for design shown in Figure 10.4:

$$v = \frac{P}{b_0 d} = \frac{64{,}000 \text{ lb.}}{(2)\left[(16 \text{ in.}) + (40 \text{ in.}) + (2)(5.75 \text{ in.})\right](5.75 \text{ in.})} = 82.4 \text{ psi}$$

$$\text{Normalized Stress} = \frac{v}{\sqrt{f'_c}} = \frac{82.4}{\sqrt{4{,}000}} = 1.30$$

The parametric curves shown in Figure 10.3 indicate that the increase in punching shear capacity due to arching action is greater for this vehicle (due to the large tire contact area) than for an HS20-44 truck. However the curves shown in that figure do not include a value for b_2 of 40 inches. Use the procedure outlined in Appendix F to calculate the punching shear capacity of this slab under this load. After a few iterations, the punching shear capacity including the affects of arching action is calculated to be 306 kips. The punching shear capacity calculated using the AASHTO and ACI equation is 177 kips. Therefore, the increase in punching shear capacity due to arching action is: $\frac{306}{177} = 1.7$.

If arching action will be present under this vehicle (large axle spacing), then it would be conservative to use the value of normalized stress calculated above (1.30) with the S-N curves for design to estimate the minimum number of cycles that would cause a punching shear fatigue failure. This conservatively predicted N-value would be about 420,000 cycles for rolling fatigue. However, the S-N curves for design include a factor that increases the punching shear capacity by about 1.4 times that given by the AASHTO and ACI equation to include the affects of arching action. Since the punching shear capacity under this vehicle is estimated to be 1.7 times that predicted by the AASHTO and ACI equation, the

normalized punching shear stress calculated above (1.30) can be reduced by the ratio of $\frac{1.7}{1.4}$ = 1.2. This results in an adjusted normalized stress range of about 1.08; the predicted minimum number of load cycles to cause a punching shear fatigue failure would be about 900,000 cycles.

G4: Typical TxDOT Isotropic Bridge Deck, Overload Vehicle With Closely Spaced Axles

If the vehicle of Section G3 above has closely spaced axles, the benefits of arching action will be reduced. In this case, the normalized stress calculated above (1.30) must be increased to account for the lack of arching action. Since the S-N curves for design include a factor of about 1.4 accounting for the presence of arching action, multiply the normalized stress calculated above by this factor:

Adjusted Normalized Stress = 1.4 (1.30) = 1.82

Referring to the S-N curve for design shown in Figure 10.4, a punching shear fatigue failure would not be expected until after about 70,000 cycles of load from this vehicle.

G5: Summary of Results for a Typical TxDOT Isotropic Bridge Deck

The example calculations above (for a typical TxDOT isotropic bridge deck) are summarized in Table G.1. The calculations indicate that for HS20-44 loads, punching shear failures would not be expected to occur. For overload

conditions, punching shear fatigue failures may occur. The reduced effectiveness of arching action that results from closely spaced axles or open joints through bridge decks, may result in dramatic reductions in the number of load cycles required to cause a punching shear fatigue failure.

Table G.1: Summary of punching shear fatigue calculations for a typical TxDOT isotropic bridge deck.

Case	Minimum Number of Cycles to Cause a Punching Shear Fatigue Failure	Comments
Standard HS20-44 Vehicle (Example G1)	-	Stress range is below endurance limit
HS20-44 Loads, Closely Spaced Axles (Example G2)	-	Stress range is below endurance limit
Overload Vehicle, Large Axle Spacing (Example G3)	900,000	Overload is 4 times the max. HS20-44 axle load
Overload Vehicle, Closely Spaced Axles (Example G4)	70,000	Overload is 4 times the max. HS20-44 axle load

APPENDIX H

SUMMARY OF TEST DATA

The following pages are test data. The data has been converted to engineering units. Loads are in kips, deflections are inches, and strains are microstrains. The location of strain gages and linear potentiometers used to record the data is discussed in Chapter 5. The symbol "#####" indicates a strain gage that has failed.

REFERENCES

Abendroth, R. E., Pratanata, H. and Singh, B. (1991). "Composite Precast Prestressed Concrete Bridge Slabs," *Final Report, Iowa DOT Project HR-319, ISU-ERI-Ames-92076,* Engineering Research Institute, Iowa State University, Ames, Iowa.

Alexander, S. D. B. and Simmonds, S. H. (1987). "Ultimate Strength of Slab-Column Connections," *ACI Structural Journal*, V. 84, No. 3, May-June 1987, pp. 255-261.

Batchelor, B. deV., Hewitt, B. E. and Csagoly P. (1978). "An Investigation of the Fatigue Strength of Deck Slabs of Composite Steel/Concrete Bridges," *Transportation Research Record,* No. 664, pp. 153-161.

Bridge Design Guide (1990). 1st Ed., The State of Texas, State Department of Highways and Public Transportation, pp. 4-02, 5-01, 5-05, 5-08 to 5-12.

Building Code Requirements for Reinforced Concrete and Commentary (1989). American Concrete Institute, Detroit, Michigan, 1989. ACI 318-89 and ACI 318R-89.

Dragosavic, M. and Beukel, A. van den (1974). "Punching Shear," *Heron*, V. 20, No. 2, 1974.

Elling, C. W., Klingner, R. E. and Burns, N. H. (1986). "Distribution of Girder Loads in a Composite Highway Bridge," *Research Report 350-2*, Center for Transportation Research, The University of Texas at Austin, Austin, Texas.

Fang, I.-K., Worley, J., Klingner, R. E. and Burns, N. H. (1986). "Behavior of Ontario-Type Bridge Decks on Steel Girders," *Research Report 350-1,* Center for Transportation Research, The University of Texas at Austin, Austin, Texas.

Fang, I.-K., Worley, J., Klingner, R. E. and Burns, N. H. (1990a). "Behavior of Isotropic Concrete Bridge Decks on Steel Girders," *Structures Journal*, ASCE, V. 116, No. 3, March 1990, pp. 659-679.

Fang, I.-K., Tsui, C. K.-T., Burns, N. H. and Klingner, R. E. (1990b). "Fatigue Behavior of Cast-in-Place and Precast Panel Bridge Decks with Isotropic Reinforcement," *PCI Journal*, V. 35, No. 3, May-June 1990, pp. 28-39.

Kim, J., Burns, N. H. and Klingner, R. E. (1994). "Factors affecting the Design Thickness of Bridge Slabs: Results of Static and Fatigue Test," *Research Report 1305-2*, Center for Transportation Research, The University of Texas at Austin, Austin, Texas.

Kim, K. H., Klingner, R. E., Burns, N. H. and Dominguez, J. (1988). "Behavior of Skew Bridges with Ontario-Type Decks," *Research Report 350-4F*, Center for Transportation Research, The University of Texas at Austin, Austin, Texas.

Klingner, R. E., Fang, I.-K., Tsui, C. K.-T. and Burns, N. H. (1990). "Load Capacity of Isotropically Reinforced, Cast-in-Place and Precast Panel Bridge Decks," *PCI Journal*, V. 35, No. 4, July-August 1990, pp. 104-114.

Kuang, J. S. and Morley, C. T. (1992). "Punching Shear Behavior of Restrained Reinforced Concrete Slabs," *ACI Structural Journal*, V. 89, No. 1, January-February 1992, pp. 13-19.

Kupfer, H., Hilsdorf, H. K. and Rusch, H. (1969). "Behavior of Concrete under Biaxial Stresses," *ACI Journal*, V. 66, August 1969, pp. 656-666.

MacGregor, J. G. (1992). *Reinforced Concrete: Mechanics & Design*, 2nd ed., Prentice-Hall, Inc., Englewood Cliffs, New Jersey, pp. 659-673.

Mallet, G. P. (1991). *Fatigue of Reinforced Concrete*, Transport and Road Research Laboratory, Department of Transport, HMSO Publications, London, England, pp. 3-4, 153-160.

Matsui, S., Sonoda, K., Okamura, H. and Okada, K. (1986). "Concepts for Deterioration of Highway Bridge Decks and Fatigue Studies," *International Symposium on Fundamental Theory of Reinforced and Prestressed Concrete*, Nanjing, China, September 1986, pp. 831-838.

Ontario Highway Bridge Design Code and Commentary (1983). 2nd ed., Ontario Ministry of Transportation and Communication, Highway Engineering Division, Ontario, Canada.

PCI Design Handbook (1985). 3rd ed., Precast Concrete Institute, Chicago, Illinois, pp. 4-39, to 4-41, 11-18.

Perdikaris, P. C. and Beim, S. (1988). "RC Bridge Decks under Pulsating and Moving Load," *ASCE Journal of Structural Engineering*, V. 114, No. 3, March 1988, pp. 591-607.

Perdikaris, P. C., Beim, S. and Bousias, S. N. (1989). "Slab Continuity Effect on Ultimate and Fatigue Strength of Reinforced Concrete Bridge Deck Models," *ACI Structural Journal*, V. 86, No. 4, July-August 1989, pp. 483-491.

Standard Specifications for Construction of Highways, Streets, and Bridges (1993). Texas Department of Transportation, pp. 620-621.

Standard Specifications for Highway Bridges (1992). 15th ed., American Association of State Highway and Transportation Officials, Washington, D.C.

Tsui, C. K.-T., Burns, N. H. and Klingner, R. E. (1986). "Behavior of Ontario-Type Bridge Decks on Steel Girders: Negative Moment Region and Load Capacity," *Research Report 350-3,* Center for Transportation Research, The University of Texas at Austin, Austin, Texas.

Whitt, J., Kim, J., Burns, N. H. and Klingner, R. E. (1993). "Factors Affecting the Design Thickness of Bridge Slabs: Test Setup," *Research Report 1305-1*, Center for Transportation Research, The University of Texas at Austin, Austin, Texas.

Wilson, E., and Habibullah, A. (1988). *SAP90*^{TM} *-- A Series of Computer Programs for the Static and Dynamic Finite Element Analysis of Structures*, Computers and Structures, Inc., Berkeley, California, 1988.